



HAL
open science

Atomization and dispersion of a liquid jet : numerical and experimental approaches

Francisco Felis-Carrasco

► **To cite this version:**

Francisco Felis-Carrasco. Atomization and dispersion of a liquid jet : numerical and experimental approaches. Fluids mechanics [physics.class-ph]. Ecole Centrale Marseille, 2017. English. NNT : 2017ECDM0001 . tel-01558141

HAL Id: tel-01558141

<https://theses.hal.science/tel-01558141>

Submitted on 7 Jul 2017

HAL is a multi-disciplinary open access archive for the deposit and dissemination of scientific research documents, whether they are published or not. The documents may come from teaching and research institutions in France or abroad, or from public or private research centers.

L'archive ouverte pluridisciplinaire **HAL**, est destinée au dépôt et à la diffusion de documents scientifiques de niveau recherche, publiés ou non, émanant des établissements d'enseignement et de recherche français ou étrangers, des laboratoires publics ou privés.

École Doctorale : Sciences pour l'ingénieur: Mécanique, Physique, Micro et Nanoélectronique (ED353)

THÈSE DE DOCTORAT

pour obtenir le grade de

DOCTEUR de l'ÉCOLE CENTRALE de MARSEILLE

Discipline : Mécanique et Physique des Fluides

ATOMISATION ET DISPERSION D'UN JET LIQUIDE : Approches Numérique et Expérimentale

par

FELIS CARRASCO Francisco

Directeur de thèse : ANSELMET Fabien

Soutenue le 24 Mars 2017

devant le jury composé de :

AMIELH Muriel	CR IRPHE/CNRS Marseille	Invitée
ANSELMET Fabien	PR IRPHE/ECM Marseille	Directeur
DEMOULIN François-Xavier	PR CORIA/Univ. de Rouen	Rapporteur
ELICER-CORTÉS Juan-Carlos	PR DIMEC/Univ. de Chile	Invité
GJELSTRUP Palle	Dr.-Ir. Dantec-Dynamics Denmark	Invité
MATAS Jean-Philippe	PR LMFA/Univ. Lyon I	Rapporteur
SIMONIN Olivier	PR IMFT/INP Toulouse	Président
TOMAS Séverine	IR G-EAU/IRSTEA Montpellier	Examinatrice
VALLET Ariane	CR ITAP/IRSTEA Montpellier	Examinatrice

Hey Hey,
My My
— *Neil Young*

(Into the Black)

Acknowledgements

I would like to thank everyone involved directly or indirectly in the achievement of this doctoral thesis.

From before my arrival in France, to the people at Universidad de Chile, who pushed me into this adventure. Specially to Pr. Juan Carlos ELICER, who carefully introduced me to the unknowns of the turbulence world. Also, to the CONICYT Becas-Chile fellowship from the Chilean government, that made possible the accomplishment of this work.

Later, in France, to the Turbulence team at IRPHE Marseille for their welcoming and guidance: Pr. Fabien ANSELMET, Dr. Muriel AMIELH, Dr. Laurence PIETRI, Dr. Malek ABID and all Professors at Centrale-Marseille. Special thanks to the International Relations team who support us all foreign students with all the guidance upon our arrival.

Moving to Montpellier and the actual beginning of the thesis. Many thanks to both PEPS and PRESTI teams at IRSTEA Montpellier. Specially to Dr. Séverine TOMAS and Dr. Ariane VALLET, for their continuing guidance and support during the development of this thesis. To Bernadette RUELLE, Michèle EGEE, Pr. Tewfik SARI, Dr. Olivier BARRETEAU, Dr. Dominique ROLLIN and Dr. Bruno MOLLE for their continuous administrative support. And on the fine details of the experimental set-up, to Cyril TINET, David BASTIDON and Jean-Philippe TRANI from the PEPS team.

And in the end, to the whole thesis jury, actively present even in the early steps of this work. To Pr. Olivier SIMONIN for the on-time discussions about multi-phase flow models, Pr. François-Xavier DEMOULIN for the initial OpenFOAM support at CORIA, Pr. Jean-Philippe MATAS for the experimental post-treatment guidance, Dr. Jean-Bernard BLAISOT for the detailed explanations and guidance of the experimental set-up and Dr. Jean-Jacques LASSERRE and Dr. Palle GJELSTRUP for the scientific and technical support at Dantec-Dynamics.

Finally, to my friends, my parents and family who are always there on any adventure that I decide to pursue (video-calls are easy these days...). I am sure that there will be many more, so hang-in-there!

A todos, gracias... ¡Totales!

Montpellier, March 24, 2017

F. F.

Abstract

A typical water round-nozzle jet for agricultural applications is presented in this study. The dispersion of a liquid for irrigation or pesticides spraying is a key subject to both reduce water consumption and air pollution. A simplified study case is constructed to tackle both scenarios, where a round $d_n = 1.2 \text{ mm}$ nozzle of a length $L_n = 50d_n$ is considered. The injection velocity is chosen to be $\bar{u}_j = 35 \text{ m/s}$, aligned with gravity, placing the liquid jet in a turbulent atomization regime. The flow is considered statistically axisymmetric. Experimental and numerical approaches are considered.

An Eulerian mixture multiphase model describes the original two-phase flow. Several U-RANS turbulence models are used: $k - \epsilon$ and RSM; where special attention is taken to the modelling of variable density effects from the mixture formulation. A custom numerical solver is implemented using the OpenFOAM CFD code. A series of study cases are constructed to test the influence of the turbulence modeling and first/second-order closures of the turbulent mass fluxes.

LDV and DTV optical techniques are used to gather statistical information from both the liquid and the gas phases of the spray. The experimental campaign is carried out from $x/d_n = 0$ to 800. Concerning the LDV, small ($\sim 1 \mu\text{m}$) olive-oil tracers are used to capture the gas phase, where a distinction between the liquid droplets and tracers is achieved by a specific set-up of the laser power source and the burst Doppler setting (BP-Filter and SNR). On the dispersed zone, DTV measurements are carried out to measure velocities and sizes of droplets. Special attention to the depth-of-field (DOF) estimation is taken in order to obtain a less biased droplet's size-velocity correlation.

Numerical and experimental results show good agreement on the mean velocity field. A strong dependence on the turbulence model is found. However, the RSM does not capture the same behaviour on the calculated Reynolds stresses. Indeed, neither the experimental anisotropy ($\overline{u_y'^2}/\overline{u_x'^2} \approx 0.05$), nor the liquid-gas slip-velocity can be reproduced, even with a second-order closure for the turbulent mass fluxes. The strong density ratio (water/air), flow's directionality and production of turbulent kinetic energy may be the cause of a weak dispersion and mixing between the two fluids. This mechanism is not yet clarified from a RSM modeling point-of-view.

Key words: Liquid Jet, Atomization, Mixture, RANS, Turbulence, LDV/DTV

Résumé

L'atomisation d'un jet circulaire d'eau typique des applications agricoles est présentée dans cette étude. Maîtriser la dispersion de l'eau à des fins d'irrigation ou de traitements phytosanitaires implique de réduire la consommation d'eau et la pollution de l'environnement. Un cas d'étude simplifié est construit : une buse ronde $d_n = 1.2 \text{ mm}$ et d'une longueur $L_n = 50d_n$ est considérée. La vitesse d'injection est fixée à $\bar{u}_j = 35 \text{ m/s}$ et alignée avec la gravité, plaçant le jet liquide dans un régime d'atomisation turbulent. L'écoulement est statistiquement axisymétrique. L'approche est à la fois expérimentale et numérique.

Un modèle multiphasique Eulérien de mélange décrit l'écoulement constitué de deux phases. Plusieurs modèles de turbulence U-RANS sont utilisés : $k - \epsilon$ et RSM. Une attention particulière est alors portée à la modélisation des effets de masse volumique variable issus de la formulation du fluide de mélange. Un solveur numérique spécifique est développé à l'aide du code CFD OpenFOAM. Une série de cas d'étude est construite pour tester l'influence de la modélisation de la turbulence et des fermetures de premier/second-ordre des flux massiques turbulents.

Les techniques optiques (LDV et DTV) sont déployées pour recueillir des informations statistiques des phases liquide et gazeuse du spray. La campagne expérimentale est réalisée de $x/d_n = 0$ jusqu'à 800. En ce qui concerne la LDV, des gouttelettes d'huile d'olive ($\sim 1 \mu\text{m}$) permettent d'analyser la phase gazeuse. Une distinction entre les gouttes de liquide et ces traceurs est obtenue par une configuration spécifique de la source laser et le paramétrage de la détection des bouffées Doppler (Filtre-BP et le SNR). Dans la zone dispersée, les mesures par DTV permettent d'estimer les vitesses et les tailles des gouttes. Une attention particulière est portée à l'estimation de la profondeur de champ (DOF) afin d'obtenir une corrélation taille-vitesse des gouttes moins biaisée.

Les résultats numériques et expérimentaux concordent pour le champ de vitesse moyenne. Une forte dépendance au modèle de turbulence est trouvée. Cependant, le modèle RSM ne simule pas le comportement du tenseur de Reynolds. En effet, ni l'anisotropie trouvée expérimentalement ($\overline{u_y^2}/\overline{u_x^2} \approx 0.05$), ni la vitesse de glissement liquide-gaz ne peuvent être reproduites ; même avec une fermeture au 2nd-ordre des flux massiques turbulents. Le fort rapport de masse volumique (eau/air), la directionnalité de l'écoulement et la production d'énergie cinétique turbulente peuvent être à l'origine d'une faible dispersion et d'un faible mélange entre les deux fluides. Ce mécanisme n'est pas encore clarifié du point de vue de la modélisation RSM.

Mots clefs : Jet Liquide, Atomisation, Mélange, RANS, Turbulence, LDV/DTV

Résumé de la thèse

Introduction

Une étude sur l'atomisation des jets liquides, pour des applications agricoles, est abordée dans cette thèse. L'étude de ce type d'écoulements est importante non seulement pour réduire la consommation d'eau dans le cas de l'irrigation, mais aussi pour limiter la pollution de l'environnement liée à la pulvérisation de produits phytosanitaires.

Dernièrement, de nombreux travaux ont été réalisés dans ce champ d'application. Ils s'appuient sur des modélisations numériques et/ou des mesures expérimentales. L'objectif est toujours de mieux connaître l'écoulement pour prédire son comportement dans des situations particulières (Al Heidary et al. [1], Salcedo et al. [52], De Luca [11], Belhadef et al. [5], Stevenin et al. [59, 58]).

L'approche numérique permet d'examiner de nombreux cas d'étude plus rapidement que les expériences. Par contre, la validité de cette approche est souvent bornée par des simplifications ou sous-modèles, et principalement par l'incapacité de décrire un cas d'étude avec toutes les complexités d'une application réelle.

L'objectif de cette thèse est donc de concevoir un cas d'étude particulier, où une approche numérique et expérimentale puisse permettre d'analyser l'atomisation d'un jet liquide, similaire à celui d'une buse agricole. L'accent est mis sur l'écoulement moyenné et la turbulence, décrite par le tenseur de Reynolds, où une forte anisotropie est mise en évidence par Stevenin [57].

Méthodologie

Cas d'étude

Un cas d'étude simplifié est construit pour générer un écoulement dans le régime d'atomisation, ce qui correspond aux cas d'irrigation ou de pulvérisation. Le même cas d'étude est utilisé aussi bien pour les simulations numériques que pour la campagne expérimentale. Des simplifications sont faites pour rendre plus compatibles les conditions aux limites entre les expériences et les cas simulés.

Une buse ronde de diamètre $d_n = 1.2 \text{ mm}$ est alors construite avec une longueur $L_n = 50d_n$ pour assurer un écoulement développé à l'intérieur. La buse est alignée avec la gravité (vers le bas) ; l'écoulement est alors statistiquement axisymétrique. Le fluide de travail est de l'eau déminéralisée, injectée dans l'air au repos, où toutes les propriétés physiques sont considérées sous conditions normales (20°C, 1 atm). L'injecteur est construit en verre borosilicate, ce qui

donne un accès optique à l'écoulement interne et impose une rugosité de paroi négligeable. La vitesse débitante d'injection est fixée à $\bar{u}_J = 35 \text{ m/s}$. Avec les propriétés physiques et la géométrie de la buse, le nombre de Reynolds au point d'injection est $Re_L = \frac{\bar{u}_J d_n}{\nu_L} = 41833$, et le nombre de Weber $We_G = \frac{\rho_G \bar{u}_J^2 d_n}{\sigma_{L-G}} = 24.3$. Cette condition génère un écoulement turbulent à l'intérieur de la buse et un régime d'atomisation turbulent en sortie. La rupture/fragmentation du liquide est alors pilotée par la turbulence de l'écoulement, devant les effets aérodynamiques (Dumouchel [16]).

L'écoulement à deux phases est étudié par modélisation numérique et par des techniques expérimentales. Une approche U-RANS (*Unsteady Reynolds Averaged Navier-Stokes Equations*) est choisie pour décrire l'écoulement de mélange, en moyenne de Favre. L'aire interfaciale du liquide-gaz est décrite par un modèle Eulérien. Pour comparer avec le modèle, des mesures par les méthodes optiques de LDV (Vélocimétrie Laser Doppler - Laser Doppler Velocimetry) et DTV (Vélocimétrie par Suivi des Gouttes - Droplet Tracking Velocimetry) par images d'ombroscopie sont effectuées. Une comparaison entre les deux approches est construite en regard des champs de vitesse moyens et turbulents.

Modélisation

Pour décrire le fluide à deux phases, une formulation Eulérienne mono-fluide de mélange est utilisée (Vallet et al. [60], Demoulin et al. [14], Beau [4], Lebas et al. [40], Duret et al. [17]). Cette approche est valide sous deux conditions : le nombre de Reynolds de l'écoulement doit être suffisamment grand, donc la turbulence est prédominante ; et le nombre de Weber est grand aussi, ce qui permet de négliger les forces interfaciales devant le mélange turbulent du liquide-gaz. Ces hypothèses permettent d'avoir recours à une seule équation pour la conservation de la quantité de mouvement et la conservation de la masse. Cependant, une équation supplémentaire est nécessaire pour décrire le mélange turbulent des deux phases, considéré ici en moyennes de Favre :

$$\frac{\partial \bar{\rho}}{\partial t} + \frac{\partial \bar{\rho} \tilde{u}_i}{\partial x_i} = 0; \quad (1)$$

$$\frac{\partial \bar{\rho} \tilde{u}_i}{\partial t} + \frac{\partial \bar{\rho} \tilde{u}_i \tilde{u}_j}{\partial x_j} = -\frac{\partial \bar{p}}{\partial x_i} + \bar{\rho} g_i + \frac{\partial \tilde{\tau}_{ij}}{\partial x_j} - \frac{\partial \bar{\rho} \widetilde{u_i'' u_j''}}{\partial x_j}; \quad (2)$$

$$\frac{\partial \bar{\rho} \tilde{Y}}{\partial t} + \frac{\partial \bar{\rho} \tilde{u}_i \tilde{Y}}{\partial x_i} = -\frac{\partial \bar{\rho} \widetilde{u_i'' Y''}}{\partial x_i}. \quad (3)$$

Le système d'équations est décrit en coordonnées cartésiennes ($i = 1, 2, 3$) où les variables sont en unités-SI. Dans les équations, \tilde{u}_i est la vitesse de mélange, \bar{p} la pression moyenne, \tilde{Y} la fraction massique du liquide et g_i la force de gravité. La masse volumique de mélange s'exprime à partir de celles du liquide et du gaz $\bar{\rho} = \bar{Y} \rho_L + (1 - \bar{Y}) \rho_G$, où la fraction volumique de liquide est $\bar{Y} = \frac{\bar{\rho} \tilde{Y}}{\rho_L}$. Le tenseur des contraintes visqueuses moyennes est considéré très petit devant la turbulence, mais il est retenu et pris en compte à partir de la formulation de Stokes $\tilde{\tau}_{ij} = \bar{\mu} \left(\frac{\partial \tilde{u}_i}{\partial x_j} + \frac{\partial \tilde{u}_j}{\partial x_i} - \frac{2}{3} \frac{\partial \tilde{u}_k}{\partial x_k} \delta_{ij} \right)$, où la viscosité dynamique de mélange est simplement $\bar{\mu} = \bar{Y} \mu_L + (1 - \bar{Y}) \mu_G$ (et $\bar{\nu} = \frac{\bar{\mu}}{\bar{\rho}}$). La modélisation de la turbulence intervient dans la description

du tenseur de Reynolds $\widetilde{u_i'' u_j''}$ et du flux turbulent de masse $\widetilde{u_i'' Y''}$. Ce sont les seules quantités qui ont besoin de modèles de fermeture. Dans cette formulation Eulérienne de l'atomisation de jets liquides, une équation supplémentaire est nécessaire pour décrire le transport de l'aire interfaciale liquide-gaz par unité de volume $\bar{\rho}\tilde{\Omega}$. Cette quantité permet d'avoir une estimation de la taille moyenne des gouttes en fonction du diamètre moyen de Sauter $\bar{d}_{[32]}$.

Turbulence

Deux formulations RANS sont considérées : $k - \epsilon$ et $R_{ij} - \epsilon$. La première, k-Epsilon ($k - \epsilon$), est une transposition directe du modèle original de Jones and Launder [34] sous une formulation à masse volumique variable (voir Chassaing et al. [8]). Le tenseur de Reynolds s'exprime alors suivant :

$$-\bar{\rho}\widetilde{u_i'' u_j''} + \frac{2}{3}\bar{\rho}\tilde{k}\delta_{ij} = \mu_t \left(\frac{\partial \tilde{u}_i}{\partial x_j} + \frac{\partial \tilde{u}_j}{\partial x_i} - \frac{2}{3} \frac{\partial \tilde{u}_k}{\partial x_k} \delta_{ij} \right); \quad (4)$$

où $\mu_t = C_\mu \bar{\rho} \frac{\tilde{k}^2}{\bar{\epsilon}}$ est la viscosité turbulente de mélange, décrite avec un modèle à deux équations où $C_\mu = 0.09$ est une constante de proportionnalité. Les deux équations sont : une pour l'énergie cinétique turbulente (\tilde{k}) ; et l'autre pour le taux de dissipation de \tilde{k} ($\bar{\epsilon}$).

$$\frac{\partial \bar{\rho}\tilde{k}}{\partial t} + \frac{\partial \bar{\rho}\tilde{u}_i \tilde{k}}{\partial x_i} = \frac{\partial}{\partial x_j} \left[\left(\bar{\mu} + \frac{\mu_t}{\sigma_k} \right) \frac{\partial \tilde{k}}{\partial x_j} \right] - \bar{\rho}\widetilde{u_i'' u_j''} \frac{\partial \tilde{u}_i}{\partial x_j} - \bar{\rho}\bar{\epsilon} + \bar{\rho} \left(\frac{1}{\rho_g} - \frac{1}{\rho_l} \right) \widetilde{u_i'' Y''} \frac{\partial \bar{p}}{\partial x_i}; \quad (5)$$

$$\begin{aligned} \frac{\partial \bar{\rho}\bar{\epsilon}}{\partial t} + \frac{\partial \bar{\rho}\bar{\epsilon}\tilde{u}_i}{\partial x_i} &= \frac{\partial}{\partial x_i} \left[\left(\bar{\mu} + \frac{\mu_t}{\sigma_\epsilon} \right) \frac{\partial \bar{\epsilon}}{\partial x_i} \right] - C_{\epsilon 1} \frac{\bar{\epsilon}}{\tilde{k}} \bar{\rho}\widetilde{u_i'' u_j''} \frac{\partial \tilde{u}_i}{\partial x_j} - C_{\epsilon 2} \bar{\rho} \frac{\bar{\epsilon}^2}{\tilde{k}} \\ &+ C_{\epsilon 3} \frac{\bar{\epsilon}}{\tilde{k}} \bar{\rho}' \frac{\partial \tilde{u}_k''}{\partial x_k} - C_{\epsilon 4} \frac{\bar{\epsilon}}{\tilde{k}} \bar{\rho} \left(\frac{1}{\rho_g} - \frac{1}{\rho_l} \right) \widetilde{u_i'' Y''} \frac{\partial \bar{p}}{\partial x_i} - C_{\epsilon 5} \bar{\rho}\bar{\epsilon} \frac{\partial \tilde{u}_k}{\partial x_k}; \end{aligned} \quad (6)$$

où $C_{\epsilon 1} = 1.60$ (voir Dally et al. [9]), $C_{\epsilon 2} = 1.92$, $C_{\epsilon 3} = 0.0$ (n'est pas modélisé), $C_{\epsilon 4} = 1.0$ et $C_{\epsilon 5} = 1.0$ (voir Chassaing et al. [8]). Les nombres de Schmidt turbulents sont $\sigma_k = 1.0$ et $\sigma_\epsilon = 1.3$.

De la même façon, le deuxième modèle avec une fermeture au second ordre correspond à une version à masse volumique variable du RSM (Reynolds Stress Model, $R_{ij} - \epsilon$), originalement proposée par Launder et al. [39] :

$$\frac{\partial \bar{\rho}\widetilde{u_i'' u_j''}}{\partial t} + \frac{\partial \bar{\rho}\tilde{u}_l \widetilde{u_i'' u_j''}}{\partial x_l} - \frac{\partial}{\partial x_l} \left[C_S \bar{\rho} \frac{\tilde{k}}{\bar{\epsilon}} \widetilde{u_l'' u_k''} \frac{\partial \widetilde{u_i'' u_j''}}{\partial x_k} \right] = \bar{\rho}P_{ij} + \bar{\rho}\Phi_{ij} + \Sigma_{ij} - \bar{\epsilon}_{ij}. \quad (7)$$

Pour le terme diffusif, on impose $C_S = 0.22$. Le terme de production est séparé en deux parties. Le premier reste celui d'origine :

$$P_{ij} = - \left(\widetilde{u_i'' u_k''} \frac{\partial \tilde{u}_j}{\partial x_k} + \widetilde{u_j'' u_k''} \frac{\partial \tilde{u}_i}{\partial x_k} \right); \quad (8)$$

et le deuxième ne tient compte que des variations de masse volumique couplant le flux turbulent de masse avec le gradient pression :

$$\Sigma_{ij} = \bar{\rho} \left(\frac{1}{\rho_g} - \frac{1}{\rho_l} \right) \left[\widetilde{u_i'' Y''} \frac{\partial \bar{p}}{\partial x_j} + \widetilde{u_j'' Y''} \frac{\partial \bar{p}}{\partial x_i} \right]. \quad (9)$$

Un modèle linéaire pour la corrélation des fluctuations pression-déformation Φ_{ij} est utilisé selon la formulation suivante (Rotta [50], Launder et al. [39], Vallet et al. [60]) :

$$\begin{aligned} \Phi_{ij} &= \phi_{ij}^{(slow)} + \phi_{ij}^{(rapid,P)} + \phi_{ij}^{(rapid,\Sigma)} \\ &= -C_1 \frac{\bar{\epsilon}}{\bar{k}} \left(\widetilde{u_i'' u_j''} - \frac{2}{3} \tilde{k} \delta_{ij} \right) - C_2 \left(P_{ij} - \frac{1}{3} P_{ll} \delta_{ij} \right) - C_3 \frac{1}{\bar{\rho}} \left(\Sigma_{ij} - \frac{1}{3} \Sigma_{ll} \delta_{ij} \right); \end{aligned} \quad (10)$$

où $\phi_{ij}^{(slow)}$ est le terme de retour à l'isotropie, avec $C_1 = 1.8$; et $\phi_{ij}^{(rapid)}$ est l'isotropisation des termes de production, avec $C_2 = 0.6$ et $C_3 = 0.75$.

Finalement, le taux de dissipation (ϵ) est modélisé par l'équation 6, mais deux variations sont étudiées pour modéliser le tenseur du taux de dissipation ($\bar{\epsilon}_{ij}$). La première option est de prendre les termes diagonaux, ce qui fait une équivalence parfaite avec le taux de dissipation de \tilde{k} . La deuxième option est de faire apparaître un facteur d'anisotropie dans la dissipation, comme dans la formulation proposée par Rotta [50]. Ces deux variations s'expriment suivant :

$$\bar{\epsilon}_{ij} = \frac{2}{3} \bar{\rho} \bar{\epsilon} \delta_{ij}; \text{ ou} \quad (11)$$

$$\bar{\epsilon}_{ij} = \bar{\rho} \frac{\widetilde{u_i'' u_j''}}{\tilde{k}} \bar{\epsilon}. \quad (12)$$

Avec cette dernière considération, la modélisation RSM est alors appelée $R_{ij} - \epsilon$ quand la première formulation de base est utilisée, et $R_{ij} - \epsilon_{ij}$ quand l'anisotropie est prise en compte dans $\bar{\epsilon}_{ij}$.

Flux turbulent de masse

Trois types de modélisation sont considérés pour décrire $\widetilde{u_i'' Y''}$: deux variations d'une fermeture au premier ordre ; et une fermeture au second ordre où une équation de transport est à résoudre pour les flux.

Pour la fermeture au premier-ordre, les deux formulations suivantes sont retenues, appelées Y_{mod0} et Y_{mod1} respectivement (Belhadef et al. [5]) :

$$-\bar{\rho} \widetilde{u_i'' Y''} = \frac{\mu_t}{\sigma_Y} \frac{\partial \tilde{Y}}{\partial x_i}; \quad (13)$$

$$-\bar{\rho} \widetilde{u_i'' Y''} = C_Y \bar{\rho} \frac{\tilde{k}}{\bar{\epsilon}} \widetilde{u_i'' u_j''} \frac{\partial \tilde{Y}}{\partial x_j}. \quad (14)$$

Au lieu de la valeur standard pour le nombre de Schmidt turbulent $\sigma_Y \approx 0.9$, une valeur modifiée est proposée par Stevenin et al. [59], en fonction d'un facteur d'anisotropie important dans

le tenseur de Reynolds, trouvé expérimentalement. En effet, si $\frac{\partial \tilde{Y}}{\partial x_2} \gg \frac{\partial \tilde{Y}}{\partial x_1}$, et la composante principale dans la direction radiale est $\tilde{u}_2'' \approx 0.082\tilde{k}$, Y_{mod1} devient Y_{mod0} avec $\sigma_Y \approx 5.5$. Le modèle de fermeture au second ordre, appelé Y_{mod2} , est basé sur la formulation proposée par Beau [4]. Une équation de transport est résolue pour $\tilde{u}_i'' \tilde{Y}''$. Le modèle inclut une description des forces de traînée en fonction de la taille des particules (gouttes) dans l'écoulement :

$$\begin{aligned} \frac{\partial \bar{\rho} \tilde{u}_i'' \tilde{Y}''}{\partial t} + \frac{\partial \bar{\rho} \tilde{u}_j \tilde{u}_i'' \tilde{Y}''}{\partial x_j} = \frac{\partial}{\partial x_j} \left(\frac{\mu_t}{\sigma_F} \frac{\partial \tilde{u}_i'' \tilde{Y}''}{\partial x_j} \right) \\ - C_{F1} \bar{\rho} \tilde{u}_j'' \tilde{Y}'' \frac{\partial \tilde{u}_i}{\partial x_j} - C_{F2} \bar{\rho} \tilde{u}_i'' \tilde{u}_j'' \frac{\partial \tilde{Y}}{\partial x_j} - C_{F3} \bar{Y}'' \frac{\partial \bar{p}}{\partial x_i} + C_{F4} \bar{F}_{Drag,i}; \end{aligned} \quad (15)$$

où $C_{F1} = 4.0$, $C_{F2} = 0.1$, $C_{F3} = 0.0$, $C_{F4} = 4.0$ et $\sigma_F = 0.9$.

La traînée est calculée à partir de la formulation de Schiller-Naumann. Le coefficient de traînée est fonction du nombre de Reynolds basé sur la vitesse de glissement vue par les gouttes :

$$\bar{F}_{Drag,i} = -\frac{\bar{\rho} \tilde{Y}}{\tau_R} (\tilde{u}_{i,L} - \tilde{u}_{i,G} - \tilde{u}_{i,D}); \quad (16)$$

$$\tau_R = \frac{\rho_L d_L^2}{18\mu_G} (1 + 0.15 Re_d^{0.687})^{-1}; \quad (17)$$

$$Re_d = \frac{\|\tilde{u}_{i,L} - \tilde{u}_{i,G} - \tilde{u}_{i,D}\| d_L}{v_G}; \quad (18)$$

$$\tilde{u}_{i,D} = \frac{1}{\tilde{Y}(1 - \tilde{Y})} \frac{v_t}{\sigma_Y} \frac{\partial \tilde{Y}}{\partial x_i}; \quad (19)$$

où d_l est une longueur caractéristique représentant le diamètre de la population de gouttes, prise comme le diamètre équivalent $d_{[32]}$ du modèle $\bar{\rho}\tilde{\Omega}$. La vitesse de dérive $\tilde{u}_{i,D}$ est calculée en utilisant le modèle au premier ordre Y_{mod0} .

Transport de l'aire interfaciale

Pour le transport de l'aire interfaciale moyenne par unité de volume $\bar{\rho}\tilde{\Omega}$, la version décrite par Lebas et al. [40] est retenue. Des simplifications sont faites en négligeant les termes liés à la collision/coalescence et au changement de phase :

$$\frac{\partial \bar{\rho}\tilde{\Omega}}{\partial t} + \frac{\partial \bar{\rho}\tilde{\Omega}\tilde{u}_i}{\partial x_i} = \frac{\partial}{\partial x_i} \left(\frac{\mu_t}{\sigma_\Omega} \frac{\partial \tilde{\Omega}}{\partial x_i} \right) + \alpha \frac{\bar{\rho}\tilde{\Omega}\tilde{e}}{\tilde{k}} \left(1 - \frac{\tilde{\Omega}}{\tilde{\Omega}^*} \right); \quad (20)$$

où $\tilde{\Omega}^*$ est la valeur d'équilibre quand $We^* = 1.0$ (Duret et al. [17]) :

$$\tilde{\Omega}^* = 4 \frac{0.5(\rho_L + \rho_G)\bar{Y}(1 - \bar{Y})\tilde{k}}{\sigma\bar{\rho}We^*}. \quad (21)$$

Les paramètres du modèle sont ceux par défaut, donc $\alpha = 1.0$ et $\sigma_\Omega = 1.0$. De la même façon que dans le modèle original proposé par Vallet et al. [60], $\tilde{\Omega}$ est lié au diamètre moyen de

Sauter $d_{[32]}$ par la relation suivante :

$$d_{[32]} = \frac{\rho_L \bar{Y}}{\bar{\rho} \tilde{\Omega}}. \quad (22)$$

Solveur numérique

Le système d'équations est codé dans un solveur qui utilise la bibliothèque des outils *Open-FOAM*. Une modification dans la boucle PISO (solveur de la pression) est ajoutée pour prendre en compte la divergence non nulle de la vitesse en moyenne de Favre. Cet ajout induit un couplage direct entre le modèle de flux turbulent de masse et la *QDM*.

Comme le cas est résolu de façon non-stationnaire (Modèle U-RANS), un temps de simulation de $t = 0.3 \text{ s}$ est choisi pour l'ensemble des calculs. Ce temps est suffisant pour avoir une solution établie dans tout le domaine considéré : de $x/d_n = -50$ dans la buse (injection en amont), en passant par $x/d_n = 0$ (sortie de la buse), jusqu'au $x/d_n = 1500$ dans le domaine d'atomisation.

Un test de maillage est effectué pour s'assurer que les résultats, pour l'ensemble des modèles considérés, sont indépendants de la taille des mailles. Un maillage hexaédrique est alors construit dont le nombre de mailles est de l'ordre de 6×10^6 . Les conditions aux limites et initiales sont dérivées du cas d'étude expérimentale (vitesse débitante $\bar{u}_J = 35 \text{ m/s}$ d'eau i.e. $\bar{Y}_J = 1$) et sont imposées à $x/d_n = -50$, avec une intensité turbulente de $I_t = 4\%$.

Les cas de simulation sont calculés sur un cluster HPC au CINES sous l'allocation c20152b7363 et c20162b7363 du GENCI (Grand Équipement National de Calcul Intensif) en France.

Campagne expérimentale

Les techniques de mesure optiques LDV et DTV par ombroscopie sont utilisées pour caractériser l'atomisation du jet décrit précédemment (Figure 1b et 1c).

Le système LDV est fourni par Dantec Dynamics (LDV-2C). Une source laser ion-argon de $488 \text{ nm}@1.8 \text{ W}$ et $514.5 \text{ nm}@2.8 \text{ W}$ Coherent 306S permet de mesurer les deux composantes de vitesse. Une optique de 310 mm de distance au plan focal est utilisée comme émetteur, et de 400 mm pour le récepteur. Les deux sont écartées d'un angle de 55° , ce qui permet de maximiser le taux d'acquisition. L'analyseur de spectre des bouffés Doppler (BSA) est un modèle P60, également fourni par Dantec-Dynamics.

Les mesures par LDV sont effectuées en deux campagnes différentes : une pour mesurer dans la phase liquide ; et l'autre pour mesurer dans la phase gazeuse, en utilisant des gouttelettes d'huile d'olive ($d \sim 1 - 2 \mu\text{m}$) comme traceurs (Figure 1b). Dans ce dernier cas, une configuration particulière du BSA permet de différencier la vitesse purement du gaz de celle des gouttes d'eau qui se trouvent dans le mélange (Mychkovsky et al. [43] [42]).

Les mesures par DTV sont effectuées par une technique d'ombroscopie. Un système *Shadow-Strobe* de Dantec-Dynamics est utilisé pour acquérir les images. Le système est composé d'une caméra CCD PIV/DTV HiSense 4M-C, avec une optique Canon MP-E 65 mm f/2.8, où une source laser Litron Nd-YAG de 135 mJ (532 nm) est couplée avec un diffuseur/collimateur qui génère un fond d'image d'intensité lumineuse uniforme et non-cohérente. Des paires

d'images (*frames*) sont acquises à une fréquence de $f_a = 5 \text{ Hz}$, où le temps entre chaque frame est défini entre $tbp = 5 - 20 \mu\text{s}$, en fonction de la vitesse moyenne des objets dans l'image qui varie suivant la distance au centre ($y/d_n = 0 - 32$). La résolution est de 139 pix/mm , ce qui correspond à une taille d'image de $14.73 \times 14.73 \text{ mm}^2$ ($2048 \times 2048 \text{ pix}$).

Cette méthode est basée sur les travaux de Yon [65], Fdida et Blaisot [20] et Stevenin et al. [58] pour l'estimation de tailles de gouttes dans un spray poli-disperse. Les vitesses sont calculées à partir de l'algorithme *SoftAssign* proposé par Gold et al. [24]. Cet algorithme a été adapté et implémenté lors de ces travaux en utilisant le *Image Processing Toolbox* de MATLAB, à l'aide d'une carte graphique *nVidia CUDA*. La Figure 1c montre une photo d'ombroscopie du spray, où l'algorithme par DTV est appliqué aux gouttes détectées dans l'image. L'estimation des tailles (contours) et vitesses (vecteurs) y est reportée.

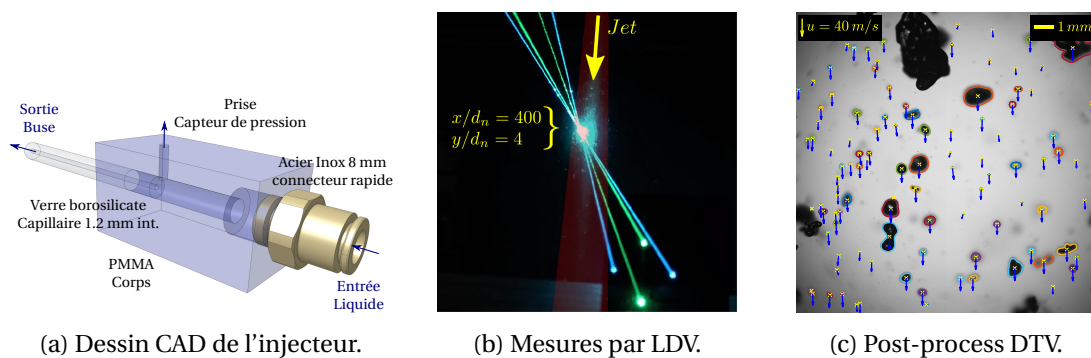


FIGURE 1 – Campagne expérimentale en utilisant une buse de $d_n = 1.2 \text{ mm}$.

Résultats et analyse

Les premiers résultats expérimentaux sont analysés pour définir les paramètres de base caractérisant le comportement des jets. Le premier est l'estimation de la longueur de rupture du coeur liquide \bar{L}_c . À partir d'une analyse similaire à celle de Wu et Faeth [63] et Hoyt et Taylor [29], la Figure 2 met en évidence le régime turbulent de rupture. La valeur expérimentale calculée à partir de la moyenne des images $\bar{L}_c/d_n = 219$ est proche de celle estimée à partir de la relation $\bar{L}_c/d_n = 8.51 We_L^{0.31} = 203$ (Sallam et al. [53]).

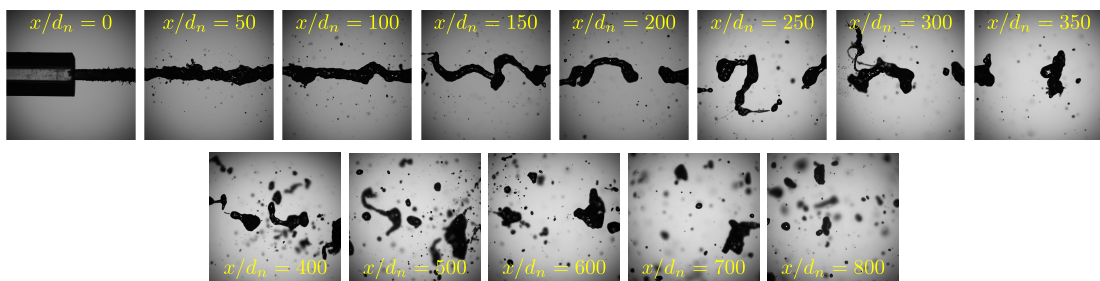


FIGURE 2 – Ombroscopie au niveau de l'axe du jet : de $x/d_n = 0$ jusqu'à $x/d_n = 800$.

Dans la zone dispersée du jet (de $x/d_n = 400$ jusqu'à $x/d_n = 800$), des profils radiaux sont

acquis par LDV et DTV. L'analyse conjointe des vitesses et tailles de gouttes issue de la campagne expérimentale est montrée à la Figure 3, où des histogrammes (normalisés en pdf) sur un profil radial à $x/d_n = 800$ sont construits. Ces résultats mettent en évidence l'existence d'une forte vitesse moyenne de glissement entre les deux phases. En plus, en fonction de leur taille, les gouttes réagissent de façon très différente à la turbulence. À partir de ces informations, les quantités moyennes décrites dans la Table 1 sont construites pour comparer aux résultats numériques. Pour la DTV, deux types de moyennes sont calculées : pondérées ou non par le diamètre des gouttes.

TABLE 1 – Quantités moyennées à partir des données expérimentales.

Méthode	Quantité moyennée	Formule
LDV-Liq.	Vitesse	$\bar{u}_{i,L} = \frac{1}{n} \sum_{k=1}^n u_{i,\{k \in Liq\}}$
	T. de Reynolds	$\bar{R}_{ij,L} = \frac{1}{n} \sum_{k=1}^n (u_{i,\{k \in Liq\}} - \bar{u}_{i,L})(u_{j,\{k \in Liq\}} - \bar{u}_{j,L})$
LDV-Gaz	Vitesse	$\bar{u}_{i,G} = \frac{1}{n} \sum_{k=1}^n u_{i,\{k \in Gas\}}$
	T. de Reynolds	$\bar{R}_{ij,G} = \frac{1}{n} \sum_{k=1}^n (u_{i,\{k \in Gas\}} - \bar{u}_{i,G})(u_{j,\{k \in Gas\}} - \bar{u}_{j,G})$
DTV	Vitesse	$\bar{u}_i = \frac{1}{n} \sum_{k=1}^n u_{i,k}$
	T. de Reynolds	$\bar{R}_{ij} = \frac{1}{n} \sum_{l=1}^n (u_{i,l} - \bar{u}_i)(u_{j,l} - \bar{u}_j)$
	Vitesse pondérée	$\bar{u}_{i,d} = \frac{\sum_{k=1}^n d_{[30],k} u_{i,k}}{\sum_{k=1}^n d_{[30],k}}$
	T. de Reynolds pondérée	$\bar{R}_{ij,d} = \frac{\sum_{l=1}^n d_{[30],l} (u_{i,l} - \bar{u}_i)(u_{j,l} - \bar{u}_j)}{\sum_{l=1}^n d_{[30],l}}$
	Vitesse par classe	$\bar{u}_{i,(k)} = \frac{1}{n} \sum_{l=1}^n u_{i,\{l \in (k)\}}$
	T. de Reynolds par classe	$\bar{R}_{ij,(k)} = \frac{1}{n} \sum_{l=1}^n (u_{i,\{l \in (k)\}} - \bar{u}_{i,(k)})(u_{j,\{l \in (k)\}} - \bar{u}_{j,(k)})$

TABLE 2 – Partition de la population de gouttes par classe de diamètre.

Classe 1 :	$d_{[30]} \leq 0.10 \text{ mm}$
Classe 2 :	$0.10 \text{ mm} < d_{[30]} \leq 0.25 \text{ mm}$
Classe 3 :	$0.25 \text{ mm} < d_{[30]} \leq 0.50 \text{ mm}$
Classe 4 :	$0.50 \text{ mm} < d_{[30]} \leq 0.75 \text{ mm}$
Classe 5 :	$0.75 \text{ mm} < d_{[30]} \leq 1.00 \text{ mm}$
Classe 6 :	$1.00 \text{ mm} < d_{[30]}$

Les campagnes de mesure par LDV du liquide-gaz sont comparées à celle de la DTV. La façon de construire les quantités moyennes a une influence sur les résultats dans la représentation de la phase liquide. Le volume de mesure de la LDV est petit par rapport à l'aire d'intégration des données de DTV, ce qui la rend plus précise dans l'espace. Pour avoir une précision supplémentaire dans la DTV, une décomposition en sous-images est effectuée, où les gouttes détectées sont réparties dans 5 divisions horizontales dans l'image. En plus, pour caractériser le comportement des gouttes en fonction de leur taille, le classement détaillé dans la Table 2 est utilisé.

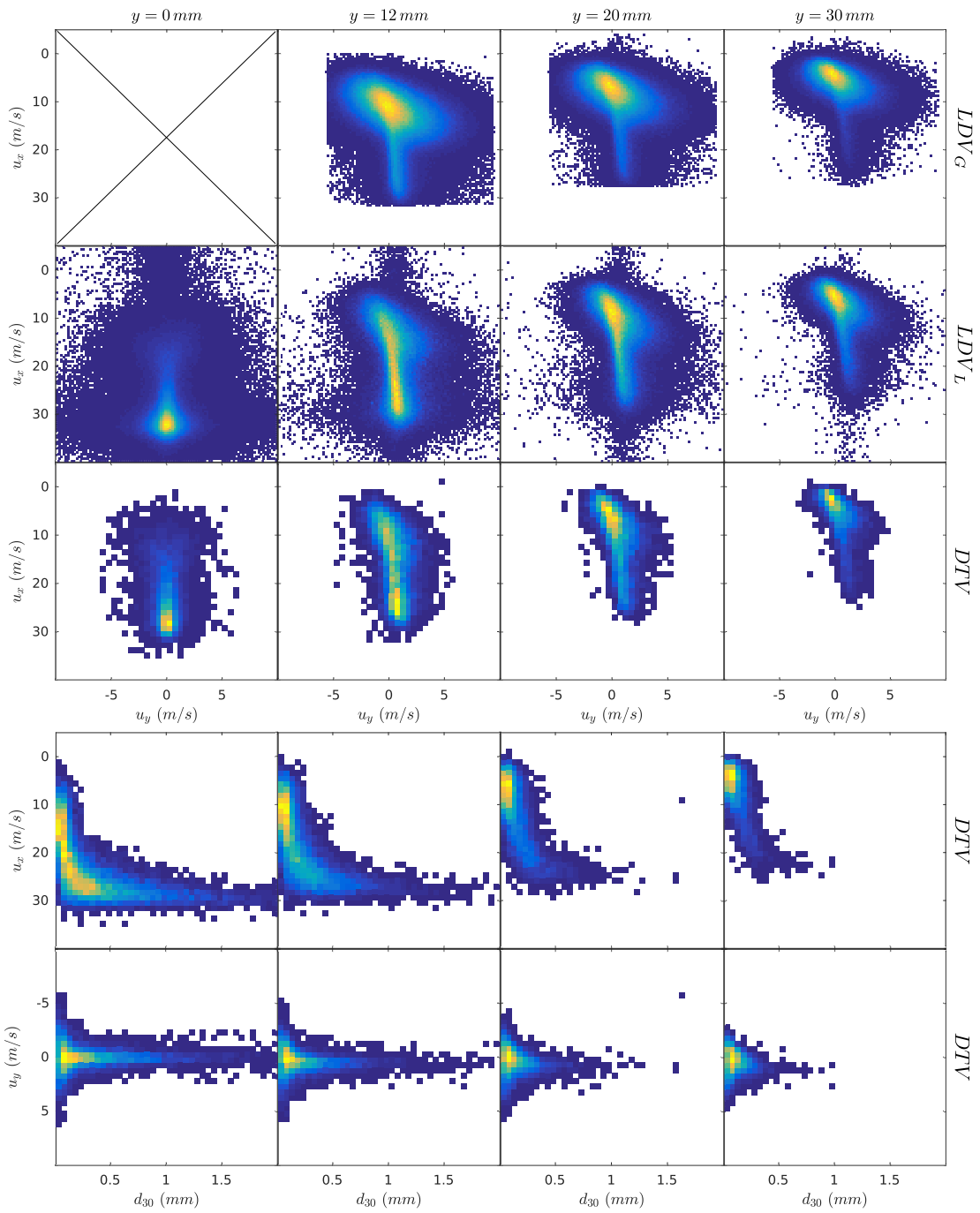


FIGURE 3 – Histogrammes de vitesses et tailles de gouttes (*pdf*) à $x/d_n = 800$. LDV-Gaz, LDV-Liq et DTV.

Les résultats issus, des cas de simulation, des différentes façons de représenter les moyennes de la DTV et de la LDV, sont présentés à la Figure 4. La portée du jet est caractérisée par le taux de décroissance de la vitesse sur l'axe. Ruffin et al. [51] ont mis en évidence que $\frac{\bar{u}_{x,0}}{\bar{u}_j} = \frac{1}{A} \left(\frac{d_n}{x-x_0} \right) \left(\frac{\rho_L}{\rho_G} \right)^b$, avec $b = 0.5$ pour un jet gaz-gaz à masse volumique variable, où $A \approx 0.2$.

Résumé de la thèse

Ici, on obtient $A = 0.021$ par LDV et $A = 0.019$ par DTV, calculés à partir de $x/d_n > 400$. L'étalement du jet est caractérisé par le paramètre $S = \frac{\partial y_{0.5u}}{\partial x}$, où la demi-largeur de la vitesse est définie telle que $\bar{u}_{x,L}(x, y = y_{0.5u}) = \bar{u}_{x,L,0}/2$. Ces valeurs (A et S) sont proches de celles estimées par Stevenin et al. [58] : $A = 0.027$ et $S = 0.024$.

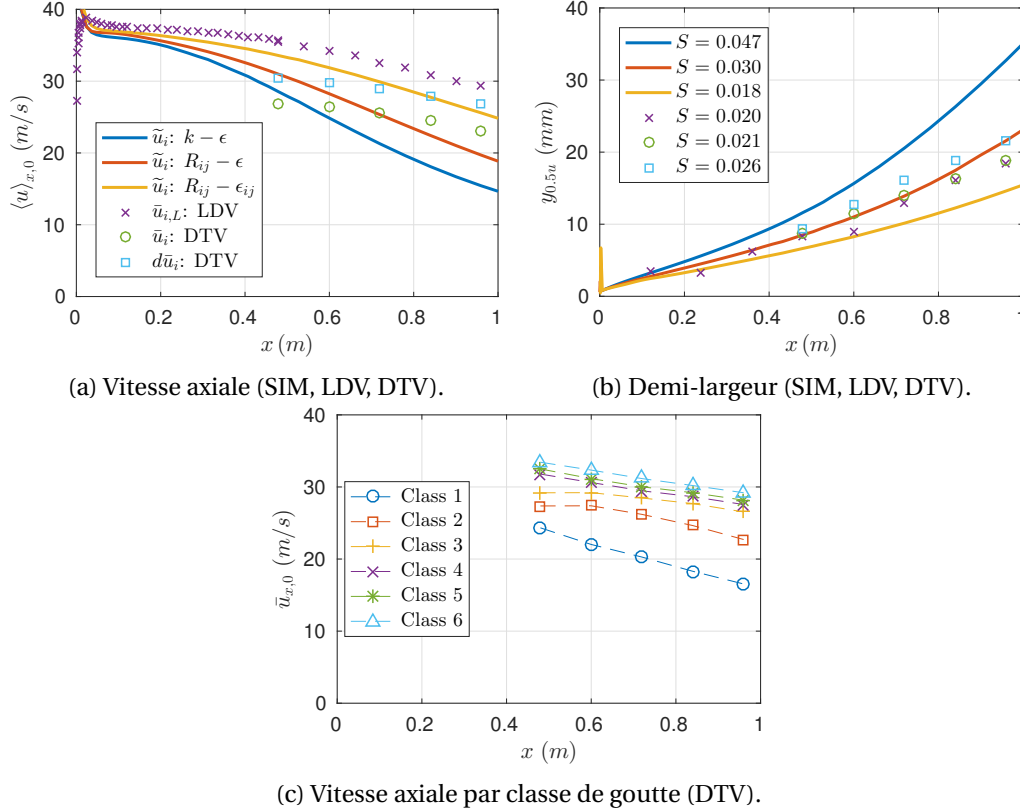


FIGURE 4 – Campagne expérimentale en utilisant une buse de $d_n = 1.2 \text{ mm}$.

Si on considère que la vitesse moyenne calculée à partir de la LDV est la plus précise sur l'axe du jet, l'écart par classe de goutte observée en DTV, met en évidence que, selon la taille, les gouttes vont réagir de façon différente à la turbulence de l'écoulement. Le modèle $R_{ij}-\epsilon_{ij}$ semble être le plus proche des résultats expérimentaux. Cette observation est confortée par la figure 5, où les profils radiaux de vitesse axiale sont comparés. La vitesse axiale de mélange \bar{u}_x doit être une combinaison de la vitesse de la phase liquide $\bar{u}_{x,L}$ et du gaz $\bar{u}_{x,G}$, en fonction de la fraction massique \tilde{Y} . Cette dernière quantité est également montrée à la figure 5, mais issue de la modélisation, comme point référentiel.

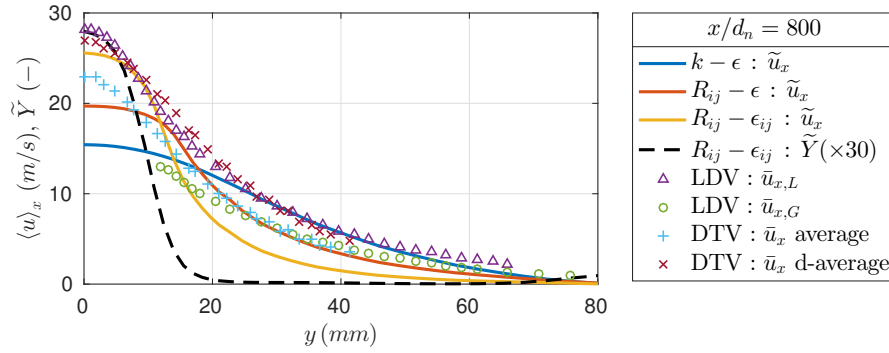


FIGURE 5 – Composante axiale de la vitesse moyenne en fonction de la distance radiale. Comparaison des modèles de turbulence vis à vis des résultats de LDV et DTV.

Autant la vitesse moyenne est très bien représentée par la modélisation U-RANS autant les champs turbulents ne le sont pas. En effet, l'énergie cinétique turbulente est correctement reproduite, mais sa distribution selon les composantes principales du tenseur de Reynolds est plus anisotrope que prévue. La Figure 6 montre un comportement très similaire à celui d'un jet gaz-gaz pour la composante $\langle R \rangle_{11}$ (voir Hussein et al. [30]). Par contre, la composante $\langle R \rangle_{22}$ est très faible, avec un facteur d'anisotropie $\langle R \rangle_{22} / \langle R \rangle_{11} \approx 0.05$. Ce résultat est similaire à celui trouvé par Stevenin et al. [58], mais très différent à celui de El-Asrag and Braun [18] dans un jet d'acétone ou celui de Ferrand et al. [21] dans un jet de gaz avec des particules.

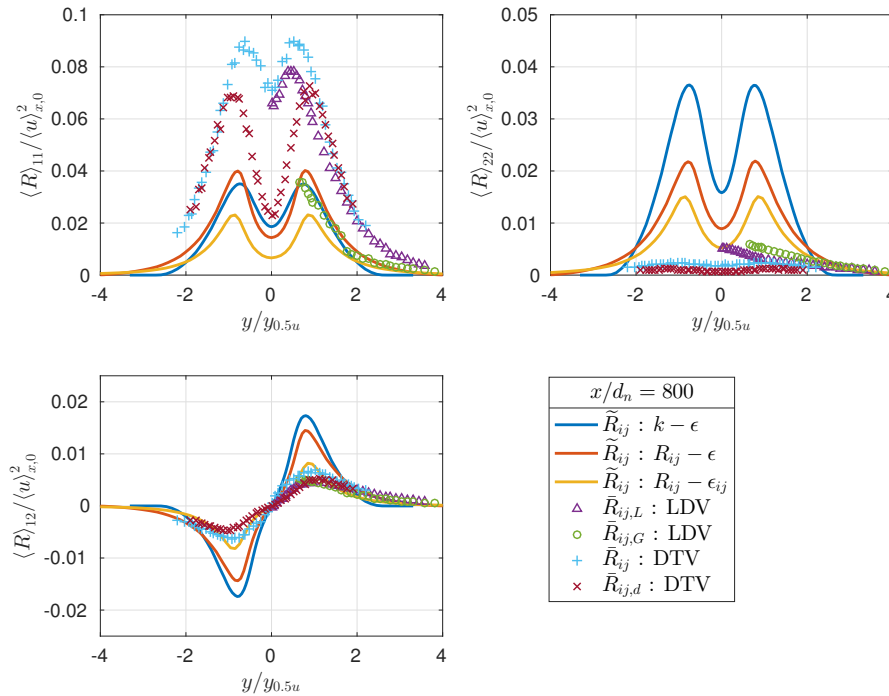


FIGURE 6 – Tenseur de Reynolds en fonction de la distance radiale. Comparaison des modèles de turbulence vis-à-vis des résultats de LDV et DTV.

En se focalisant sur l'analyse du modèle $R_{ij} - \epsilon_{ij}$, avec une fermeture au second ordre pour

$\widetilde{u}_i'' Y''$, une possible source de cette anisotropie peut être la représentation de Σ_{ij} (Éq. 9). En effet, la vitesse de glissement moyenne est directement liée au flux turbulent de masse, avec $\bar{u}_{i,L} - \bar{u}_{i,G} = \frac{\widetilde{u}_i'' Y''}{\bar{Y}(1-\bar{Y})}$, et pourtant, lié au terme de production Σ_{ij} . Par contre, à cause du gradient de pression, c'est seulement le glissement radial qui intervient de manière prépondérante. Aussi, Σ_{ij} n'est pas en cause. Une possible explication pourrait provenir du terme de production P_{ij} . Cependant, ce terme est correctement estimé en fonction de la composante $\langle R \rangle_{12}$ et du champ de vitesse $\langle u \rangle_1$. C'est pour cela que nous remettons en cause le rôle de la redistribution $\phi_{ij}^{(rapid,\Sigma)}$ qui ne permet pas, dans sa formulation actuelle, de diminuer la composante $\langle R \rangle_{22}$ au profit de $\langle R \rangle_{11}$. Cette dernière hypothèse n'a pas pu être explorée dans le cadre de ces travaux.

Conclusions

Les points suivants résument les travaux réalisés au cours de cette thèse et ouvrent sur leurs perspectives :

- Un cas d'étude à échelle réduite est correctement développé pour étudier l'atomisation d'un jet liquide, dans un régime proche de ceux rencontrés en irrigation et pulvérisation de pesticides. Les simplifications faites permettent d'assurer une compatibilité entre les simulations numériques et les mesures expérimentales afin de caractériser finement ce jet diphasique.
- Un modèle U-RANS de mélange eau/air est implémenté à l'aide des outils CFD Open-FOAM pour étudier le cas évoqué. La flexibilité du code permet d'explorer correctement les différents modèles de turbulence et flux turbulent de masse, avec une approche Eulerienne pour la description de l'interface liquide-gaz. Une stratégie de solution est proposée dans l'algorithme numérique, ce qui permet d'avoir une solution compatible avec les équations à masse volumique variable, dans un cas de mélange diphasique incompressible.
- Pour la campagne expérimentale, des mesures par LDV et DTV sont effectuées. La mesure de la vitesse par LDV permet d'estimer les champs de vitesse moyenne et fluctuante dans les deux phases du jet (liquide/gaz). Par ailleurs, la technique de DTV permet de désagréger l'information du liquide (champs de vitesse moyenne et fluctuante) par taille de gouttes. L'ensemble de ces données, obtenues par LDV et DTV, permet de comparer le comportement de ce jet liquide avec les cas de simulation.
- Le comportement dynamique de ce type de jet, décrit par les champs moyens de vitesse, est très différent des jets monophasiques gaz-gaz. La géométrie et le régime d'atomisation produisent une faible décroissance de la vitesse sur l'axe et un faible taux d'étalement du jet. Malgré cela, ces comportements sont bien capturés avec un modèle de turbulence de type RSM. Sur les champs turbulents, un comportement très différent selon la taille de gouttes est trouvé pour la contrainte de Reynolds, où le facteur d'anisotropie peut atteindre $\langle R \rangle_{22} / \langle R \rangle_{11} \approx 0.05$. D'un point de vue numérique, cette anisotropie ne peut pas être bien représentée, ce qui oblige à utiliser un nombre de

Schmidt turbulent assez grand pour le flux turbulent de masse $\sigma_Y = 5.5$.

- Les perspectives de ces travaux sont évoquées en fonction des améliorations sur la précision des résultats expérimentaux et l'exploration de nouveaux cas d'étude numériques. Du côté expérimental, des nouveaux systèmes LDV permettraient de faire une distinction plus précise dans un écoulement diphasique gaz/liquide. L'usage de ce nouveau système sur une configuration de jet similaire à celle-ci paraît pertinente, à la fois pour valider les résultats obtenus, mais aussi pour tester l'efficacité de cette nouvelle technique. Les statistiques sur la population de gouttes obtenues par DTV nécessitent une calibration par rapport à la profondeur de champ. Cette méthode a été mise en oeuvre dans cette thèse mais les corrélations taille/profondeur de champ et corrections des contours en fonction des gradients de niveaux de gris n'ont pas été appliquées aux données DTV. En effet, si la distribution de la population de gouttes est modifiée par la calibration, les champs de vitesse et de fluctuations doivent l'être également. Aussi, une telle correction n'est pas triviale et nécessite de plus amples recherches. Finalement, du côté numérique, une possible source pour augmenter l'anisotropie du tenseur de Reynolds est proposée : modifier le terme de redistribution dans le modèle turbulence RSM ($\phi_{ij}^{(rapid,\Sigma)}$) pourrait permettre d'approcher les résultats expérimentaux.

Contents

Acknowledgements	i
Abstracts (English/Français)	iii
Thesis short version (Français)	vii
List of figures	xxiii
List of tables	xxvii
Nomenclature	xxix
Introduction	1
1 General context	3
1.1 State of the art	4
1.1.1 Atomization in agriculture	4
1.1.2 Liquid jet's fragmentation	6
1.2 Study case	10
Summary	12
2 Numerical modelling	13
2.1 Multiphase flow modelling	14
2.1.1 Eulerian formulation	14
2.1.2 Multiphase average model	15
2.1.3 Mixture RANS equations	16
2.2 Turbulence modelling	18
2.2.1 Reynolds stresses	18
2.2.2 Turbulent mass-flux	22
2.2.3 Eulerian interface	25
2.3 Numerical model	26
2.3.1 OpenFOAM solver	27
2.3.2 Numerical schemes	32
2.3.3 Mesh and convergence	34
2.4 Numerical study cases	36
	xxi

Contents

2.4.1	Cases definitions	37
2.4.2	HPC Cluster	39
2.4.3	Mesh convergence test	41
	Summary	44
3	Experimental campaign	45
3.1	Measurement techniques	47
3.2	Experimental set-up	48
3.3	Measurement set-up	49
3.3.1	LDV set-up	49
3.3.2	DTV set-up	56
	Summary	68
4	Results	69
4.1	Experimental observations	70
4.1.1	Mean velocity field	70
4.1.2	Reynolds stresses	78
4.2	Numerical model analysis	88
4.2.1	RANS turbulence model	89
4.2.2	Epsilon equation behaviour	93
4.2.3	Turbulent mass transport	95
4.2.4	Fully-coupled turbulent model	100
	Summary	103
	Summary, conclusions and perspectives	105
	Bibliography	113

List of Figures

1	Campagne expérimentale en utilisant une buse de $d_n = 1.2\text{ mm}$	xiii
2	Ombroscopie au niveau de l'axe du jet : de $x/d_n = 0$ jusqu'à $x/d_n = 800$	xiii
3	Histogrammes de vitesses et tailles de gouttes (<i>pdf</i>) à $x/d_n = 800$. LDV-Gaz, LDV-Liq et DTV.	xv
4	Campagne expérimentale en utilisant une buse de $d_n = 1.2\text{ mm}$	xvi
5	Composante axiale de la vitesse moyenne en fonction de la distance radiale. Comparaison des modèles de turbulence vis à vis des résultats de LDV et DTV.	xvii
6	Tenseur de Reynolds en fonction de la distance radiale. Comparaison des modèles de turbulence vis-à-vis des résultats de LDV et DTV.	xvii
1.1	Sprinkler for irrigation purposes (Source: www.rainbird.fr).	5
1.2	Reynolds stresses anisotropy factor $\bar{R}_{22}/\bar{R}_{11}$ ($\overline{w'w'}/\overline{u'u'}$) from the DTV measurements performed by Stevenin [57].	6
1.3	Round jet behaviour, stability curve of the breakup length L_c as a function of the average liquid velocity at the nozzle \bar{u}_j . Region A: Dripping regime. Region B: Rayleigh regime. Region C: First wind-induced regime. Region D: Second wind-induced regime. Region E: Atomization regime. (from Dumouchel [16])	8
2.1	Favre average operation over the liquid phase indicator Y and the fluid density ρ . 16	
2.2	OpenFOAM C++ code to solve the momentum conservation equation.	28
2.3	Solution control for the customised solver implemented in OpenFOAM for each time-step Δt	31
2.4	Parameters in finite volume discretization (from the OpenFOAM®Programmer's Guide 2.4.0).	33
2.5	Schematic representation of the mesh, including boundary conditions.	34
2.6	Meshing strategy for a 3D case: Longitudinal slice (left) and transverse slice(right) near the injector nozzle.	36
2.7	Scalability test for the parallel decomposition of a simulation case.	40
2.8	Mesh convergence analysis on the mean axial velocity using three different turbulence models. Radial profile at $x/d_n = 200$	41
2.9	Mesh convergence analysis on the Reynolds stresses using three different turbulence models. Radial profile at $x/d_n = 200$	42
2.10	Mesh convergence analysis on the liquid volume fraction using three different turbulence models. Radial profile at $x/d_n = 200$	42

List of Figures

3.1	Custom transparent $d_n = 1.2\text{ mm}$ nozzle components and real operating conditions.	48
3.2	Schematic representation of the hydraulic system connected to the injector. . .	49
3.3	Schematic of the 2-Component LDV set-up for measuring both the liquid and gas phases. The measurement volume size is shown next to the liquid round-jet dimensions for scale.	50
3.4	Drop-sizing and DTV post-processing on shadowgraph images at $x/d_n = 400$, $y/d_n = 0$: jet centerline (red), $y/d_n = 4$ mark (orange line), droplets detected (coloured contours), velocity-vector (blue arrow) and equivalent diameter ($d_{[30]}$ in μm) written next to each contour detected.	52
3.5	Bi-variate histograms of both velocity components for the liquid phase (blue, left) and the gas phase (green, right). Mean values on red line levels.	52
3.6	Convergence analysis of the Reynolds stresses on the liquid phase at $[x/d_n = 400, y/d_n = 4]$	54
3.7	Convergence analysis of the Reynolds stresses on the gas phase at $[x/d_n = 400, y/d_n = 4]$	55
3.8	Schematic view of the measurement points for the LDV campaign in the study case.	55
3.9	Experimental set-up of the DTV system using shadow images.	56
3.10	Shadow images at the jet centerline from $x/d_n = 0$ to $x/d_n = 800$	57
3.11	Probability distribution of the liquid column average breakup length \bar{L}_c as a function of the normalised distance from the nozzle.	57
3.12	Shadow image segmentation using MATLAB toolboxes. Image post-processing at $[x/d_n = 800, y/d_n = 12]$	58
3.13	Sub-image analysis on a detected droplet. Local contours and principal axis. . .	59
3.14	Custom DTV post-processing algorithm. Image centre at $x/d_n = 600, y/d_n = 0$. . .	60
3.15	ThorLabs grid distortion target. 3in x 3in, 125 to 2000 μm grid spacings, soda lime glass.	61
3.16	Calibration using a commercial optical target.	61
3.17	Convergence analysis on the mean velocity by droplet's class diameters. Sub-image count at $[x/d_n = 600, y = 0\text{ mm}]$	64
3.18	Convergence analysis on the Reynolds stresses by droplet's class diameters. Sub-image count at $[x/d_n = 600, y = 0\text{ mm}]$	65
3.19	Bi-variate histograms normalised as a <i>pdf</i> for: u_x - u_y , u_x - $d_{[30]}$ and u_y - $d_{[30]}$. Sub-image count at $[x/d_n = 600, y = 0\text{ mm}]$	66
3.20	Super-resolution profile reconstruction by overlapping of sub-image data. Blue zones are kept, red are discarded. Example at $x/d_n = 600$	67
3.21	Schematic view of the measurement points for the DTV campaign.	67
4.1	Mean velocity axial profiles from experimental observations.	71
4.2	DTV. Mean liquid axial velocity along the centerline $\bar{u}_{x,0}$ by droplets class diameters.	72

4.3	Axial velocity profile against radial distance at $x/d_n = 0$	73
4.4	Liquid centerline axial velocity decay rate against axial distance.	73
4.5	Velocity field from the Liquid and Gas LDV campaign. Profiles against radial distance from $x/d_n = 400$ to $x/d_n = 800$	74
4.6	Mean axial and lateral velocities against radial distance. DTV radial profiles from $x/d_n = 400$ to $x/d_n = 800$	75
4.7	Mean axial velocity by droplet's class diameter against radial distance. DTV <i>Average</i> radial profiles from $x/d_n = 400$ to $x/d_n = 800$	76
4.8	Mean lateral velocity by droplet's class diameter against radial distance. DTV <i>Average</i> radial profiles from $x/d_n = 400$ to $x/d_n = 800$	77
4.9	Reynolds stresses against radial distance. LDV liquid, gas and slip components radial profiles at $x/d_n = 400$ and $x/d_n = 800$	79
4.10	Shear stress over turbulent kinetic energy. LDV liquid and gas components. Radial profiles from $x/d_n = 400$ to $x/d_n = 800$	80
4.11	Bi-variate histograms normalised as a <i>pdf</i> from LDV and DTV, at $x/d_n = 800$ for: $u_x - u_y$, $u_x - d_{[30]}$ and $u_y - d_{[30]}$	82
4.12	Reynolds stresses against radial distance. DTV <i>Average</i> and <i>d-Average</i> radial profiles from $x/d_n = 400$ to $x/d_n = 800$	83
4.14	Reynolds stresses anisotropy factor ($\bar{R}_{22}/\bar{R}_{11}$) against radial distance. DTV radial profiles by droplets' class diameters from $x/d_n = 400$ to $x/d_n = 800$	84
4.13	Reynolds stresses against radial distance. DTV radial profiles by droplets' class diameters for $x/d_n = 400$ and $x/d_n = 800$	85
4.15	Reynolds stresses against radial distance. DTV and LDV radial profiles at $x/d_n = 800$	86
4.16	Stokes number at the jet centerline by droplets' class of diameters from $x/d_n = 400$ to $x/d_n = 800$	87
4.17	Schematic representation of the 3D mesh, including boundary conditions.	88
4.18	Turbulence models' benchmark compared to the Liquid LDV.	89
4.19	Liquid mass fraction \tilde{Y} field in a mid-plane ($z = 0$) cutout. Solution from $t = 0.1$ s to $t = 0.3$ s.	90
4.20	Comparison of the Reynolds stresses against radial distance as a function of the turbulence model at $x/d_n = 800$. Experimental LDV (liquid and gas) and DTV radial profiles are shown as a benchmark.	92
4.21	Epsilon equation budget against radial distance for two cases: (a) $R_{ij} - \epsilon$ with $C_{\epsilon 1} = 1.44$ (Standard value); (b) $R_{ij} - \epsilon$ with $C_{\epsilon 1} = 1.60$ (round-jet correction). Radial profiles at $x/d_n = 400$	94
4.22	Mean axial velocity against radial distance as a function of $C_{\epsilon 1}$ at $x/d_n = 400$. Experimental LDV (liquid and gas) and DTV radial profiles are shown as a benchmark.	94
4.23	Equivalent diameter of droplets population against radial distance. Radial profiles from simulations and DTV at $x/d_n = 400$	96

List of Figures

4.24 Turbulent mass transport equation contributions budget against radial distance. Axial and radial components at $x/d_n = 400$	96
4.25 Mean slip-velocity against radial distance as a function of Y_{mod} at $x/d_n = 600$. Experimental LDV slip-velocity shown as a benchmark.	97
4.26 Reynolds stresses equations budget against radial distance at $x/d_n = 400$ for the $R_{ij} - \epsilon_{ij} Y_{mod0}$ case. Experimental LDV (liquid and gas) radial profiles are shown as a benchmark.	99
4.27 Comparison of the mean axial velocity against radial distance as a function of Y_{mod} at $x/d_n = 400$. Experimental LDV (liquid and gas) and DTV radial profiles are shown as a benchmark.	101
4.28 Turbulence mass transport models' benchmark. (a) Axial velocity along the centerline; (b) Axial velocity half-width; (c) Liquid volume fraction along the centerline.	101

List of Tables

1	Quantités moyennées à partir des données expérimentales.	xiv
2	Partition de la population de gouttes par classe de diamètre.	xiv
1.1	Physical properties of a phase-incompressible two-phase flow in SI-Units.	7
1.2	Operating conditions of a phase-incompressible two-phase flow.	7
1.3	Summary of the criteria for the cylindrical liquid jet fragmentation regimes.	8
1.4	Experimental conditions used in the study performed by Stevenin [57].	9
1.5	Physical properties of the study-case in SI-units at normal conditions.	10
1.6	Dimensionless numbers for the study-case conditions.	10
2.1	Integration and interpolation methods used in the <i>OpenFOAM</i> solver.	33
2.2	Spatial discretization methods used in the <i>OpenFOAM</i> solver.	34
2.3	Boundary conditions expressed in <i>OpenFOAM</i> solver.	35
2.4	Number of decomposed regions in the scalability test.	40
2.5	Mesh configurations for the mesh solution convergence test.	41
3.1	LDV BSA set-up for liquid and gas phases analysis.	51
3.2	Convergence criteria for the LDV liquid points.	53
3.3	Convergence criteria for the LDV gas points.	54
3.4	Partition of droplets population by class of diameter.	63

Nomenclature

Greek alphabet

$\bar{\Sigma}$	Mean liquid/gas interface surface per unit volume	$[m^2 \cdot m^{-3}]$
$\tilde{\Omega}$	Mean liquid/gas interface surface per unit mass	$[m^2 \cdot kg]$
τ_{ij}	Viscous constraint tensor	$[kg \cdot m^{-1} \cdot s^{-2}]$
ϵ	Turbulent kinetic energy dissipation rate	$[m^2 \cdot s^{-3}]$
ρ	Density	$[kg \cdot m^{-3}]$
ν	Kinematic viscosity	$[m^2 \cdot s^{-1}]$
μ	Dynamic viscosity	$[kg \cdot m^{-1} \cdot s^{-1}]$
σ_{L-G}	Liquid-gas surface tension	$[N \cdot m^{-1}]$
δ_{ij}	Kronecker tensor	$[-]$

Latin alphabet

x, y, z	Cartesian axial distance	$[m]$
u_i	Velocity vector	$[m \cdot s^{-1}]$
R_{ij}	Reynolds stresses tensor	$[m^2 \cdot s^{-2}]$
F_i	Turbulent mass flux vector	$[m \cdot s^{-1}]$
k	Turbulent kinetic energy	$[m^2 \cdot s^{-2}]$
g	Gravity acceleration	$[m \cdot s^{-2}]$
p	Pressure	$[Pa]$
\tilde{Y}	Liquid mass fraction	$[-]$
\bar{Y}	Liquid volume fraction	$[-]$
d_n	Nozzle diameter	$[m]$

Nomenclature

L_n	Nozzle length	[m]
L_c	Liquid column breakup length	[m]
S	Spreading rate	[–]
A	Axial centerline velocity decay rate	[–]
$y_{0.5u}$	Axial velocity half-width	[m]
$d_{[30]}$	Volume equivalent sphere diameter	[m]
$d_{[32]}$	Sauter mean diameter or SMD	[m]
Re	Reynolds number	[–]
We	Weber number	[–]
Oh	Ohnesorge number	[–]
St	Stokes number	[–]
C	Contrast ratio	[–]
l	Relative grey intensity level	[–]
w	Contour curve	

Subscripts and superscripts

i	Cartesian vector component, $i = \{1, 2, 3\}$ or $i = \{x, y, z\}$
ij	Cartesian tensor component, $i, j = \{1, 2, 3\}$
L	Refers to the liquid phase
G	Refers to the gas phase
s	Refers to the liquid-gas slip
J	Refers to the nozzle injection point
0	Refers to the jet's centerline
t	Turbulent quantity
(k)	Refers to the droplet class k

Symbols and operators

—	Reynolds average
~	Favre average

'	Reynolds turbulent fluctuation
"	Favre turbulent fluctuation
⟨ ⟩	Generic ensemble average

Abbreviations

<i>RANS</i>	Reynolds Averaged Navier-Stokes Equations
<i>RSM</i>	Reynolds Stress Model
<i>LDV</i>	Laser Doppler Velocimetry
<i>DTV</i>	Droplet Tracking Velocimetry
<i>OP</i>	Optical Probe
<i>SNR</i>	Signal-to-Noise Ratio
<i>BP</i>	Band-Pass Filter
<i>tbp</i>	Time between pulses

Introduction

This doctoral thesis is a product of the joint collaboration between the *Institut de Recherche sur les Phénomènes Hors Equilibre* (IRPHE) and the *Institut National de Recherche en Sciences et Technologies pour l'Environnement et l'Agriculture* (IRSTEA). All activities are carried out at IRSTEA Montpellier Centre, under the particular research topics at the UMR ITAP (Unité Mixte de Recherche Information – Technologies – Analyse environnementale – Procédés agricoles) and UMR G-Eau (Unité Mixte de Recherche Gestion de l'Eau, Acteurs, Usages). This doctoral thesis is partially financed by a fellowship from the Chilean government *CONICYT Becas Chile*.

The study subject of this thesis is the atomization of liquids in agricultural applications. Although this is not explicitly treated in this work, there are two main research topics accounted. From one side, on the use of pesticides sprayers for crop protection: to minimise problems due to the transport of polluting agents from the treated crops to air, water and ground. And in another side, on the optimisation of water usage for irrigation: to improve the efficiency of sprinklers that simulate the natural irrigation made by rain, limiting losses and heterogeneity.

Both study subjects are not treated from any specific application point-of-view. Instead, a generic case is created to investigate the atomization and dispersion of a liquid jet, which may share some elements with the original subjects, like the type of fluid and operating regimes (geometry, flow-rate and pressure). These similarities and the justification for the construction of this study case are presented in Chapter 1, where a simplified water round nozzle is conceived. In particular, the importance of conducting experimental and numerical approaches at the same time.

A choice is made on the type of flow modelling and numerical simulations. This is addressed in Chapter 2, where the specific approach of a mixture RANS turbulence modelling is used. The numerical method to solve the flow equations is also detailed, where a custom solver is built using the *OpenFOAM* CFD code. Although the experimental observations are introduced later, the construction of the numerical simulation cases is made in accordance with the experimental results.

The experimental campaign is presented in Chapter 3. Two main optical non-intrusive techniques are used to measure in both liquid and gas phases. The objective is to estimate the velocity field and droplet's sizes. LDV measurements are carried out first, where the main

Introduction

challenge is to capture separately the liquid from the gas acquisitions. To measure the droplet sizes and velocities, a custom DTV algorithm is constructed and applied to shadow images of droplets in the dispersed region of the jet. Using the data from the two experimental measurement techniques, the mean and fluctuating velocity fields are estimated, along with the droplet's sizes distribution.

The comparison between the results from the experimental and numerical approaches is presented in Chapter 4. Several parameters like the axial velocity decay-rate and the spreading rate of the jet are compared with numerical model cases. A focus is made on the reconstruction of the Reynolds stresses by class of droplet sizes and role of the mean liquid-gas slip-velocity as a source of anisotropy seen by the particular turbulence modelling.

A final set of conclusions are given in Chapter 4.2.4, along with some perspectives on some specific subjects that are not treated in this work, and that may be useful to improve the analysis for such atomization study.

1 General context

Introduction

The general framework on which this study is conducted is presented in this chapter. From the general use of atomisers in agricultural application to the underlying physics within. Since this doctoral thesis is focused on experimental and numerical techniques, applied to the atomization of liquid jets, the focus is on the review of such applications.

The general context is placed on the importance of the understanding of the fine behaviour of technological applications such as sprinklers for irrigation and pesticides sprayers for crop protection. Upon this, it focuses on the great effort that current experimental and numerical simulation techniques are being developed and used to better understand the atomization of liquids in agricultural applications.

From the atomization point-of-view, a state of the art is presented from a larger application spectrum. For example, because of the sensible and more precision needed in its applications, the atomization of liquids is a large topic of research in combustion. The access to cutting-edge experimental techniques and numerical simulations makes a literature review on such research subjects an interesting starting point.

The scope of this chapter is then to investigate how these other applications are related to the technological ones in agricultural sprayers and what type of applied research could be used.

1.1 State of the art

1.1.1 Atomization in agriculture

A typical system used in irrigation and/or pesticides aspersion consists in a liquid-jet flow projected into the air. Upon this projection, the liquid flow splits into droplets which will ultimately reach the target soil or leaves. The process by which this fragmentation occurs is called atomization.

The behaviour of the flow depends on several operational and environmental conditions, such as: geometry, flow rate, turbulence, liquid rheology and wind velocity, all of which have an impact on the droplets' sizes, distribution and velocity. It is important then to understand the physical mechanisms by which the liquid atomization and droplets' drift occur to better conceive and/or improve the technological applications in agriculture.

Throughout many years, the research development in liquid atomization for sprayers in agriculture has been conducted from a phenomenological approach, based on a large set of experiments that lead to empirical relations for some specific application. For example, Al Heidary et al. [1] review shows some of these experimental approaches and Salcedo et al. [52] some numerical simulations in an attempt to give a description of the flow. From these types of studies, it can be concluded that to perform this kind of research methodology in every possible case can be very expensive, both in time and resources.

Compared to other domains, like fuel-injectors for combustion or bubbly-flow in boilers, the atomization problem in agricultural sprayers is a rather large problem. It can go from the smallest scales of turbulence ($\sim 10^{-6} m$), passing through injector nozzle sizes of $\sim 10^{-3} m$, then to several meters of average range ($\sim 10^0 m$) and up to even kilo-meters ($\sim 10^3 m$) in the case of small droplets' drift into the atmosphere. It is extremely difficult then to study the whole problem; simplifications, sub-models, empirical relations, data integration, etc. have to be made to tackle the final problem.

From the point of view of irrigation and pesticides application, several detailed studies have been performed at IRSTEA (Institut National de Recherche en Sciences et Technologies pour l'Environnement et l'Agriculture). Currently, the irrigation part is overseen at the *UMR G-Eau* and the use of pesticides at the *UMR ITAP*, both at IRSTEA Montpellier Centre and in collaboration with IRPHE (Institut de Recherche sur les Phénomènes Hors Equilibre).

In irrigation, Kadem et al. [36] studies a large water cannon using a commercial CFD software (computational fluid dynamics), comparing the data with experiments using an optical probe (OP). There, a simplified two-phase mixture model, based on the original RANS (Reynolds Averaged Navier-Stokes) model proposed by Vallet et al. [60], is used to solve numerically the turbulent flow. The OP is used to obtain the estimated droplet's sizes and velocities, along with the liquid volume fraction. Although many simplifications and assumptions are used, the numerical results showed a relatively good agreement with the experimental data, but always

using a good set of model parameters.

In a following study, De Luca et al. [12] attempts to use the same numerical and experimental techniques, but this time applied to a hollow-cone swirl-chamber injector nozzle for pesticides. The complex flow generated by this type of injector produces another layer of complexity. From a numerical simulation point-of-view, it generates a strongly three-dimensional (3D) flow, making the numerical solver more time-consuming and boundary conditions difficult to estimate. Experiments are also more challenging, since an increase of spatial resolution and precision is needed to obtain accurate results. Nevertheless, again, using an appropriate turbulence model and parameters, good agreement between numerical and experimental results is found.

To tackle the questions issued from the later study, Belhadeff et al. [5] attempts to perform a more detailed set of experimental data, along with a similar numerical approach implemented into a commercial CFD software (ANSYS Fluent). Digging deeper into the turbulence RANS model, and having a set of PDA (Phase Doppler Anemometer) experimental data to compare, it appears that a simple description of the turbulent mass transport can not always provide good results. Indeed, once again the numerical results are considered in good agreement to the experimental observations only when a specific set of model parameters are specified.

The latest study performed at IRSTEA on the same subject is carried out by Stevenin [57]. In a similar way, the objective is to apply the same RANS turbulence model, back to an irrigation sprinkler this time (Figure 1.1), along with experimental data using an OP and DTV (Droplet Tracking Velocimetry) by shadow images.



(a) Commercial sprinkler Rain Bird RB46. (b) Field irrigation using a RB46 array.

Figure 1.1 – Sprinkler for irrigation purposes (Source: www.rainbird.fr).

The more detailed velocity field issued from the DTV data gives some insights on the turbulent multiphase flow of the problem. It is now possible to compare the Reynolds stresses from the DTV with the turbulent kinetic energy from the turbulent RANS model.

One interesting result is the anisotropy factor between the principal Reynolds stresses in this case, shown in Figure 1.2. Compared to a turbulent mono-phase round-jet, where the anisotropy factor takes a value close to $\bar{R}_{22}/\bar{R}_{11} \approx 0.6$, the case studied by Stevenin et al. [58] shows a value of $\bar{R}_{22}/\bar{R}_{11} \approx 0.05$ in the liquid phase, in the dispersed zone of the jet ($x/d_n > 500$);

where \bar{R}_{11} is the axial component of the Reynolds stresses and \bar{R}_{22} the lateral (radial) one.

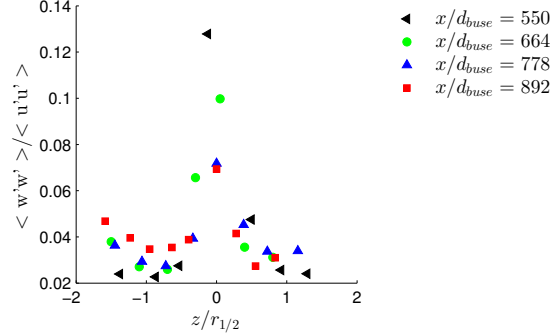


Figure 1.2 – Reynolds stresses anisotropy factor $\bar{R}_{22}/\bar{R}_{11}$ ($\overline{w'w'}/\overline{u'u'}$) from the DTV measurements performed by Stevenin [57].

This result raises questions about the $k - \epsilon$ RANS turbulent model used, and moreover, the assumptions of a boundary-layer like flow might neglect some key aspects about the source of this anisotropy.

Indeed, as pointed out in a more recent study by El-Asrag and Braun [18], the use of a RSM (Reynolds Stress Model) over a $k - \epsilon$ model type could improve the prediction of the Reynolds stresses in zones where the anisotropy is large.

It is then one of the main motivation of this study to find the source of this anisotropy by investigating why and how it is generated in this type of flow. To achieve this goal, a similar study case is considered in the present work, where numerical and experimental approaches are used.

1.1.2 Liquid jet's fragmentation

The atomization of a liquid jet occurs when a liquid-phase flow is injected into a gas-phase medium. This two-phase flow is considered non-miscible, meaning that the two phases do not form a mixture fluid and there are forces that keep a distinguishable interface between them. By the action of external forces on this interface, the liquid-phase breaks into packets or droplets, causing the actual atomization into the gas phase.

The forces present in this process of atomization vary depending on the fluid's properties and operating conditions. If there is only one liquid phase and one gas phase present, no phase-change occurs and there are no compressibility effects, the relevant physical properties are summarised in Table 1.1.

Table 1.1 – Physical properties of a phase-incompressible two-phase flow in SI-Units.

ρ_L	Liquid density	(kg/m^3)
ρ_G	Gas density	(kg/m^3)
ν_L	Liquid kinematic viscosity	(m^2/s)
ν_G	Gas kinematic viscosity	(m^2/s)
σ_{L-G}	Liquid-Gas surface tension	(N/m)

For the operating conditions, in the case of a liquid injected through a nozzle, only the average bulk velocities of both phases are considered. These are detailed in Table 1.2.

Table 1.2 – Operating conditions of a phase-incompressible two-phase flow.

$\bar{u}_{L,J}$	Liquid phase average bulk velocity	(m/s) .
$\bar{u}_{G,J}$	Gas phase average bulk velocity	(m/s) .

Where $\bar{u}_{G,J}$ is the injection velocity of a coaxial gas flow. Having these basic physical properties and operating conditions, three main dimensionless quantities can be constructed as a function of the forces that intervene in the atomization process:

- Reynolds number: Ratio of inertial forces to viscous forces within a fluid subject movement. Defined at the exit of a nozzle of diameter d_n :

$$Re = \frac{(\bar{u}_L - \bar{u}_G)d_n}{\nu_L}. \quad (1.1)$$

- Weber number: Ratio of inertial forces to surface tension. Can be defined for the liquid:

$$We_L = \frac{\rho_L(\bar{u}_L - \bar{u}_G)^2 d_n}{\sigma_{L-G}}, \quad (1.2)$$

and for the gas:

$$We_G = \frac{\rho_G(\bar{u}_L - \bar{u}_G)^2 d_n}{\sigma_{L-G}}. \quad (1.3)$$

- Ohnesorge number: Relate the viscous forces to inertial and surface tension:

$$Oh = \frac{\rho_L \nu_L}{\sqrt{\rho_L \sigma_{L-G} d_n}}. \quad (1.4)$$

In an extensive review, Dumouchel [16] presents many experimental works on the primary atomization of liquids. Based on these dimensionless numbers, several classifications can be made as a function of: fluids properties, geometry, laminar or turbulent regimes, gas assisted or injected into still gases. In the case of liquid jets for agricultural applications, there is a

high probability to find turbulent liquid round jets. Therefore, the analysis of the atomization regime is centred on this type of liquid fragmentation.

Having a fixed geometry and working fluid, the average bulk velocity \bar{u}_L is the only parameter that could set the working regime of a round jet. As detailed by Dumouchel [16], a first classification can be made based on the observation of the liquid core breakup length L_c as a function of \bar{u}_L . This is shown in Figure 1.3.

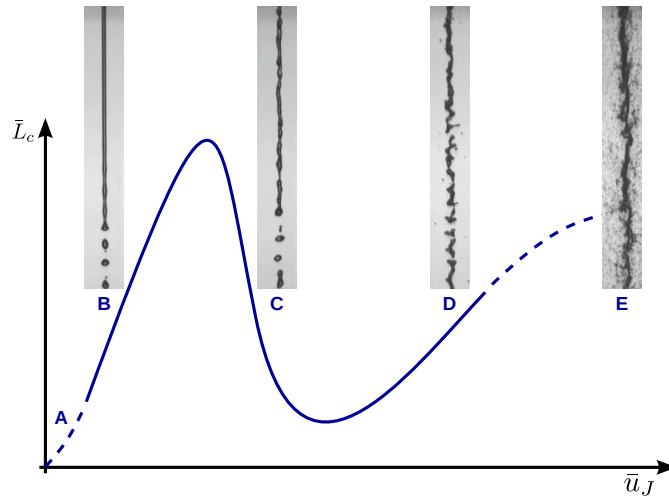


Figure 1.3 – Round jet behaviour, stability curve of the breakup length L_c as a function of the average liquid velocity at the nozzle \bar{u}_J . Region A: Dripping regime. Region B: Rayleigh regime. Region C: First wind-induced regime. Region D: Second wind-induced regime. Region E: Atomization regime. (from Dumouchel [16])

Then, as a function of the Weber and Ohnesorge numbers, several authors described a detailed separation between the regions as detailed in the Table 1.3.

Table 1.3 – Summary of the criteria for the cylindrical liquid jet fragmentation regimes.

Region A: Dripping regime	$We_L < 8$
Region B: Rayleigh regime	$We_L > 8$
	$We_G < 0.4$ or
	$We_G < 1.2 + 3.41Oh^{0.9}$
Region C: First wind-induced regime	$1.2 + 3.41Oh^{0.9} < We_G < 13$
Region D: Second wind-induced regime	$13 < We_G < 40.3$
Region E: Atomization regime	$40.3 < We_G$

As described by Dumouchel [16], the characteristics of large jets ($d_n > 1\text{ mm}$) is the presence of peeling droplets from the nozzle exit, this is called the primary breakup.

Primary breakup is important because it determines the initial properties of the dispersed

liquid phase and has an effect on the behaviour of the later secondary breakup mechanism. Wu et al. [64] showed that spray properties are strongly determined by the turbulence conditions at the nozzle exit and differ from the results with laminar nozzle conditions. Moreover, the length of the liquid jet core is also affected by the turbulence inside the injector.

As an example, the main case studied by Stevenin et al. [59] [58] corresponds to a turbulent high-Weber liquid round jet, whose conditions are summarised on Table 1.4.

Table 1.4 – Experimental conditions used in the study performed by Stevenin [57].

Nozzle diameter	d_n	4.37 mm
Injection bulk velocity	\bar{u}_L	22 m/s
Density ratio	ρ_L/ρ_G	840
Reynolds number	Re	97000
Weber number	We_L	29000
Ohnesorge number	Oh	0.0018

This would place the case in the *Region D* of the diagram. Moreover, based on the review by Sallam et al. [53], the liquid breakup length L_c should follow the following empirical relation:

$$\frac{\bar{L}_c}{d_n} = 8.51 We_L^{0.32}, \quad (1.5)$$

corresponding to a turbulent breakup regime, yielding an estimated average breakup length of $\bar{L}_c/d_n = 228$. In this regime, breakup is due to the turbulent fluctuations, already present in the liquid core, leaving the aerodynamic effects to a secondary role.

To study a similar case, whatever the type of round nozzle used, it should operate under the following considerations:

1. It should be a large circular jet, where $d_n > 1 \text{ mm}$. In a turbulent regime, there should be a distinguishable boundary layer inside the nozzle, this generates the peeling droplets at the surface right after the injection.
2. The combination of physical properties of the fluids, along with the geometrical and operating conditions, should place the atomization regime into the *second wind-induced regime*.

This motivates the construction of a specific study case that is carried out throughout this whole study. Both numerical simulations and experimental techniques are applied to this study subject, these are detailed later in Chapter 2 and Chapter 3 respectively.

1.2 Study case

As reported by Stevenin [57], the main difficulty for obtaining accurate experimental results using a DTV and LDV set-up is the spatial precision of the measurement points. When working with a large liquid jet, the resulting liquid range could be up to several meters, making an experimental campaign difficult to accomplish.

In an effort to try to reproduce a similar case under a more controlled experimental environment, a downsized case is considered. In particular, to investigate the Reynolds stresses anisotropy as shown before, the downsized study case should be placed in the same atomization regime. Considering this, the following parameters for this study case are selected:

1. **Injector:** A circular nozzle of $d_n = 1.2 \text{ mm}$ is used. To avoid any extra difficulty on the estimation of the boundary layer inside the nozzle, the roughness of the interior walls is considered negligible. With this, a borosilicate glass is chosen for the material. In the same way as Wu et al. [64], Sallam et al. [53] and others mentioned in Dumouchel [16] review on round jets, the nozzle length is chosen in order to obtain a fully developed turbulent pipe flow, in this case $L_n/d_n = 50$.
2. **Fluids properties:** A liquid water jet is injected into still air. From this, Table 1.5 shows the physical properties taken at *normal conditions* (297 K, 1 atm).

Table 1.5 – Physical properties of the study-case in SI-units at normal conditions.

ρ_L	Water density	998.3	kg/m^3
ρ_G	Air density	1.205	kg/m^3
ν_L	Water kinematic viscosity	1.004×10^{-6}	m^2/s
ν_G	Air kinematic viscosity	15.11×10^{-6}	m^2/s
σ_{L-G}	Water-Air surface tension	0.073	N/m

3. **Injection velocity:** An injection average bulk velocity of $\bar{u}_J = 35 \text{ m/s}$ is selected. Along with the physical properties mentioned before, it yields the dimensionless numbers detailed in Table 1.6.

Table 1.6 – Dimensionless numbers for the study-case conditions.

Reynolds number	Re	41 833
Weber number	We_L	20 158
	We_G	24.3
Ohnesorge number	Oh	0.0034

4. **Gravity effects:** To avoid any asymmetry, the injection velocity is aligned with gravity, pointing downwards.

All these fluids properties and operating conditions ensure that the turbulence inside the nozzle should be fully developed upon any upstream boundary conditions. Then, the nozzle diameter is sufficiently large to have a direct influence on the boundary layer thickness inside the nozzle on the primary atomization. And finally, the experiment should operate inside the second wind-induced atomization regime.

With the intent to emulate a real case, and although this type of nozzle does not exist in any agricultural application, a simplified case like this should provide a more controlled environment for any experimental and/or numerical simulation.

Summary

The general framework of this study is presented in this chapter. More specifically, the use of sprinklers in agriculture, like water jets for irrigation or some specific nozzles for pesticides spraying. From this point-of-view, the following points could summarise this chapter:

- The study of sprinklers in agriculture leads to the study of the atomization process of liquids. Like in other applications, the flow is almost always turbulent, meaning that the analysis is centred on the fragmentation of the liquid under turbulent conditions.
- The understanding of this multiphase flow is tackled by experiments and numerical simulations. The turbulent nature of the flow induces a large spectrum of scales of motion, making both experimental and numerical studies hard to accomplish.
- A short literature review reveals the advantage of the use of a simplified study case. This case is finally a water round jet injected into still air. The cylindrical nozzle diameter is $d_n = 1.2 \text{ mm}$, with a length of $L_n/d_n = 50$. The injection average bulk velocity is $\bar{u}_J = 35 \text{ m/s}$, placing the atomization process in a turbulent second-wind induced regime.
- Similar to previous experimental and numerical studies conducted at IRSTEA Montpellier Centre, LDV and DTV experimental techniques are used to capture the velocity fields of both liquid and gas phases in the flow. Whereas from the numerical simulation part, due to the large spatial dimension size of the problem, an Eulerian mixture RANS turbulence approach is used to simulate the flow.

2 Numerical modelling

Introduction

This chapter is dedicated to the numerical modelling of a generic multiphase flow encountered in a typical liquid jet atomization problem. An Eulerian approach is considered along with a mixture-fluid variable-density formulation for the liquid/gas mixture. The chapter is divided in four main sections: Multiphase flow modelling, Turbulence modelling, Numerical solver and study cases definition.

In Section 2.1 a detailed description of the mixture multiphase formulation is presented. The transformation from the instantaneous field equations, and their corresponding variables, to the average mixture problem is achieved using the Favre-average operator. This operator transforms the set of equations into a variable-density U-RANS (Unsteady Reynolds-averaged Navier-Stokes) problem.

Based on this formulation, the description of the two main RANS turbulence models used in this study are presented in Section 2.2: $\tilde{k} - \tilde{\epsilon}$ and $\tilde{R}_{ij} - \tilde{\epsilon}$. Then, several variations for the turbulent mass flux modelling are presented, along with an Eulerian description of the interface between the two phases.

The numerical method to solve the U-RANS system of equations is then presented in Section 2.3. Details of the implementation of a custom solver using the *OpenFOAM C++* library are provided. The main focus is on the strong coupling between the turbulent mass flux and the pressure-based solver in the momentum equation, which differs from a solver for incompressible constant density fluids.

Finally, several study cases are developed using a combination of the presented models in this chapter. Starting from the geometric 3D construction of the cases, mesh generation, convergence analysis and specific definition of every case analysed later in Chapter 4 are detailed. These cases are constructed based on an incremental analysis on the complexity of the turbulence and other transport models.

2.1 Multiphase flow modelling

2.1.1 Eulerian formulation

For the Eulerian formulation, it is assumed that the fluid is a continuum and the forces applied to an infinitesimal volume of fluid can be described by field equations. From the starting point of this case, one main assumption is taken into account: the liquid atomization problem occurs at high Reynolds and Weber numbers. This means that the forces at the interface between phases are small compared to inertial forces. This approach yields five main equations for the instantaneous problem in 3D-Cartesian coordinates (x_i with $i = 1, 2, 3$):

1. Mass conservation (1 equation):

$$\frac{\partial \rho}{\partial t} + \frac{\partial \rho u_i}{\partial x_i} = 0; \quad (2.1)$$

2. Momentum conservation (3 equations, 1 for each component):

$$\frac{\partial \rho u_i}{\partial t} + \frac{\partial \rho u_i u_j}{\partial x_j} = -\frac{\partial p}{\partial x_i} + \rho g_i + \frac{\partial \tau_{ij}}{\partial x_j}; \quad (2.2)$$

3. Phase transport (1 equation):

$$\frac{\partial \rho Y}{\partial t} + \frac{\partial \rho u_i Y}{\partial x_i} = 0; \quad (2.3)$$

where every variable is an instantaneous field depending on the absolute position and time (x_i, t), which in SI units are:

- u_i : Velocity field, (m/s).
- p : Pressure field, (Pa).
- g_i : Gravity field, (m/s^2).
- τ_{ij} : Viscous constraint, ($kg/m \cdot s$).
- Y : Liquid phase indicator, takes the value of 1 when in the liquid and 0 otherwise, (-).
- ρ : Fluid density, takes the value of ρ_L (liquid density) when in the liquid and ρ_G (gas density) otherwise, (kg/m^3).

The fluid velocity u_i is then composed of discontinuous liquid $u_{i,L}$ and gas $u_{i,G}$ velocity fields at a given position and time. Therefore it is the liquid phase indicator Y which sets the current state:

$$u_i = Y u_{i,L} + (1 - Y) u_{i,G}. \quad (2.4)$$

The laminar viscous constraint τ_{ij} is modelled using a simple Stokes hypothesis for Newtonian fluids:

$$\tau_{ij} = \mu \left(\frac{\partial u_i}{\partial x_j} + \frac{\partial u_j}{\partial x_i} - \frac{2}{3} \frac{\partial u_k}{\partial x_k} \delta_{ij} \right), \quad (2.5)$$

where the dynamic viscosity μ is defined as a discontinuous quantity too, so it takes the value of μ_l in the liquid and otherwise μ_g for the gas as a function of Y :

$$\mu = Y\mu_L + (1 - Y)\mu_G. \quad (2.6)$$

It is important to notice that in this mixture Eulerian formulation for the mixture-fluid there is no special treatment at the liquid/gas interface, as there are no separate momentum equations for each phase and the fluid is considered as a miscible binary-mixture. This approach is also called Quasi-Multiphase Eulerian (QME) in more recent developments [40] [3].

2.1.2 Multiphase average model

Because of the size and the different scales of motion in this liquid atomization problem, a step further in the modelling involves the averaging of equations (2.1), (2.2) and (2.3); following the same procedure as in a single-phase variable density fluid [8].

Under this approach a mass-weighted average is used: the *Favre Average*. It is understood that the averaging process is an ensemble average over n-identical repetitions, where for any instantaneous variable h the operator and the subsequent mean \tilde{h} and fluctuating h'' parts are:

$$\tilde{h} = \frac{\overline{\rho h}}{\bar{\rho}}; \quad h = \tilde{h} + h''; \quad (2.7)$$

where $\bar{\rho}$ is the mixture density. For a relatively low injection velocity and constant temperature, $\bar{\rho}$ is only a function of the mixture of ρ_L and ρ_G :

$$\bar{\rho} = \bar{Y}\rho_L + (1 - \bar{Y})\rho_G. \quad (2.8)$$

The mean volume fraction \bar{Y} can be expressed also as a function of the mean mass fraction \tilde{Y} , making the formulation closer to a variable density scalar mass concentration equivalence:

$$\tilde{Y} = \frac{\rho_L \bar{Y}}{\bar{\rho}}. \quad (2.9)$$

A graphical representation of this process is shown in Figure 2.1, where the Favre-average is applied to the liquid phase indicator Y and density ρ , transforming them into \tilde{Y} and $\bar{\rho}$ respectively.



Figure 2.1 – Favre average operation over the liquid phase indicator Y and the fluid density ρ .

The same procedure can be made to the other variables and the equations (2.1), (2.2) and (2.3), yielding the desired mixture RANS formulation, which is presented next.

2.1.3 Mixture RANS equations

The mixture RANS model equations are obtained by applying the Favre-average operator to the previous set of equations and by expressing the variables as a fluctuation centred on the ensemble average. Using this procedure, the set of equations to solve are very similar to the previous ones:

1. Mass conservation (1 equation):

$$\frac{\partial \bar{\rho}}{\partial t} + \frac{\partial \bar{\rho} \tilde{u}_i}{\partial x_i} = 0; \quad (2.10)$$

2. Momentum conservation (3 equations, 1 for each component):

$$\frac{\partial \bar{\rho} \tilde{u}_i}{\partial t} + \frac{\partial \bar{\rho} \tilde{u}_i \tilde{u}_j}{\partial x_j} = -\frac{\partial \bar{p}}{\partial x_i} + \bar{\rho} g_i + \frac{\partial \tilde{\tau}_{ij}}{\partial x_j} - \frac{\partial \bar{\rho} \widetilde{u_i'' u_j''}}{\partial x_j}; \quad (2.11)$$

3. Turbulent mass transport (1 equation):

$$\frac{\partial \bar{\rho} \tilde{Y}}{\partial t} + \frac{\partial \bar{\rho} \tilde{u}_i \tilde{Y}}{\partial x_i} = -\frac{\partial \bar{\rho} \widetilde{u_i'' Y''}}{\partial x_i}; \quad (2.12)$$

where $\widetilde{u_i'' u_j''}$ is the Favre-averaged Reynolds stress tensor and $\widetilde{u_i'' Y''}$ the turbulent mass flux. Both are new unknowns in the equation and closure models are needed to solve them. The Favre-averaged laminar viscous constraint $\tilde{\tau}_{ij}$ is deduced from Eq. (2.5):

$$\tilde{\tau}_{ij} = \bar{\mu} \left(\frac{\partial \tilde{u}_i}{\partial x_j} + \frac{\partial \tilde{u}_j}{\partial x_i} - \frac{2}{3} \frac{\partial \tilde{u}_k}{\partial x_k} \delta_{ij} \right). \quad (2.13)$$

However, the mixture dynamic viscosity represented by $\bar{\mu}$ is defined using a linear contribution between the liquid dynamic viscosity μ_l and gas dynamic viscosity μ_g :

$$\bar{\mu} = \bar{Y}\mu_L + (1 - \bar{Y})\mu_G. \quad (2.14)$$

Many forms of this contribution can be found in the literature. For example, Sanjose [54] used Wilke [62] formulation to describe the mixture viscosity of evaporating fuels, this applies however only to a mixture of gas species. Despite the inaccuracy of Eq. 2.14, given the high Reynolds number as a starting hypothesis for this atomization problem, this term is expected to be orders of magnitude smaller than the Reynolds stresses contribution, making this possible error negligible.

Two extra expressions arise from this type of averaging. The first one is that the turbulent mass flux can be expressed from the liquid-gas slip-velocity $\bar{u}_{i,S}$, starting from Eq. (2.4):

$$\bar{u}_{i,S} = \bar{u}_{i,L} - \bar{u}_{i,G} = \frac{\widetilde{u_i'' Y''}}{\widetilde{Y}(1 - \widetilde{Y})}; \quad (2.15)$$

where $\bar{u}_{i,L}$ and $\bar{u}_{i,G}$ are the Reynolds-averaged liquid and gas velocities. The second one is that the fluctuating part of the Favre-averaged velocity is not centred when a Reynolds average is applied; $\overline{u_i''} \neq 0$. Indeed, developing this from Eq. (2.7), it can also be expressed in terms of $\widetilde{u_i'' Y''}$:

$$\overline{u_i''} = - \left(\frac{1}{\rho_G} - \frac{1}{\rho_L} \right) \bar{\rho} \widetilde{u_i'' Y''}. \quad (2.16)$$

Along with momentum and mass conservation equations, and using the same hypothesis for high Reynolds and Weber numbers flows as Vallet et al. [60], the interface of the liquid/gas mixture is modelled using a transport equation for the quantity $\bar{\Sigma}$, the mean surface area of the liquid/gas interface per unit volume.

All variables to solve and quantities to model can be summarised in the following list:

- $\bar{\rho}$: Mixture average density (as a function of \bar{Y} or \widetilde{Y}), to solve.
- \bar{u}_i : Mixture average velocity field, to solve.
- \bar{p} : Average pressure field, to solve.
- $\bar{\tau}_{ij}$: Mixture average viscous constraint, to be modelled.
- $\widetilde{u_i'' u_j''}$: Mixture Reynolds stress tensor, to be modelled.
- $\widetilde{u_i'' Y''}$: Turbulent mass flux, to be modelled.
- $\bar{\Sigma}$: Mean surface area of the liquid/gas interface per unit volume, to be modelled. Also expressed as $\bar{\Sigma} = \bar{\rho} \widetilde{\Omega}$.

The purpose of the next sections of this chapter is to address the solving of this system of equations.

2.2 Turbulence modelling

The focus of this section is to present all the models implemented and tested into the custom numerical solver, for both the Reynolds stresses $\widetilde{u''_i u''_j}$ and turbulent mass fluxes $\widetilde{u''_i Y''}$.

2.2.1 Reynolds stresses

Many options exist for the closure of this quantity. However, only two main options are considered for this study:

1. First order closure: Two-equation variable density $\widetilde{k} - \widetilde{\epsilon}$ model (K-Epsilon).
2. Second order closure: Seven-equation variable density $\widetilde{R}_{ij} - \widetilde{\epsilon}$ model (RSM, Reynolds Stress Model).

In the first choice, the Reynolds stresses are coupled with the mean flow using an eddy-viscosity concept. The form of this eddy-viscosity is then constructed using two transport equations, both dependent on flow characteristics. The other option is to prescribe transport equations for each component of the Reynolds stresses and other quantities, also dependent of the flow characteristics.

First order closure: K-Epsilon

Using an eddy-viscosity model under variable density formulation, a direct transposition from the Reynolds-averaged Boussinesq hypothesis case is used. Although many variations and non-linear versions exist for this closure (some can be found fully detailed in Chassaing et al. [8]), only the simplest linear version is kept.

$$-\bar{\rho} \widetilde{u''_i u''_j} + \frac{2}{3} \bar{\rho} \widetilde{k} \delta_{ij} = \mu_t \left(\frac{\partial \widetilde{u}_i}{\partial x_j} + \frac{\partial \widetilde{u}_j}{\partial x_i} - \frac{2}{3} \frac{\partial \widetilde{u}_k}{\partial x_k} \delta_{ij} \right). \quad (2.17)$$

Compared to the expression for constant-density incompressible flows, this variable density version reads that the deviatoric part of $\widetilde{u''_i u''_j}$ is proportional to the deviatoric part of the rate-of-strain tensor $\widetilde{S}_{ij} = \frac{1}{2} \left(\frac{\partial \widetilde{u}_i}{\partial x_j} + \frac{\partial \widetilde{u}_j}{\partial x_i} \right)$, via the eddy-viscosity μ_t , which takes the following form using a $\widetilde{k} - \widetilde{\epsilon}$ formulation:

$$\mu_t = C_\mu \bar{\rho} \frac{\widetilde{k}^2}{\widetilde{\epsilon}}; \quad (2.18)$$

where \tilde{k} is the turbulent kinetic energy, $\tilde{\epsilon}$ the turbulent kinetic energy dissipation rate and C_μ a proportional constant. Henceforth, this first order closure centres its efforts into finding proper transport equations for those quantities.

The exact transport equation for the Favre-averaged turbulent kinetic energy is derived from the momentum equation Eq. (2.7). The instantaneous values are expressed from the average and fluctuating parts, then the equation is multiplied by u_i'' and averaged, finally the corresponding summation is applied making $\tilde{k} = \frac{1}{2} \overline{u_i'' u_i''}$. Different versions arises for this procedure depending on the regrouped parts and their physical explanation [8]. The version kept is the closest to the later modelled version:

$$\underbrace{\frac{\partial \tilde{\rho} \tilde{k}}{\partial t} + \frac{\partial \tilde{\rho} \tilde{k} \tilde{u}_i}{\partial x_i}}_{(a)} = - \underbrace{\frac{\partial}{\partial x_j} \left[\frac{1}{2} \overline{\tilde{\rho} u_i'' u_i'' u_j''} + \overline{p' u_j''} - \tau_{ij} u_i'' \right]}_{(b)} \underbrace{- \overline{\tilde{\rho} u_i'' u_j''} \frac{\partial \tilde{u}_i}{\partial x_j}}_{(c)} - \underbrace{\tau_{ij} \frac{\partial u_i''}{\partial x_j}}_{(d)} \quad (2.19)$$

$$\underbrace{- \overline{u_i''} \frac{\partial \tilde{p}}{\partial x_i}}_{(e)} + \underbrace{p' \frac{\partial u_i''}{\partial x_i}}_{(f)}$$

where all the terms in the first row are ones commonly found in constant-density incompressible flows, leaving the second row exclusively to Favre-averaged variable-density flows:

- (a) Material transport in conservative form.
- (b) Diffusion, split in three parts. The first two are the turbulent diffusion, including pressure effects. The last one correspond to the molecular diffusion. In jet flows, these two contributions are modelled together using a single gradient diffusion hypothesis:

$$\frac{\partial}{\partial x_j} \left(\frac{1}{2} \overline{\tilde{\rho} u_i'' u_i'' u_j''} + \overline{p' u_j''} + \tau_{ij} u_i'' \right) = - \frac{\partial}{\partial x_j} \left[\left(\tilde{\mu} + \frac{\mu_t}{\sigma_k} \right) \frac{\partial \tilde{k}}{\partial x_j} \right]; \text{ with } \sigma_k = 1.0. \quad (2.20)$$

- (c) Turbulent kinetic energy production (P_k) by mean shear, with $\overline{u_i'' u_j''}$ from Eq. (2.17).
- (d) Turbulent kinetic energy dissipation rate (E_k), modelled as $\tilde{\rho} \tilde{\epsilon}$.
- (e) Energy transfer by coupling the turbulent mass flux with the mean pressure gradient, also known as the mean pressure work (Σ_k).
- (f) Pressure-dilatation correlation. It appears when the velocity fluctuation is non-solenoidal. However, it is not included in the modelled equation.

Consequently, the modelled Favre-averaged variable density \tilde{k} -equation, based on the original formulation proposed by Jones and Launder [34], is:

$$\frac{\partial \tilde{\rho} \tilde{k}}{\partial t} + \frac{\partial \tilde{\rho} \tilde{u}_i \tilde{k}}{\partial x_i} = \frac{\partial}{\partial x_j} \left[\left(\tilde{\mu} + \frac{\mu_t}{\sigma_k} \right) \frac{\partial \tilde{k}}{\partial x_j} \right] - \overline{\tilde{\rho} u_i'' u_j''} \frac{\partial \tilde{u}_i}{\partial x_j} - \tilde{\rho} \tilde{\epsilon} - \overline{u_i''} \frac{\partial \tilde{p}}{\partial x_i}. \quad (2.21)$$

Chapter 2. Numerical modelling

For the turbulent kinetic energy dissipation rate $\tilde{\epsilon}$, a different approach is taken. First, only the solenoidal part is taken into account, so $\tilde{\epsilon} \sim \overline{\tilde{\epsilon}}$. And second, the modelled equation is not derived from the exact transport equation for $\tau_{ij} \frac{\partial u_i''}{\partial x_j}$. Instead, an approach is taken in the same way as Jones and Launder [34] by making the modelled equation homogeneous to the k-equation counterpart.

Although many options for this modelled equation exist in the literature (an extensive review can be found in Chassaing et al. [8] and Schiestel [56] for variable density flows), the version kept is the simplest one and analog to Eq. (2.21):

$$\begin{aligned} \frac{\partial \bar{\rho} \tilde{\epsilon}}{\partial t} + \frac{\partial \bar{\rho} \tilde{\epsilon} \tilde{u}_i}{\partial x_i} &= \frac{\partial}{\partial x_i} \left[\left(\bar{\mu} + \frac{\mu_t}{\sigma_\epsilon} \right) \frac{\partial \tilde{\epsilon}}{\partial x_i} \right] - C_{\epsilon 1} \frac{\bar{\epsilon}}{\bar{k}} \overline{\bar{\rho} u_i'' u_j''} \frac{\partial \tilde{u}_i}{\partial x_j} - C_{\epsilon 2} \bar{\rho} \frac{\bar{\epsilon}^2}{\bar{k}} \\ &+ C_{\epsilon 3} \frac{\bar{\epsilon}}{\bar{k}} \overline{p' \frac{\partial u_k''}{\partial x_k}} - C_{\epsilon 4} \frac{\bar{\epsilon}}{\bar{k}} \overline{u_i'' \frac{\partial \bar{p}}{\partial x_i}} - C_{\epsilon 5} \bar{\rho} \tilde{\epsilon} \frac{\partial \tilde{u}_k}{\partial x_k}; \end{aligned} \quad (2.22)$$

where in the RHS there are in the first row: Diffusion, production, destruction; and in the second row: the counterparts from Eq. (2.21) of pressure-dilatation and mean pressure work; being the last one exclusive to compressible flow, related to the turbulence length scale when passing through a shock-wave.

The standard values for the model constants are $C_{\epsilon 1} = 1.44$ and $C_{\epsilon 2} = 1.92$. The pressure-dilatation correlation is not modelled, so $C_{\epsilon 3} = 0$. The mean pressure work contribution counterpart uses $C_{\epsilon 4} = 1.0$. And for the last term, $C_{\epsilon 5} = 1/3$ in isotropic turbulence and $C_{\epsilon 5} = 1.0$ otherwise (see Chassaing et al. [8, pp. 301-302]). All these parameters are set in specific study-cases.

Second order closure: RSM

The same strategy as in the previous $\tilde{k} - \tilde{\epsilon}$ model is used to define the equations modelled for the Reynolds stresses. The six equations of the symmetric tensor are extracted from the exact transport equation for $\overline{u_i'' u_j''}$, whereas the dissipation counterpart is purely modelled.

The base formulation from Launder, Reece, and Rodi [39] is used. As our model aims to simulate also the flow inside the nozzle, wall-reflexion terms were also included (see Gibson and Launder [23]). In a similar way to Eq. (2.21), variable density effects were added to the modelled equation (see Chassaing et al. [8, pp. 312-324]).

The exact transport equation for $\overline{u_i'' u_j''}$, using a specific rearrangement of terms is the following:

$$\frac{\partial \bar{\rho} \overline{u_i'' u_j''}}{\partial t} + \frac{\partial \bar{\rho} \tilde{u}_l \overline{u_i'' u_j''}}{\partial x_l} = \bar{\rho} P_{ij} - \frac{\partial T_{lij}}{\partial x_l} + \bar{\rho} \Phi_{ij} + \Sigma_{ij} - \bar{\epsilon}_{ij}. \quad (2.23)$$

In the same way as in the k-equation, some terms need modelled relations to get a complete

closed form equation. A basic linear approach is taken for the construction of these terms, following the original RSM model from Launder, Reece, and Rodi [39]:

- P_{ij} , turbulent production. Already in its final form:

$$P_{ij} = - \left(\overline{u_i'' u_k''} \frac{\partial \tilde{u}_j}{\partial x_k} + \overline{u_j'' u_k''} \frac{\partial \tilde{u}_i}{\partial x_k} \right); \quad (2.24)$$

- Σ_{ij} , Mass flux coupling:

$$\Sigma_{ij} = \overline{u_i''} \left(\frac{\partial \bar{\tau}_{jl}}{\partial x_l} - \frac{\partial \bar{p}}{\partial x_j} \right) + \overline{u_j''} \left(\frac{\partial \bar{\tau}_{il}}{\partial x_l} - \frac{\partial \bar{p}}{\partial x_i} \right); \quad (2.25)$$

where only viscous effects are neglected for the modelled part:

$$\Sigma_{ij} = - \overline{u_i''} \frac{\partial \bar{p}}{\partial x_j} - \overline{u_j''} \frac{\partial \bar{p}}{\partial x_i}; \quad (2.26)$$

- Φ_{ij} , deviatoric pressure-strain correlation:

$$\Phi_{ij} = \frac{1}{\bar{\rho}} \left[\overline{p' \left(\frac{\partial u_i''}{\partial x_j} + \frac{\partial u_j''}{\partial x_i} \right)} \right]; \quad (2.27)$$

modelled as two contributions, the *slow* return-to-isotropy Rotta model and the *rapid* isotropization of production [47]:

$$\Phi_{ij} = \phi_{ij}^{(slow)} + \phi_{ij}^{(rapid)}; \quad (2.28)$$

where:

$$\phi_{ij}^{(slow)} = -C_1 \frac{\bar{\epsilon}}{\bar{k}} \left(\overline{u_i'' u_j''} - \frac{2}{3} \bar{k} \delta_{ij} \right); \quad (2.29)$$

and:

$$\phi_{ij}^{(rapid)} = -C_2 \left(P_{ij} - \frac{1}{3} P_{ll} \delta_{ij} \right) - C_3 \frac{1}{\bar{\rho}} \left(\Sigma_{ij} - \frac{1}{3} \Sigma_{ll} \delta_{ij} \right); \quad (2.30)$$

where for $\phi_{ij}^{(slow)}$, $C_1 = 1.8$, for $\phi_{ij}^{(rapid)}$, $C_2 = 0.6$ and $C_3 = 0.75$, from Vallet et al. [60].

- T_{lij} , transport:

$$T_{lij} = \overline{\bar{\rho} u_i'' \tilde{u}_j u_l''} + \overline{p' u_i''} \delta_{jl} + \overline{p' u_j''} \delta_{il} - \left(\overline{\tau'_{jl} u_i''} + \overline{\tau'_{il} u_j''} \right); \quad (2.31)$$

modelled as a whole turbulent diffusion term using the same Reynolds-stress tensor to

define an anisotropic diffusion coefficient [47] and the viscous part is neglected:

$$T_{lij} = -C_s \bar{\rho} \frac{\tilde{k}}{\bar{\epsilon}} \overline{u_l'' u_k''} \frac{\partial \overline{u_i'' u_j''}}{\partial x_k}; \quad (2.32)$$

where $C_s = 0.22$.

- $\bar{\epsilon}_{ij}$, turbulent dissipation rate tensor:

$$\bar{\epsilon}_{ij} = \left(\overline{\tau'_{jl} \frac{\partial u_i''}{\partial x_l}} + \overline{\tau'_{il} \frac{\partial u_j''}{\partial x_l}} \right). \quad (2.33)$$

The modelled version reads:

$$\bar{\epsilon}_{ij} = \bar{\rho} \bar{\epsilon}_{ij} \equiv \bar{\rho} \left(\bar{\mathbf{e}}_{ij} + \frac{2}{3} \bar{\epsilon} \delta_{ij} \right); \quad (2.34)$$

where $\bar{\epsilon} = \bar{\epsilon}_{ii}/2$ is the turbulent kinetic energy dissipation rate and $\bar{\mathbf{e}}_{ij}$ is the deviatoric part of $\bar{\epsilon}_{ij}$. Two options are considered. The first one is to neglect the deviatoric part making $\bar{\epsilon}_{ij}$ to act only in the principal components of $\overline{u_i'' u_j''}$:

$$\bar{\epsilon}_{ij} = \frac{2}{3} \bar{\rho} \bar{\epsilon} \delta_{ij}. \quad (2.35)$$

The second option is to include some anisotropy as proposed by Rotta [50], but making the dissipation tensor active in all the components:

$$\bar{\epsilon}_{ij} = \bar{\rho} \frac{\overline{u_i'' u_j''}}{\tilde{k}} \bar{\epsilon} \quad (2.36)$$

This basic model is closer to DNS data in a near-wall boundary layer, but still considered inaccurate [32]. However, this version is kept and no further analysis is made related to this type of modelling.

For the kinetic energy dissipation rate $\tilde{\epsilon}$, the same transport equation from the $\tilde{k} - \tilde{\epsilon}$ model is taken. The only main difference is that instead of evaluating the production term using the Boussinesq relation Eq. (2.17), the explicit Reynolds stresses from Eq. (2.23) are used.

2.2.2 Turbulent mass-flux

Along with the Reynolds stresses, the other main quantity to model is the turbulent mass flux $\overline{u_i'' Y''}$ from Eq. (2.12). Given the strong density difference between the liquid/gas, any effect on the mixture density $\bar{\rho}$ variation makes the turbulent mass flux strongly coupled with the whole system of equations in the RANS formulation, and its effect is further transferred into higher moments via $\overline{u_i''} = -\left(\frac{1}{\rho_G} - \frac{1}{\rho_L}\right) \bar{\rho} \overline{u_i'' Y''}$, which is an important source term in the $\overline{u_i'' u_j''}$

transport Eq. (2.23).

To analyse the effect on the behaviour of several case scenarios, three $\widetilde{u_i'' Y''}$ closure models are considered:

- First order model (Mod-0): Basic expression following the gradient of \widetilde{Y} and coupled with turbulence via ν_t , based on Fick's law.
- First order model (Mod-1): Basic expression following the gradient of \widetilde{Y} but coupled with the actual Reynolds stresses to include some anisotropy in the behaviour of the gradient.
- Second order model (Mod-2): A specific transport equation is solved for every component of the vector $\widetilde{u_i'' Y''}$, where source terms are coupled with the main flow, turbulence and an explicit relation to drag forces induced by droplets.

First order model

This approach is similar to a passive scalar transport problem, where if there are no strong main flow gradients, the concentration of a certain quantity is diffused following a gradient Fick's law on itself. As the flow becomes turbulent, the diffusivity coefficient varies, following the scales of motion in the fluid, but the model is nearly the same.

Based on the original work proposed by Vallet et al. [60], a simplified expression for the turbulent mass flux was derived by Stevenin et al. [59] by neglecting the pressure gradient effects and by using a boundary layer approximation on the averaged flow. This approach ensures that the fluxes are deduced by applying several simplifications on a second-order model and are not issued as a departure guess:

$$-\bar{\rho} \widetilde{u_i'' Y''} = \frac{\mu_t}{\sigma_Y} \frac{\partial \widetilde{Y}}{\partial x_i}; \quad (2.37)$$

where σ_Y is the turbulent Schmidt number for the diffusivity that takes a value close to 1.0. However, as experimentally found [58] and assuming a strong anisotropy in a liquid round jet so that $\widetilde{u_2''^2} \approx 0.082 \widetilde{k}$ under the same boundary layer approximation, it yields a value of $\sigma_Y = 5.5$ for the lateral diffusion.

To account dynamically for the possible strong anisotropy in the Reynolds stresses, the complete approximation of the later expression is the following:

$$-\bar{\rho} \widetilde{u_i'' Y''} = C_Y \bar{\rho} \frac{\widetilde{k}}{\widetilde{\epsilon}} \widetilde{u_i'' u_j''} \frac{\partial \widetilde{Y}}{\partial x_j}. \quad (2.38)$$

Here, instead of the turbulent viscosity μ_t , a decomposition using the Reynolds stresses is used. In the case analysed by Belhadef et al. [5], $C_Y \approx 0.9$, but if the modelled anisotropy is weak and closer to a mono-phase round-jet, the desired reduction in the lateral diffusivity

component (i=2) might not be achieved simply by this type of modelling. Stevenin et al. [59] proposes a forced way to set this constant in the same way as in Eq. (2.37) model for σ_Y , where assuming an anisotropy factor $\widetilde{u_2''^2}/\widetilde{u_1''^2} = a_R$ such as $C_Y \approx a_R C_\mu / \sigma_Y$.

Other approaches have been used by other authors to account for this diffusivity variation. Demoulin et al. [14] tried to make σ_Y a function of $\bar{\rho}$, to account for the large density variations. Going even further, Desantes et al. [15] proposed a Realizable version of the variable Schmidt number, by bounding the fluxes with the turbulence fluctuations scales $\sqrt{\widetilde{u_i''^2}}$. Nevertheless, these approaches only change the diffusivity and do not include other effects from the main flow, which is the purpose of the second order modelling presented next.

Second order model

Although Vallet et al. [60] proposed a second order closure for the turbulent mass flux, this approach does not provide a direct coupling with the liquid/gas interface surface per unit volume $\bar{\rho}\widetilde{\Omega}$, where the destruction term is only proportional to the turbulence decay rate $\tau_t^{-1} = \tilde{\epsilon}/\tilde{k}$.

To tackle this deficiency, a slightly different approach is developed by Beau [4] and later another similar approach by Andreini et al. [3], who constructed a general framework for the coupling of $\bar{\rho}\widetilde{\Omega}$ and \widetilde{Y} equations using RANS turbulence models.

The transport equation chosen is the version proposed by Beau [4]. The sink term in this case is a destruction term by drag forces, induced by the slip velocity between the gas phase and the droplets:

$$\begin{aligned} \frac{\partial \bar{\rho} \widetilde{u_i'' Y''}}{\partial t} + \frac{\partial \bar{\rho} \widetilde{u_j u_i'' Y''}}{\partial x_j} = \frac{\partial}{\partial x_j} \left(\frac{\mu_t}{\sigma_F} \frac{\partial \widetilde{u_i'' Y''}}{\partial x_j} \right) \\ - C_{F1} \bar{\rho} \widetilde{u_j Y''} \frac{\partial \widetilde{u_i}}{\partial x_j} - C_{F2} \bar{\rho} \widetilde{u_i'' u_j''} \frac{\partial \widetilde{Y}}{\partial x_j} - C_{F3} \overline{Y''} \frac{\partial \bar{p}}{\partial x_i} + C_{F4} \bar{F}_{Drag,i}; \end{aligned} \quad (2.39)$$

where C_{F1} , C_{F2} , C_{F3} and C_{F4} are constants, specified as 1.0, 1.0, 0.0 and 4.0 respectively by Beau [4], with $\sigma_F = 0.9$ as the turbulent Schmidt number in the diffusion term. The drag force is calculated using a Schiller-Naumann relation, as a function of the drag coefficient with the Reynolds number, and the velocity seen by the droplets:

$$\bar{F}_{Drag,i} = -18 \rho_G \nu_G \frac{\overline{Y}}{d_l^2} (\bar{u}_{i,L} - \bar{u}_{i,G} - \bar{u}_{i,D}) (1 + 0.15 Re_d^{0.687}); \quad (2.40)$$

where d_l is a characteristic length of a droplet population, where for this case the Sauter mean diameter d_{32} , calculated from the $\bar{\rho}\widetilde{\Omega}$ solution, is used. The Reynolds number associated with

this diameter is:

$$Re_d = \frac{\|\bar{u}_{i,L} - \bar{u}_{i,G} - \bar{u}_{i,D}\| d_l}{\nu_G}; \quad (2.41)$$

where $\bar{u}_{i,D}$ stands for the drift velocity. It is assumed to be the limit at which the velocity follows a first order model, so using Eq. (2.37) it becomes:

$$\bar{u}_{i,D} = \frac{1}{\tilde{Y}(1-\tilde{Y})} \frac{\nu_t}{\sigma_Y} \frac{\partial \tilde{Y}}{\partial x_i}; \quad (2.42)$$

where σ_Y is specified the same as in the first order model.

With these elements, the droplets relaxation time is defined as:

$$\tau_R = \frac{\rho_L d_l^2}{18\mu_G} (1 + 0.15 Re_d^{0.687})^{-1}. \quad (2.43)$$

Since the main objective is to construct a modelled case capable to adapt to a large spectrum of flow characteristics and geometries, it is expected that this formulation for the turbulent mass flux $\overline{u_i'' Y''}$, coupled with a RSM turbulence $\tilde{k} - \tilde{\epsilon}$ using a simple gradient law for the mass fluxes. However, as better discussed in the next section, the strong coupling of the whole system of equations is particularly challenging to the numerical solver and not all of the models described here could be used in a straightforward solution.

2.2.3 Eulerian interface

The last quantity to include in the model is the liquid/gas interface surface per unit volume, $\bar{\rho} \tilde{\Omega}$ or $\bar{\Sigma}$ (m^2/m^3). $\tilde{\Omega}$ is constructed so that $\tilde{\Omega} = \bar{\Sigma}/\bar{\rho}$, this is done simply to ensure that the transport equation can be written in a conservative form.

The model was first proposed by Vallet et al. [60] and it has been subjected to several modifications in the later years (Beau [4]; Lebas et al. [40]; Duret et al. [17]). It is important to notice that this type of formulation requires two main assumptions: a high Reynolds number, providing a strong enough turbulent mixture; and a high Weber number, so the surface tension between the liquid/gas does not play a significant role at the equilibrium to the described atomization problem.

Based on the latest advances in this formulation, the latest version proposed by Lebas et al. [40] is kept, with some considerations taken by Duret et al. [17] based on DNS calculations used to describe the behaviour of some parameters in the average model. The equation for $\tilde{\Omega}$

can be constructed in a conservative form, neglecting the evaporation part:

$$\frac{\partial \bar{\rho} \tilde{\Omega}}{\partial t} + \frac{\partial \bar{\rho} \tilde{\Omega} \tilde{u}_i}{\partial x_i} = \frac{\partial}{\partial x_i} \left(\frac{\mu_t}{\sigma_\Omega} \frac{\partial \tilde{\Omega}}{\partial x_i} \right) + \Phi (S_{init} + S_{turb}) + (1 - \Phi) (S_{coll} + S_{2ndBU}); \quad (2.44)$$

where:

- Φ is a logistic function ([0 1]) that changes the importance of the source terms from the dense part ($\bar{Y} > 0.5$) to the diluted part ($\bar{Y} < 0.1$).
- S_{init} is an initialisation term important only in the dense part close to the nozzle.
- S_{turb} is the production/destruction due to turbulence in the dense part of the spray.
- S_{coll} is the collision/coalescence source term for the dilute part of the spray.
- S_{2ndBU} is the secondary break-up source term (exclusively) for the dilute part of the spray.

Because of the lack of information on the construction of such parameters applied to this study case, only the S_{turb} term is included inside the model. Then a simplified version of the equation reads:

$$\frac{\partial \bar{\rho} \tilde{\Omega}}{\partial t} + \frac{\partial \bar{\rho} \tilde{\Omega} \tilde{u}_i}{\partial x_i} = \frac{\partial}{\partial x_i} \left(\frac{\mu_t}{\sigma_\Omega} \frac{\partial \tilde{\Omega}}{\partial x_i} \right) + \alpha \frac{\bar{\rho} \tilde{\Omega}}{\tau_t} \left(1 - \frac{\tilde{\Omega}}{\tilde{\Omega}^*} \right); \quad (2.45)$$

where $\tau_t = \tilde{k}/\tilde{\epsilon}$ and $\tilde{\Omega}^*$ is the equilibrium value at the smallest scales using an equilibrium Weber number $We^* = 1.0$:

$$\tilde{\Omega}^* = 4 \frac{0.5(\rho_L + \rho_G) \bar{Y}(1 - \bar{Y}) \tilde{k}}{\sigma_{L-G} \bar{\rho} We^*}. \quad (2.46)$$

The parameters of the model are set by default, meaning $\alpha = 1.0$ and $\sigma_\Omega = 1.0$.

In the same way that in the original work made by Vallet et al. [60], $\tilde{\Omega}$ is linked to the Sauter-Mean-Diameter $d_{[32]}$ by the following relation:

$$d_{[32]} = \frac{\rho_L \bar{Y}}{\bar{\rho} \tilde{\Omega}}. \quad (2.47)$$

2.3 Numerical model

The problem described in the previous section forms a non-linear system of differential equations. One method to solve them is to cut each equation into small pieces and find a numerical solution that approaches the real one under some assumptions. Providing a compatible set of initial and boundary conditions, a finite volume method (FVM) is used to solve the system obtaining an approximated solution for every variable.

Many available CFD tools offer the capability to find a numerical solution to this type of problem, ranging from laminar flows to different turbulent and multiphase-turbulent models. Commonly used commercial solutions offer the possibility to include custom expression to modelled equations, using user-defined-functions (UDF). However, this approach is always limited because modifications to the solver core are usually not allowed, making difficult to solve the actual system of equations and simplifications have to be made to overcome this situation [5] [38] [37].

In this problem, the system of equations to solve is formed mainly by Eq. (2.10), Eq. (2.11) and Eq. (2.12). Given the heavy coupling between all the variables, and the intention to solve it as-is, a custom solver is required to properly model each interaction under a known and controlled numerical environment.

All the efforts are then redirected to create a custom solver using an open source CFD tool. For this task, the *OpenFOAM*® code is chosen. It can handle 3D arbitrary meshes for FVM, common solvers for the momentum equation are already coded, it includes many discretization schemes and mainly because it is supported by a large community working in the same field. The description of this custom solver is the main subject of this section.

2.3.1 OpenFOAM solver

The *OpenFOAM*® C++ code was developed by Weller et al. [61] as a free, open-source software for CFD calculations. Currently it is owned and maintained by the OpenFOAM Foundation¹ and distributed exclusively under the General Public Licence (GPL).

Using the equivalent of a *module* from a commercial CFD software, *OpenFOAM*® is separated into specific *solvers*, each one focused on different physical problems but always sharing a common library of tools, all following an object-oriented programming in C++.

Instead of building a study-case using a specific *module*, the approach here is a little different. Using a *solver* from a near-like physics as a baseline, modifications are introduced to it to meet the specific requirements for the desired physical problem, creating a compiled custom solver. Applied to this particular problem, one of the main goals of this custom solver is to find a solution for the coupled system of Eq. (2.10) and Eq. (2.11). To see how this is done in OpenFOAM, an example on how equations are written and treated in the C++ code stream is shown using a laminar case for a single-phase fluid:

$$\frac{\partial \rho U}{\partial t} + \nabla \cdot \phi U - \nabla \cdot \mu \nabla U = -\nabla p. \quad (2.48)$$

This is the momentum conservation equation, where U is the velocity field, ϕ the mass flux (simply ρU), μ the dynamic viscosity and p the pressure field. If this pressure field is known and some initial and boundary conditions are provided, this differential equation can easily

¹The OpenFOAM Foundation: www.openfoam.org

be solved using a raw piece of code represented in Figure 2.2:

```
1 solve(  
2     fvm::ddt(rho, U)  
3     + fvm::div(phi, U)  
4     - fvm::laplacian(mu, U)  
5     ==  
6     - fvc::grad(p)  
7 );
```

Figure 2.2 – OpenFOAM C++ code to solve the momentum conservation equation.

Related to Eq. (2.48), highlighted in blue are the differential operators, in grey there are two options, depending if one would like to solve for a variable inside the operator (*fvm*) or simply to express the result explicitly (*fvc*). In this case, the variable to solve is the velocity field U , so *ddt*, *div* and *laplacian* require implicit discretization schemes for U .

Custom solver strategy

More specific to the multiphase problem treated here, a general strategy to solve the system of equations could be the following:

1. Solve turbulence mass flux $\widetilde{u}_i'' Y''$ and \widetilde{Y} .
2. Solve \widetilde{u}_i and \widetilde{p} .
3. Solve turbulence model $\widetilde{u}_i'' \widetilde{u}_j''$.
4. Solve other variables ($\widetilde{\Sigma}$).

Contrary to the previous single-phase example, the pressure field is generally an unknown, making the item (2) of the list hard to solve.

Many specific methods exist to solve this system of equations, one of them is the PISO algorithm (Pressure Implicit with Splitting of Operator) developed by Issa [31], which is generally well suited for unsteady problems using the smallest amount of computational resources. However, the convergence of this method under heavy compressible or variable density flows may not be always assured, for those cases, the SIMPLE (Semi-Implicit Method for Pressure-Linked Equations) algorithm (Patankar and Spalding [44]) can be used, which uses under-relaxation factors for both pressure and velocity to stabilise the solution. To account for this, an hybrid mixing of both algorithms is implemented into OpenFOAM and is detailed next.

The PIMPLE algorithm implemented in OpenFOAM has been developed by Jasak [33] to solve the transient momentum equation in conservative form. A brief description on how the

algorithm works is presented here only to describe one of the main modifications to account for the variable-density mixture multiphase formulation of this problem.

This study-case is considered to be an incompressible problem. A relatively low injection velocity and pressure-drop inside the injector do not produce compressibility effects, nor cavitation or phase changes. If both phases stay the same, it is considered to be a phase-incompressible flow.

A classic PISO solver for solving the transient Navier-Stokes equations for incompressible flows uses a velocity divergence-free condition to impose mass conservation on each time-step. However, as the velocity field is actually a mixture velocity \tilde{u} , in variable density this condition does not meet and $\nabla \cdot \tilde{u} \neq 0$. Actually, developing Eq. (2.10) gives:

$$\nabla \cdot \tilde{u} = -\frac{1}{\bar{\rho}} \frac{D\bar{\rho}}{Dt}. \quad (2.49)$$

The PISO algorithm is modified to take into account this effect, where the construction of the Poisson equation for the pressure solver (detailed next) is derived from the mass conservation in its complete form, yielding an additional explicit source term in the *RHS*.

The final correction steps on this modified PISO algorithm work the same as in the original form, where convergence is checked by mass conservation and pressure solution residuals.

Custom PISO loop

A fully discretized version of momentum equation Eq. (2.11), after all numerical schemes have been chosen, can be expressed in the following form:

$$a_P U_P^{(n+1)} = H(U^{(n)}) - \nabla p^{(n+1)} \quad (2.50)$$

where $U_P^{(n+1)}$ and $p^{(n+1)}$ are the velocity and pressure fields to solve for, advancing from the solution in $t = t_{(n)}$ to $t = t_{(n)} + \Delta t = t_{(n+1)}$. The discretization method yields a matrix-arranged variables in every cell centre P . The method separates every part of the equation that multiplies the diagonal elements of the matrix as a_P and everything else but the pressure in $H(U^{(n)})$. These operators are both function of the velocity field too, but in the linearization process they are left behind using the last know solution at $t = t_{(n)}$. For example, if the Reynolds stresses $\overline{u_i'' u_j''}$ are included explicitly into the momentum equation, then they are inside the $H(U^{(n)})$ operator, as a function of the previous $U_P^{(n)}$ solution.

Using this decomposition, it is easy to find the solution for the next time-step $t = t_{n+1}$, simply dividing by a_P :

$$U_P^{(n+1)} = \frac{H(U^{(n)})}{a_P} - \frac{\nabla p^{(n+1)}}{a_P}. \quad (2.51)$$

Chapter 2. Numerical modelling

If the pressure $p^{(n)}$ is used, then the solution is an approximation that would require a correction, called the momentum predictor. However, an implicit solution for $t = t_{(n+1)}$ is still preferred, making the pressure $p^{(n+1)}$ still an unknown.

To get both at the same time, the velocity solution $U_p^{(n+1)}$ is then injected into the mass conservation equation to isolate the pressure. To do so, first the cell centred values are interpolated to cell faces f , creating a flux:

$$\left(U_p^{(n+1)}\right)_f = \left(\frac{H(U^{(n)})}{a_p}\right)_f - \left(\frac{\nabla p^{(n+1)}}{a_p}\right)_f. \quad (2.52)$$

Then, the divergence operator ($\nabla \cdot$) is applied to Eq. (2.52), forming the mass conservation Eq. (2.10). A typical incompressible solver would use $\nabla \cdot U_f^{(n+1)} = 0$ as a short form, which is shown to be not true in variable density flows. Indeed, expanding Eq. (2.10):

$$\frac{\partial \tilde{u}_i}{\partial x_i} = -\frac{1}{\bar{\rho}} \frac{D\bar{\rho}}{Dt} \approx -\frac{1}{\bar{\rho}} \frac{\partial \bar{\rho}}{\partial \tilde{Y}} \frac{D\tilde{Y}}{Dt} \equiv \left(\frac{1}{\rho_G} - \frac{1}{\rho_L}\right) \frac{\partial}{\partial x_i} \left(\bar{\rho} \widetilde{u_i'' Y''}\right) = -\frac{\partial \overline{u_i''}}{\partial x_i}. \quad (2.53)$$

This imposes the extra constraint to solve the equation, as the divergence of the velocity field must match the RHS of this expression:

$$\nabla \cdot \left(U_p^{(n+1)}\right)_f = -\frac{1}{\bar{\rho}} \frac{D\bar{\rho}}{Dt}; \quad (2.54)$$

which yields a Poisson equation for the pressure $p^{(n+1)}$:

$$\nabla \cdot \left(\frac{H(U)}{a_p}\right)_f = \nabla \cdot \left(\frac{\nabla p}{a_p}\right)_f + \frac{1}{\bar{\rho}} \frac{D\bar{\rho}}{Dt}. \quad (2.55)$$

The solution of this equation is very time-consuming, taking nearly 80% of the computational time. Moreover, when using an arbitrary non-orthogonal mesh, several correction steps must be applied because the pressure gradient is expressed normal to cell faces. This procedure is done by solving Eq. (2.55) and then re-calculating the corrected gradient each time.

Then, the solution for $U^{(n+1)}$, with $p^{(n+1)}$ known this time, is updated by going back to Eq. (2.51):

$$U_p^{(n+1)} = U_p^* - \frac{\nabla p^{(n+1)}}{a_p}; \quad (2.56)$$

where U_p^* is simply $\frac{H(U^{(n)})}{a_p}$, updated using the last known solution for $U^{(n)}$. Finally, if the residual of $p^{(n+1)}$ is small enough not to produce further changes to the calculated $U^{(n+1)}$, the solution has converged.

This original approach should be considered as a simplification of a real compressible solver. For instance, in the compressible case studied by Payri et al. [45], the pressure equation is

parabolic and the simplification made in Eq. (2.53) does not apply.

Solver global loop

The PISO loop explained before can be repeated several times to achieve convergence inside the same time-step. However, this provides only a converged solution for \tilde{u}_i and \bar{p} fields, leaving all other variables behind. To tackle this, the PISO loop is placed inside a global SIMPLE loop as shown in Figure 2.3, where everything is solved for each time-step Δt .

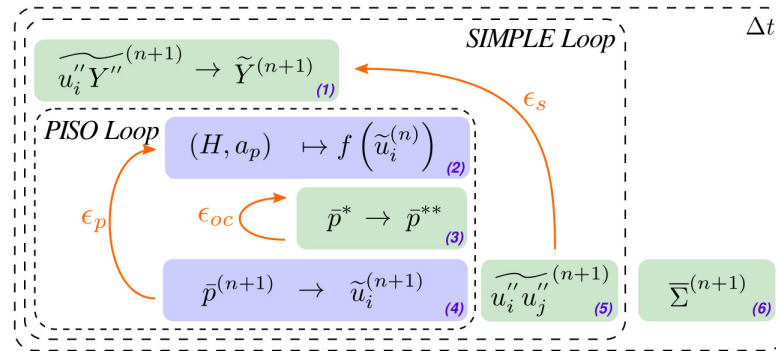


Figure 2.3 – Solution control for the customised solver implemented in OpenFOAM for each time-step Δt .

The global loop is solved in the following order for each Δt :

1. SIMPLE Loop in, solve turbulence mass flux $\widetilde{u_i'' Y''}$ and \tilde{Y} : (1). If an extra variable is needed, the last known converged solution is used (usually from the previous time-step) as an initial guess.
2. PISO Loop, solve \tilde{u}_i and \bar{p} : (2), (3) and (4). Where ϵ_{oc} is the pressure residual for the orthogonal correction and ϵ_p for the whole PISO loop. This is important because H and a_p are updated using the new velocity field each time.
3. Solve turbulence model $\widetilde{u_i'' u_j''}$: (5). The turbulence model is solved using converged velocity and pressure fields. Turbulence equations include non-negligible explicit source terms in the *RHS*, to preserve diagonal-dominance in the iterative solver, turbulence equations are under-relaxed by a factor of $\alpha = 0.5$.
4. SIMPLE Loop: Go back to (1) using the calculated solution until the residual ϵ_s for the pressure field is small enough. No under-relaxation for the pressure or velocity fields is needed this time.
5. Solve other variables ($\bar{\Sigma}$): (6). Then go to the next time-step.

As detailed in the analysis on Chapter 4, for a typical study case using 10^{-8} as a converged residual, the SIMPLE loop takes 2-3 steps for each time-step, then the PISO loop takes 2 steps

for each SIMPLE loop and the OC (Orthogonal Correction) takes 2 for each PISO step. It is then easy to see why the pressure equation takes most of the time inside the global solver. It is also this part of the solver which reaches convergence last.

2.3.2 Numerical schemes

Numerical schemes are used to have a linearised and discretized version of every equation in the system. Momentum conservation Eq. (2.11) is shown to take the form of Eq. (2.50) assuming that a numerical scheme is used. Then, using simple algebraic matrix operations, a solution can be found. It is then important to describe how this process is done and why some selected schemes are chosen to run the case analysis.

The Partial Differential Equation (PDE) system is expressed as derivative operators over variables both in space and time. In OpenFOAM, every transport equation for a scalar ϕ can be expressed as follows:

$$\underbrace{\frac{\partial \rho \phi}{\partial t}}_{(a)} + \underbrace{\nabla \cdot (\rho U \phi)}_{(b)} - \underbrace{\nabla \cdot (\rho \Gamma_\phi \nabla \phi)}_{(c)} = \underbrace{S_\phi(\phi)}_{(d)}; \quad (2.57)$$

where the terms under brackets are:

- (a): Time derivative.
- (b): Convection.
- (c): Laplacian/Diffusion.
- (d): Linearised source.

The Finite Volume Method (FVM) is based on the integral form of this expression, where Eq. (2.57) is also satisfied:

$$\begin{aligned} & \int_t^{t+\Delta t} \left[\frac{\partial}{\partial t} \int_{V_P} \rho \phi dV + \int_{V_P} \nabla \cdot (\rho U \phi) dV - \int_{V_P} \nabla \cdot (\rho \Gamma_\phi \nabla \phi) dV \right] dt \\ & = \int_t^{t+\Delta t} \left[\int_{V_P} S_\phi(\phi) dV \right] dt. \end{aligned} \quad (2.58)$$

Every term needs a discretization form, first in space and then in time. For this, Figure 2.4 shows the geometric parameters assuming an arbitrary mesh decomposition of a domain in small volumes, where the interaction of two adjacent volumes of centroids P and N is represented. V_P and V_N are the volumes of two adjacent elements, d is the distance between the centroids, f is the name designation of the face separating the volumes and S_f the surface area vector normal to this face, pointing outwards if the face is considered to be owned by P as in this case.

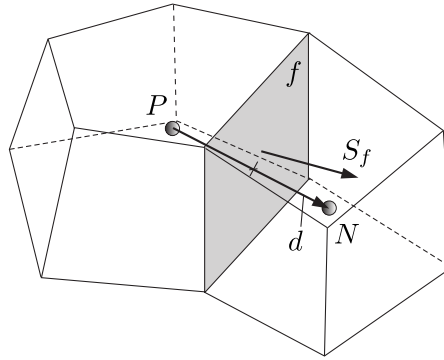


Figure 2.4 – Parameters in finite volume discretization (from the OpenFOAM®Programmer’s Guide 2.4.0).

Each term in Eq. (2.58) is then transformed using the interactions from the geometry presented in Figure 2.4. The details on how this is achieved can be found in any book of numerical methods for fluid dynamics (eg. [22]) or in the OpenFOAM documentation [26] [25].

As an example, the *Laplacian/Diffusion* term in Eq. (2.57) is expressed as follows:

$$\int_V \nabla \cdot (\Gamma_\phi \nabla \phi) dV = \int_S dS \cdot (\Gamma_\phi \nabla \phi) = \sum_f \Gamma_{\phi f} S_f \cdot (\nabla \phi)_f \tag{2.59}$$

Then, if the mesh is orthogonal and using the parameters defined in Figure 2.4, an implicit scheme would read:

$$S_f \cdot (\nabla \phi)_f = \|S_f\| \frac{\phi_N - \phi_P}{\|d\|}, \tag{2.60}$$

where an algebraic solution for the value of ϕ_N can be obtained.

It is important to notice that in this case the diffusivity parameter is linearised (it can also be a function of ϕ) and interpolated to cell faces. Then, to have an accurate and robust discretization scheme, an adequate interpolation method must be used and several passages to solve the equation might be needed to re-calculate these linearised terms.

First, to get all the expressions in an integral form, in volume and in time, the methods detailed in Table 2.1 are used.

Table 2.1 – Integration and interpolation methods used in the *OpenFOAM* solver.

Type	Method	
Temporal In- tegration	Euler	Implicit/Explicit depending on the discretization scheme.
Volume Inte- gration	Gauss	Gauss’s theorem of the volume integral for gradi- ents.
Interpolation	Linear	Used to pass from cell centres to cell faces.

Chapter 2. Numerical modelling

Then, for each type of element in this case study the corresponding spatial discretization scheme is detailed in Table 2.2.

Table 2.2 – Spatial discretization methods used in the *OpenFOAM* solver.

Type	Method	
Temporal Derivative	Euler	Implicit for all temporal derivatives. 1st order accurate in time.
Convection	Upwind	Used in every model as a first approximation. Bounded, 1st order accurate in space.
	Limited vanLeer	Used in the mass fraction transport. Bounded, 2nd order accurate in space.
	Limited Linear	Used for the rest. Bounded/unbounded, 1st/2nd order accurate in space.
Laplacian	Linear Limited	Corrected part not greater than 0.5 of the orthogonal part.
Source	Linear Implicit	When the variable is involved.
	Linear Explicit	When it is a pure source term.

2.3.3 Mesh and convergence

Mesh construction

The mesh is constructed using the *blockMesh* utility bundled with OpenFOAM. It creates an unstructured mesh of hexahedral-type elements transformed from rectangular volumes. A schematic view of the principal geometric parameters for the mesh construction along with the boundary conditions is shown in Figure 2.5.

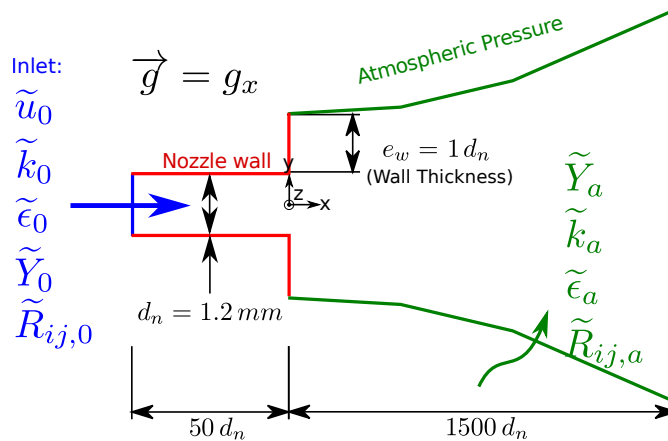


Figure 2.5 – Schematic representation of the mesh, including boundary conditions.

The Dirichlet-Neumann boundary conditions are specified in the three types of boundary:

Inlet (blue), Nozzle wall (red) and Atmospheric (green). These are detailed for all the variables using the OpenFOAM representation in Table 2.3.

Table 2.3 – Boundary conditions expressed in *OpenFOAM* solver.

Boundary	Variable	OpenFOAM Type
Inlet	\tilde{u}_0 : Velocity	<i>fixedValue</i>
	\tilde{k}_0 : Turbulent kinetic energy	<i>fixedValue</i>
	$\tilde{\epsilon}_0$: Turbulent dissipation rate	<i>fixedValue</i>
	\bar{Y}_0 : Liquid volume fraction	<i>fixedValue</i>
	$\tilde{R}_{ij,0}$: Reynolds stresses	<i>fixedValue</i>
	\bar{p}_0 : Pressure	<i>zeroGradient</i>
Wall	\tilde{u}_w : Velocity	<i>fixedValue</i>
	\tilde{k}_w : Turbulent kinetic energy	<i>kqRWallFunction</i>
	$\tilde{\epsilon}_w$: Turbulent dissipation rate	<i>epsilonWallFunction</i>
	\bar{Y}_w : Liquid volume fraction	<i>zeroGradient</i>
	$\tilde{R}_{ij,w}$: Reynolds stresses	<i>kqRWallFunction</i>
	\bar{p}_w : Pressure	<i>zeroGradient</i>
Atmospheric	\tilde{u}_a : Velocity	<i>pressureInletOutletVelocity</i>
	\tilde{k}_a : Turbulent kinetic energy	<i>inletOutlet</i>
	$\tilde{\epsilon}_a$: Turbulent dissipation rate	<i>inletOutlet</i>
	\bar{Y}_a : Liquid volume fraction	<i>inletOutlet</i>
	$\tilde{R}_{ij,a}$: Reynolds stresses	<i>inletOutlet</i>
	\bar{p}_a : Pressure	<i>totalPressure</i>

The velocity and the pressure work together to switch the boundary condition at the atmosphere limit depending on the flow's direction. As a function of this effect, in case of entrainment, all other boundary conditions also change from *zeroGradient* to an *Inlet* value that must be specified. For example, when the flow is entering at the atmospheric condition, the velocity is calculated using the total pressure and as the surrounding air does not have water in it, the inflow boundary condition for the liquid volume fraction should be $\bar{Y}_a = 0$.

If these boundary conditions are not well specified, following the behaviour of the near cells inside the main volume, an undesired solution might be found. As the Poisson equation for the pressure is elliptic, the pressure solution will strongly depend on these Dirichlet-Neumann boundary conditions. As a general rule for this case, the atmosphere boundary condition is placed far from the solution, so that no large gradients of any quantity are significant and the entrainment produced by the pressure drop happens at a very low velocity.

The volume size for the mesh might vary however depending on the study case. For instance, if a low diffusion case is tested, a narrow domain is constructed. The resulting mesh is then refined using a first approximated solution, where $\|\nabla \bar{Y}\|$ (volume fraction gradient magnitude) and $\sqrt{S^2}$ (strain tensor magnitude) are calculated to locate the zone which requires refinement.

The resulting 3D mesh for a real case can have up to 6 000 000 elements, a view of this is shown in Figure 2.6.

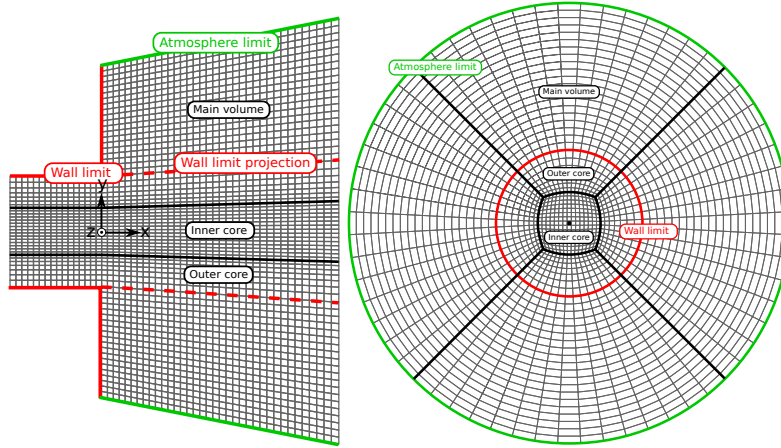


Figure 2.6 – Meshing strategy for a 3D case: Longitudinal slice (left) and transverse slice(right) near the injector nozzle.

A closer view of the Figure 2.5 (left) shows the detailed mesh construction geometry, where the nozzle wall is represented in red and the atmospheric boundary in green, matching those in the previous schematic view in Figure 2.5.

The nozzle itself is constructed by 5 square-prismatic blocks: an inner core, surrounded by 4 outer-core extensions to form a perfect circle inside the nozzle. These two volumes are then projected into the main mesh volume outside the nozzle, adding an extra layer of $1.0d_n$. The whole mesh is then translated using an expansion ratio of $0.15 m/m$, so that the same proportions shown in Figure 2.5 (right) are respected up to $1500d_n$. These final volume makes an atmospheric boundary far enough from the solution, keeping the mesh refinement close to the zone with the strongest gradients.

Despite that the geometry is consistent and that it can be translated into perfect prismatic rectangles, the mesh is considered to be always arbitrary because of the later local and wall refinements. This is needed to better represent the wall-functions inside the nozzle and the strong liquid mass fraction gradients.

2.4 Numerical study cases

The numerical study cases are constructed from combinations of the RANS turbulence models presented before, turbulent mass transport models and Eulerian interface. The order on which they are presented follow an increase of complexity logic, in an attempt to capture effects that otherwise could not be reproduced using basic representations.

As the complexity of the models increases so do the mesh details. It is necessary to perform a mesh test on every complexity level to ensure mesh-independent results. This is a delicate subject, because of the unsteadiness of the solver, averaged quantities may not always respond to a finer mesh in the same way.

2.4.1 Cases definitions

The numerical cases definitions are all based on the same study case defined in Section 1.2. Following Figure 2.5 definitions:

- The nozzle diameter is $d_n = 1.2 \text{ mm}$, of length $L_n = 50d_n$ and pointing downwards, aligned with gravity.
- Only water is injected through the nozzle, meaning that $\tilde{u}_0 = \tilde{u}_{L,J} = 35 \text{ m/s}$ and $\tilde{Y}_0 = \bar{Y}_0 = 1$. The air is considered still.
- Turbulence boundary conditions are specified as if there is an infinite similar pipe flow upstream, with a turbulence intensity $I_t = 4\%$. This yields a $\tilde{k}_0 = 3.3 \text{ m}^2/\text{s}^2$ and an $\tilde{\epsilon}_0 = C_\mu \tilde{k}_0^{3/2} / l_t = 11700 \text{ m}^2/\text{s}^3$, with $l_t = 0.038d_n$. The Reynolds stresses are considered isotropic, so $\tilde{R}_{ij,0} = 2/3 \tilde{k}_0 \delta_{ij} \text{ m}^2/\text{s}^2$.
- The simulation time is from $t_0 = 0 \text{ s}$ to $t_f = 0.3 \text{ s}$. This ensures a full coverage of the domain, even in the external regions of the jet. The time-step of the simulation is variable, calculated from the worst case as a function of the local Courant number Co . To avoid any divergence of the simulation, $Co = 0.8$ as a maximum value is always used.

With this in consideration, all study cases are detailed next. While the title gives a short description, all the detailed information is given within.

Case 111: k-Epsilon, Y-Mod0

- Turbulence model: $k - \epsilon$, Eq. 2.17, 2.18, 2.21 and 2.22. The parameters are: $C_\mu = 0.09$, $\sigma_k = 1.0$, $\sigma_\epsilon = 1.3$, $C_{\epsilon1} = 1.44$, $C_{\epsilon2} = 1.92$, $C_{\epsilon3} = 0.0$, $C_{\epsilon4} = 1.0$, $C_{\epsilon5} = 1.0$.
- Turbulent mass-flux model: Y_{mod0} , Eq. 2.37. The only parameter is $\sigma_Y = 5.5$.

Case 112: k-Epsilon, Y-Mod0

- Turbulence model: $k - \epsilon$, Eq. 2.17, 2.18, 2.21 and 2.22. The parameters are: $C_\mu = 0.09$, $\sigma_k = 1.0$, $\sigma_\epsilon = 1.3$, $C_{\epsilon1} = 1.60$, $C_{\epsilon2} = 1.92$, $C_{\epsilon3} = 0.0$, $C_{\epsilon4} = 1.0$, $C_{\epsilon5} = 1.0$.
- Turbulent mass-flux model: Y_{mod0} , Eq. 2.37. The only parameter is $\sigma_Y = 5.5$.

Case 211: RSM, Y-Mod0

- Turbulence model: $R_{ij} - \epsilon$, Eq. 2.18, 2.23, 2.35 and 2.22. The parameters are: $C_\mu = 0.09$, $C_S = 0.22$, $C_1 = 1.8$, $C_2 = 0.6$, $C_3 = 0.75$, $\sigma_\epsilon = 1.3$, $C_{\epsilon 1} = 1.44$, $C_{\epsilon 2} = 1.92$, $C_{\epsilon 3} = 0.0$, $C_{\epsilon 4} = 1.0$, $C_{\epsilon 5} = 1.0$.
- Turbulent mass-flux model: Y_{mod0} , Eq. 2.37. The only parameter is $\sigma_Y = 5.5$.

Case 212: RSM, Y-Mod0

- Turbulence model: $R_{ij} - \epsilon$, Eq. 2.18, 2.23, 2.35 and 2.22. The parameters are: $C_\mu = 0.09$, $C_S = 0.22$, $C_1 = 1.8$, $C_2 = 0.6$, $C_3 = 0.75$, $\sigma_\epsilon = 1.3$, $C_{\epsilon 1} = 1.60$, $C_{\epsilon 2} = 1.92$, $C_{\epsilon 3} = 0.0$, $C_{\epsilon 4} = 1.0$, $C_{\epsilon 5} = 1.0$.
- Turbulent mass-flux model: Y_{mod0} , Eq. 2.37. The only parameter is $\sigma_Y = 5.5$.

Case 222: RSM, Y-Mod1

- Turbulence model: $R_{ij} - \epsilon$, Eq. 2.18, 2.23, 2.35 and 2.22. The parameters are: $C_\mu = 0.09$, $C_S = 0.22$, $C_1 = 1.8$, $C_2 = 0.6$, $C_3 = 0.75$, $\sigma_\epsilon = 1.3$, $C_{\epsilon 1} = 1.60$, $C_{\epsilon 2} = 1.92$, $C_{\epsilon 3} = 0.0$, $C_{\epsilon 4} = 1.0$, $C_{\epsilon 5} = 1.0$.
- Turbulent mass-flux model: Y_{mod1} , Eq. 2.38. The only parameter is $C_Y = 0.016$.

Case 232: RSM, Y-Mod2

- Turbulence model: $R_{ij} - \epsilon$, Eq. 2.18, 2.23, 2.35 and 2.22. The parameters are: $C_\mu = 0.09$, $C_S = 0.22$, $C_1 = 1.8$, $C_2 = 0.6$, $C_3 = 0.75$, $\sigma_\epsilon = 1.3$, $C_{\epsilon 1} = 1.60$, $C_{\epsilon 2} = 1.92$, $C_{\epsilon 3} = 0.0$, $C_{\epsilon 4} = 1.0$, $C_{\epsilon 5} = 1.0$.
- Turbulent mass-flux model: Y_{mod2} , Eq. 2.39. The parameters are: $\sigma_Y = 5.5$, $\sigma_F = 1.0$, $C_{Fb} = 0.1$, $C_{F1} = 4.0$, $C_{F2} = 0.1$, $C_{F3} = 0.0$, $C_{F4} = 4.0$.

Case 311: RSM, Y-Mod0

- Turbulence model: $R_{ij} - \epsilon$, Eq. 2.18, 2.23, 2.36 and 2.22. The parameters are: $C_\mu = 0.09$, $C_S = 0.22$, $C_1 = 1.8$, $C_2 = 0.6$, $C_3 = 0.75$, $\sigma_\epsilon = 1.3$, $C_{\epsilon 1} = 1.44$, $C_{\epsilon 2} = 1.92$, $C_{\epsilon 3} = 0.0$, $C_{\epsilon 4} = 1.0$, $C_{\epsilon 5} = 1.0$.
- Turbulent mass-flux model: Y_{mod0} , Eq. 2.37. The only parameter is $\sigma_Y = 5.5$.

Case 312: RSM, Y-Mod0

- Turbulence model: $R_{ij} - \epsilon$, Eq. 2.18, 2.23, 2.36 and 2.22. The parameters are: $C_\mu = 0.09$, $C_S = 0.22$, $C_1 = 1.8$, $C_2 = 0.6$, $C_3 = 0.75$, $\sigma_\epsilon = 1.3$, $C_{\epsilon 1} = 1.60$, $C_{\epsilon 2} = 1.92$, $C_{\epsilon 3} = 0.0$, $C_{\epsilon 4} =$

1.0, $C_{\epsilon 5} = 1.0$.

- Turbulent mass-flux model: Y_{mod0} , Eq. 2.37. The only parameter is $\sigma_Y = 5.5$.

Case 322: RSM, Y-Mod1

- Turbulence model: $R_{ij} - \epsilon$, Eq. 2.18, 2.23, 2.36 and 2.22. The parameters are: $C_\mu = 0.09$, $C_S = 0.22$, $C_1 = 1.8$, $C_2 = 0.6$, $C_3 = 0.75$, $\sigma_\epsilon = 1.3$, $C_{\epsilon 1} = 1.60$, $C_{\epsilon 2} = 1.92$, $C_{\epsilon 3} = 0.0$, $C_{\epsilon 4} = 1.0$, $C_{\epsilon 5} = 1.0$.
- Turbulent mass-flux model: Y_{mod1} , Eq. 2.37. The only parameter is $C_Y = 0.016$.

Case 332: RSM, Y-Mod2

- Turbulence model: $R_{ij} - \epsilon$, Eq. 2.18, 2.23, 2.36 and 2.22. The parameters are: $C_\mu = 0.09$, $C_S = 0.22$, $C_1 = 1.8$, $C_2 = 0.6$, $C_3 = 0.75$, $\sigma_\epsilon = 1.3$, $C_{\epsilon 1} = 1.60$, $C_{\epsilon 2} = 1.92$, $C_{\epsilon 3} = 0.0$, $C_{\epsilon 4} = 1.0$, $C_{\epsilon 5} = 1.0$.
- Turbulent mass-flux model: Y_{mod2} , Eq. 2.39. The parameters are: $\sigma_Y = 5.5$, $\sigma_F = 1.0$, $C_{Fb} = 0.1$, $C_{F1} = 4.0$, $C_{F2} = 0.1$, $C_{F3} = 0.0$, $C_{F4} = 4.0$.

2.4.2 HPC Cluster

The mesh size, and the subsequent maximum time-step allowed for the simulations, create a heavy time consuming study case. Using a normal workstation computer, it would take months or even years to complete a whole simulation case if a fine grid is used.

For this reason, a parallel calculation is needed to increase the overall speed. It works by cutting the mesh into smaller pieces, solving each one of them in a cluster array of computers. This is a common practice in every CFD software and some key considerations on the resources used by this process are detailed here.

All cases run in a High Performance Computer (HPC) cluster at CINES (Centre Informatique National de l'Enseignement Supérieur), under the allocation c20152b7363 and c20162b7363 made by GENCI (Grand Équipement National de Calcul Intensif) in France.

The HPC is a Bull machine called OCCIGEN (2015 model). It has a total of 50544 cores distributed in 2106 nodes, each one with 2 Intel 12-Cores processors (E5-2690 at 2.6 GHz) with 64 or 128 GB of RAM. The operating system is a Linux based system, the BullX AE4 based on Redhat 6.4.

The OpenFOAM version is v2.4.0 and is compiled in the OCCIGEN machine, along with the customised modules with every extra model implemented. The parallel jobs in OpenFOAM communicate with each other via MPI (Message Passing Interface), where a custom BullxMPI version, already made available by CINES, is used.

Chapter 2. Numerical modelling

To test the performance of the parallel simulation, one of the simulation cases is used as a test platform for scalability, where the speed-up of a parallel simulation cases is studied as a function of the parallel workers used. A series of sub-cases are created from it, by decomposing the simulation in a scaling number of nodes and giving them the same task. *Case 112* is selected, and the task is to advance from the solution at $t_i = 0.1$ s to $t_i = 0.11$ s in a mesh size of 6068720 elements. The decomposition is detailed in Table 2.4.

Table 2.4 – Number of decomposed regions in the scalability test.

Scaling case	Number of nodes	Decomposed regions
0	1	24
1	2	48
2	4	96
3	8	192
4	16	384
5	32	768
6	64	1536

If the scaling is perfect, every time that the number of nodes is doubled, the time to accomplish the given task should be divided by 2 (theoretical speed-up). This is true up to a limit, where the quantity of information shared under the MPI forms a bottleneck, relative to the velocity of the process itself inside the processor. This effect is shown in Figure 2.7, where the real speed-up is compared to the theoretical as a function of the number of parallel nodes.

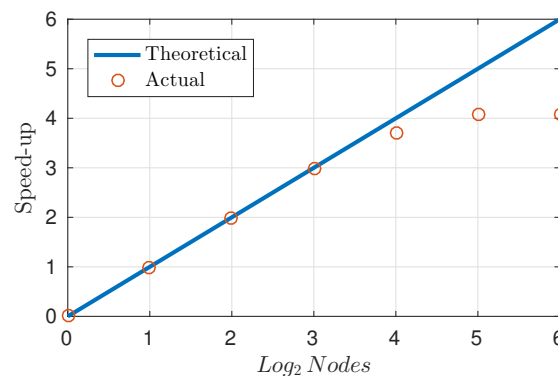


Figure 2.7 – Scalability test for the parallel decomposition of a simulation case.

It is clear that for this case the optimum speed-up is reached at 192 processors. Beyond this point, the parallel calculation is not optimal, although 384 could be used to gain time in sacrifice of performance. The maximal optimum tested point (192 cores) corresponds to ~ 30000 elements per processor.

2.4.3 Mesh convergence test

The final test is performed in the study cases themselves, where every family of cases is tested under a mesh sensitivity analysis. This is done in a wide variety of cases because it is difficult to predict how the solution behaves when the model becomes more complex. The models selected cases are: **Case 112**, **Case 212** and **Case 312**.

From the numerical discretization schemes described before, an *upwind* (first order) scheme is chosen to start every simulation case. With the solution at $t = 0.01$ s, a change to a second order scheme is made and the simulation continues to the end. The mesh test consists in testing the solution at $t_f = 0.3$ s with several meshes, hoping that further refinements do not change the overall solution. The mesh sizes are detailed in Table 2.5.

Table 2.5 – Mesh configurations for the mesh solution convergence test.

Designation	Number of elements
Mesh 00	97770
Mesh 01	766440
Mesh 02	6068720

The non-convergence of a solution comes from two main sources: numerical diffusion from convective schemes and poor representation of gradients due to interpolation. These effects are easily seen when radial profiles are presented in zones with strong velocity gradients and, because of the strong density ratio between ρ_L and ρ_G , in zones with strong mixture density gradients.

To visualise this effect, a comparison of the axial velocity against radial distance for the three meshes and the three cases is presented in Figure 2.8.

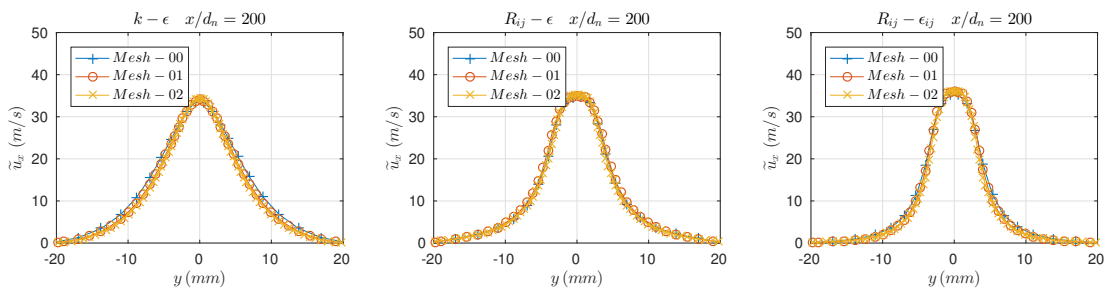


Figure 2.8 – Mesh convergence analysis on the mean axial velocity using three different turbulence models. Radial profile at $x/d_n = 200$.

The profiles at $x/d_n = 200$ are chosen because they still present strong gradients in all quantities, before going into a more dispersed part of the jet. The solution is shown along with the very cell centre values, allowing to see the quality and uniformity of the mesh along the

Chapter 2. Numerical modelling

solution profile.

This result shows clearly that the possible numerical diffusion does not come from the convective scheme in the momentum equation, making the second order scheme adopted both enough accurate and stable.

Nevertheless, there are several other quantities affected by numerical diffusion. The shear component of the Reynolds stresses is one of them (\bar{R}_{12}), because it involves the calculation of gradients in multiple directions and from other quantities as well. The results at the same distance from the nozzle are shown in Figure 2.9.

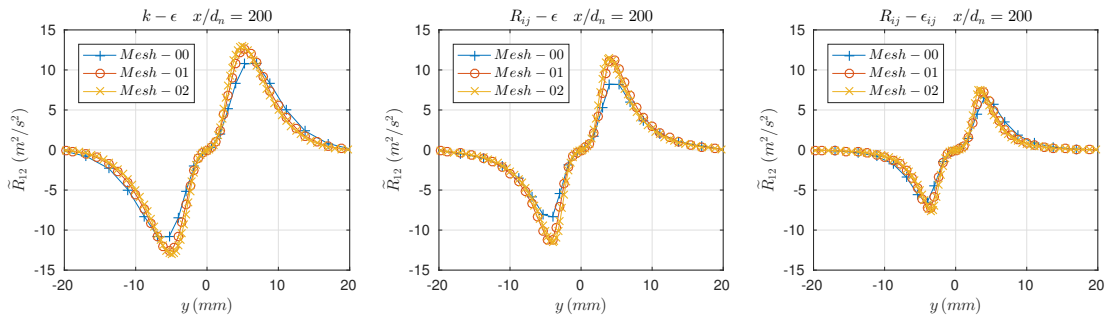


Figure 2.9 – Mesh convergence analysis on the Reynolds stresses using three different turbulence models. Radial profile at $x/d_n = 200$.

Here, a more significant result on the mesh convergence can be seen. For the coarser mesh, the quantity is not well represented, whereas little difference can be found for the later two cases. This result might give a possible candidate for running all the numerical simulations.

But, the most problematic equation that drives the numerical diffusion in this model is the solution to Eq. (2.12). The density ratio between ρ_L and ρ_G imposes strong gradients to represent both the convection and the interpolation schemes in this equation. These effects appear clearly in Figure 2.10, where the solution of the volume fraction \bar{Y} is shown.

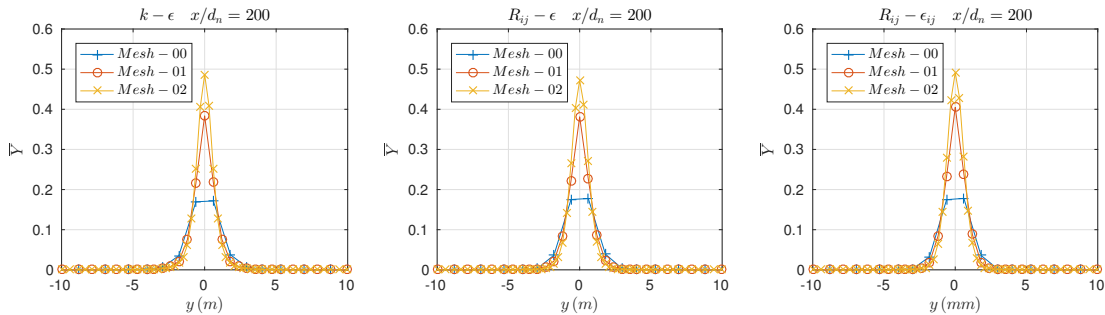


Figure 2.10 – Mesh convergence analysis on the liquid volume fraction using three different turbulence models. Radial profile at $x/d_n = 200$.

The candidate from before is discarded then. As shown in all the family of cases, this quantity only begins to converge with the finest mesh resolution of 6068720 elements. An even more refined case solution could be attempted, but given the marginal improvements in all the other quantities, and the huge computation resources that this attempt may require, this is discarded.

Summary

From the subjects developed thorough this chapter, the following points could summarise the work:

- An Eulerian mixture multiphase model is used to describe the original two-phase flow in a liquid atomization problem. The model is an extension from the original work proposed by Vallet et al. [60], which has been tested in several atomization cases by other authors.
- The focus is centred on the turbulence modelling of the flow. Several U-RANS turbulence models are used, like $k - \epsilon$ and some variations of RSM. The influence on the modelling of some expressions, within those turbulence models, is the main study subject, most noticeably those related to the variable density description of the mixture flow.
- A custom numerical solver is implemented using the OpenFOAM CFD code. This approach allows to build a coupling between the whole system of equations that describe the flow. The main feature is the modified PISO loop, inside the momentum equation solver, allowing it to be compatible with the turbulent mass flux while keeping the phase-incompressible nature of the solver.
- A set of study cases is created to test the behaviour of this possible set of equations. The cases describe an unsteady solution (U-RANS approach), so they consume a lot of computational resources. For this, a HPC cluster solution is used to run the cases. A good mesh convergence is found, along with an optimisation in the use of parallel computing resources.

Part of the results are presented within this chapter, the first part of them can be seen on the mesh test analysis. However, the logical choice for the study cases follows the experimental observations presented next, in Chapter 3.

The behaviour of the average velocity and turbulent fields drives the cases configuration. For this reason, the overall results are shown in a combined numerical-experimental analysis in Chapter 4.

3 Experimental campaign

Introduction

An experimental campaign is carried out on the defined study case, this provides a baseline to which the numerical model can compare. Although many experimental techniques with application in fluid dynamics exist, not all of them are suited for obtaining reliable results on multiphase flows. Therefore, before setting up the choice for this work, a brief review on the applicable techniques to liquid jets/sprays is presented.

From the definition of the study case, a simplified test scenario is constructed. The geometry and operating conditions are chosen to remove some constraints and to provide a well controlled environment for optical measurement techniques. The test subject is a round $d_n = 1.2\text{ mm}$ nozzle, constructed in PMMA/Glass to provide visual access to the internal flow, where the actual injector is a circular glass tube of length $L_n = 50d_n$, so the flow turbulence at the exit of the nozzle is completely developed. Gravity effects on the liquid dispersion are attenuated by placing the injector in an up-down direction, making the flow statistically axisymmetric. Operating conditions are chosen to place the liquid jet in a turbulent atomization regime.

The objective is then to obtain the velocity field in this two-phase flow. LDV (Laser Doppler Velocimetry) and DTV (Droplet Tracking Velocimetry) optical techniques are finally chosen, they are used to gather statistical information from both the liquid and the gas phases. The use of these optical techniques require some specific set-ups on both systems, which are carefully detailed and discussed in this chapter. The output of these measurements are the velocity field, the Reynolds stresses field and the droplets size distributions, everything on a carefully selected measurement spacial grid, well suited for the later comparison with the numerical results.

LDV measurements are carried out first along the liquid core vertical axis, the results give a rough estimation of the liquid axial-velocity component, from $x/d_n = 0$ to $x/d_n = 800$. On the vicinity, radial gas profiles are obtained using small ($\sim 1 - 2\ \mu\text{m}$) olive-oil tracers to capture the

Chapter 3. Experimental campaign

gas phase. From the Doppler-burst threshold between the liquid and oil particles, a distinction between both phases is achieved. In the dispersed zone, DTV measurements are carried out to determine several radial profiles between $x/d_n = 400$ to $x/d_n = 800$, special attention to the depth-of-field (DOF) estimation is taken in order to obtain a less biased droplet's size-velocity correlation.

3.1 Measurement techniques

In multiphase flows, the characterisation reduces to find the velocity field, along with some identification for each phase present. This technique is called velocimetry, where some general aspects are discussed here to justify its use in this study case. An extensive review of every technique can be found in Boutier [6], principally on the advantages and disadvantages as a function of the application, and the related biases and how to treat them.

To capture the velocities, laser velocimetry is often used as a non-intrusive method, meaning that the local fluid is not modified at the scales of measurement. It is based on light diffusion over tracer particles in the fluid, the challenge in multiphase flow is to properly identify and discriminate the tracers from the dispersed phases inside the mixture, adding an extra difficulty in comparison with single-phase applications (See Modarres et al. [41] work on the application of LDV in two-phase flows).

Although LDV can provide accurately enough velocity measurements, these are time-series fixed in one position where all spacial structure information is lost. To complement, PIV (Particle Image Velocimetry), LIF (Laser Induced Fluorescence) and DTV (Droplet Tracking Velocimetry) techniques allow to reconstruct instantaneous spacial fields, adding additional information on the flow structure.

In two-phase flows these techniques are often used combined. Sathe et al. [55] uses an array of high-speed cameras to separate and capture the velocity fields of both phases in a bubbly flow, at the same time, where image filtering and post-treatment algorithms are used to separate the information of each phase. However, the precision of such results is compromised when a heavily dispersed flow is present, like in poly-dispersed multiphase jet flows (Grosshans et al. [27]).

If no images from the flow are available, some intrusive methods can be use to estimate the void fraction (or presence) of a particular phase. Hong et al. [28] discusses the use of OP (Optical Probes) to estimate the sizes and velocities of droplets in a poly-dispersed spray. The technique requires some assumptions to estimate the velocities and a specific signal treatment to obtain the correct liquid volume fraction. Despite that it is indeed an intrusive method, and therefore, the flow might be modified, OPs are very precise in space, where the probe tip makes $130\mu m$ (Cartellier [7]). This characteristic makes it a good technique to complement shadow images, where the droplets are distributed on a 3D space depth-of-field (DOF), and the uncertainty of this quantity makes the estimation of the volume fraction difficult.

To have an instantaneous space information of the volume fraction, Prasser et al. [48] studies the use of a capacitive wire mesh sensor in bubbly flow. However, their current development does not allow to have a quick response time like the OP, leaving their use to less diluted applications.

Finally, the experimental techniques used in this work are LDV and DTV by shadow images.

Chapter 3. Experimental campaign

The LDV is used in different configurations, on separate measurement campaigns, to capture both liquid and gas phase velocity fields. Shadow images are used to run a DTV algorithm on the dispersed phase of the flow, this captures at the same time droplets sizes and velocities, providing a benchmark along the LDV. Shadow images also allow used to visualise the primary breakup mechanisms of the liquid jet. These techniques are applied to this specific study case and are detailed next.

3.2 Experimental set-up

As detailed in Section 1.2, a simplified test scenario is constructed to remove some constraints and to provide a more controlled environment for the optical measurement techniques. Instead of the original nozzle from Stevenin et al. [58] ($d_n = 4.37 \text{ mm}$), a smaller round $d_n = 1.2 \text{ mm}$ nozzle is constructed.

The injector is a circular borosilicate glass tube of length $L_n = 50d_n$ inserted in a PMMA (Poly methyl methacrylate) body. While providing a visual access to the internal flow, the glass surface is considered smooth, so no roughness will intervene in the boundary layer which is considered to be completely developed at $50d_n$. Gravity effects on the liquid dispersion are attenuated by placing the injector aligned with gravity in an up-down direction, making the flow statistically axisymmetric.

The injection velocity is $\bar{u}_L = 35 \text{ m/s}$, placing the atomization process in a turbulent atomization regime [53], according to Figure 1.3. The clean optical access also allows to verify that no cavitation is produced inside the glass tube. As an example, a shadow image next to the CAD (Computer Assisted Drawing) model of the nozzle is shown in Figure 3.1.

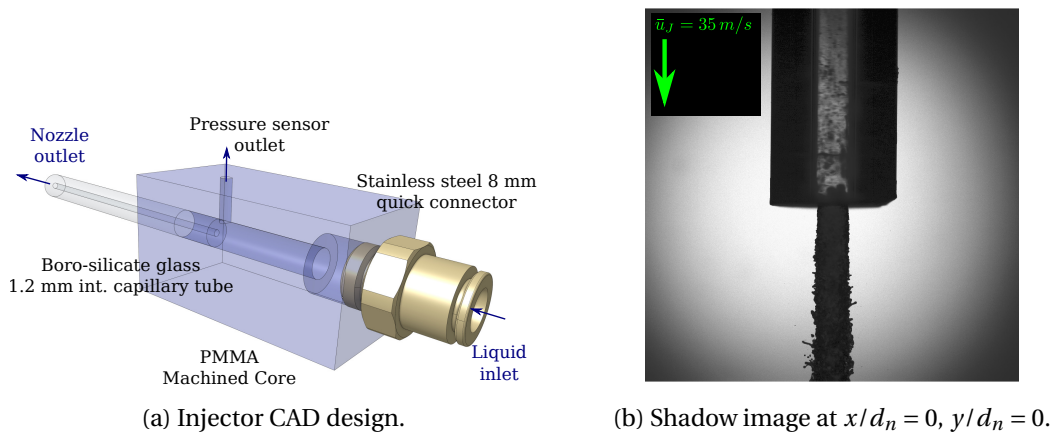


Figure 3.1 – Custom transparent $d_n = 1.2 \text{ mm}$ nozzle components and real operating conditions.

A reservoir-pump-collector hydraulic system is used to feed water to the nozzle. The system is mounted in compatibility to the visual and spatial clearance needed to perform both the LDV

and DTV measurements.

To achieve an average injection bulk velocity of $\bar{u}_L = 35 \text{ m/s}$, a relatively high pressure flow must be injected. The narrow nozzle diameter generates a pressure drop of nearly $\Delta P = 17 \text{ bar}$, so a centrifugal pump from a domiciliary water grid is not enough to achieve this ($\sim 6 \text{ bar}$). A triple-head diaphragm pump is used instead, along with a compressed air damper and a needle valve to regulate the flow rate as shown in Figure 3.2.

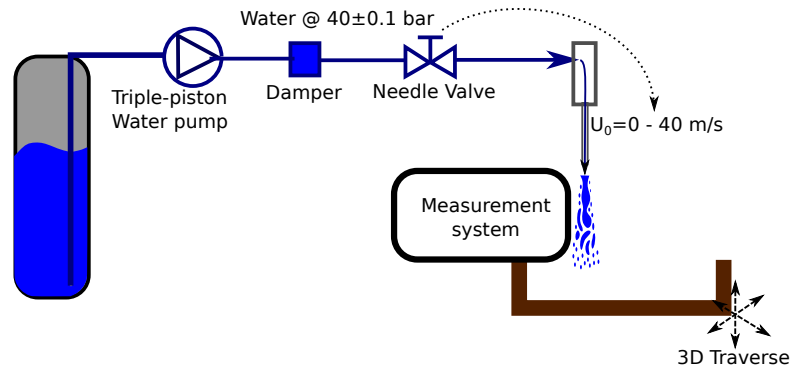


Figure 3.2 – Schematic representation of the hydraulic system connected to the injector.

To avoid clogging, purified water is used as a working fluid in a closed circuit. After the injector, the droplets are recovered and the water goes back to the reservoir. This closed circuit increases the water temperature, so an evaporating cooling system is implemented in the pump's rejection circuit. With the room temperature set at 20°C at 50% HR, the working fluid reaches a stable temperature of 24°C after 1 h.

3.3 Measurement set-up

3.3.1 LDV set-up

A two component LDV system is used to measure the liquid phase (water) and gas phase (air) velocity fields. As the liquid disperses, it is hard to make a distinction between both phases, so a specific set-up is considered for each type of measurement.

The LDV system consisted in a two component (LDV-2C) from Dantec Dynamics with an Argon-ion of $488 \text{ nm}@1.8 \text{ W}$ and $514.5 \text{ nm}@2.8 \text{ W}$ Coherent 306S laser source. A Dantec-Dynamics 60X11 transducer separates and conduct the 2C beams. A 310 mm focus-length optics is used for the emitter and 400 mm for the receiver, forming a LDV measurement volume of $2.9 \times 0.146 \times 0.146 \text{ mm}^3$ along the principal directions. A Burst Spectrum Analyser (BSA) P60, also from Dantec Dynamics, is used to analyse the raw LDV data.

Although the system provided the option for PDA (Phase Doppler Anemometry) measurements, the nature of this liquid round-jet breakup produces highly non-spherical droplets

Chapter 3. Experimental campaign

making the PDA data extremely biased. The optical arrangement is configured then to maximise the LDV data-rate in scattering mode, with a 55° detector angle and no mask in the receiver optics as shown in Figure 3.3.

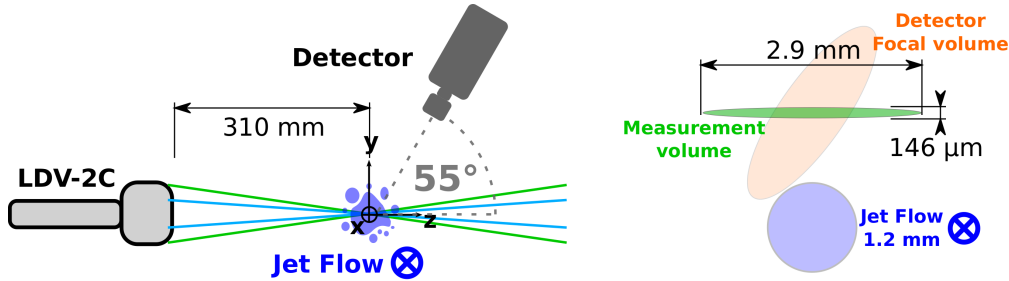


Figure 3.3 – Schematic of the 2-Component LDV set-up for measuring both the liquid and gas phases. The measurement volume size is shown next to the liquid round-jet dimensions for scale.

An extra reduction of the LDV measurement volume is achieved by the 55° detector angle, where the focusing point cuts the larger dimension as Figure 3.3 shows. This is an important feature of the set-up, because if the measurement volume is considerably larger than the liquid jet itself, a lack of detail of the resulting velocity field measurement will be found closer to the axis. Without this, spatial correlations between two distant internal points, inside the volume, could be mistaken for timed correlations in the acquired time-series.

Acquisition parameters

The details on the specific configuration for measuring the liquid and gas phases is presented here. As mentioned before, the goal is to capture the liquid phase velocity field $u_{i,L}$ and the gas phase velocity field $u_{i,G}$. When measuring only in the liquid phase, the LDV captures the velocity of the liquid/gas interface of large liquid packets or small droplets. To capture the gas phase, a second configuration uses olive-oil mist as tracers for the gas around the liquid, where the processing unit captures the velocity of small droplets of $\sim 1 - 2 \mu m$ and liquid droplets.

As described by Mychkovsky et al. [43] [42] in a fluidised bed study, a distinction between the tracers and the real particles can be made by looking at the Doppler burst signal pedestal. If one type of particle is considerable bigger than the other, the burst should have a bigger carrier pedestal too. In a transposition from their case, here the background gas phase is seeded with very small tracers compared to the poly-dispersed liquid droplets, so the same distinction should exist.

Other authors have also worked with this technique on bubbly flow, like the ones mentioned in the review made by Joshi et al. [35], where the main difficulty on this kind of LDV set-up is to capture a proper Doppler signal from the tracers in the carrier phase, when a heavy dispersed second phase is present.

However, the BSA-P60 from Dantec Dynamics available at IRSTEA Montpellier does not allow to record the Doppler burst pedestal, as this signal is eliminated from the processor at the beginning of the burst analysis inside the BSA. With this in mind, a second strategy is developed by doing two sets of measurements: a first without seeded particles in the gas phase, and a second with the seeded particles but not in the zones where a large concentration of water droplets is present.

The two different configurations for the Laser source power (LP), photomultiplier gain (PM), accepted signal-to-noise ratio (SNR) and band-pass filter (BP) are selected and shown in Table 3.1.

Table 3.1 – LDV BSA set-up for liquid and gas phases analysis.

Configuration	Laser Power	PM Gain	SNR	BP-Filter
Water	0.6 W	600 V	4 dB	Velocity-span based
Oil	1.1 W	1200 V	8 dB	Velocity-span based

Given that the LDV processing module does not allow an actual separation of the signal acquired in the gas phase configuration (olive-oil particles), some assumptions should be considered when looking at the gas-phase velocity field.

First, it is noticed that a much greater PM gain is needed to be able to see the olive-oil particles in the raw Burst-Doppler signal. By increasing this value, along with the desired signal to noise ratio limit (SNR), yields a big data-rate only for oil droplets, where although large non-spherical objects have a higher intensity, they are seen much noisier and therefore almost always rejected by SNR criterion. However, there will always be some droplets that are counted as part of the gas signal.

Second, because the signal intensity from the water droplets/sacs is higher, the gain in the PM sensitivity sets a threshold on the positioning of the measurement volume, so no overlapping between gas and liquid profiles is achieved where a large concentration of water droplets is present, to avoid damage to the PMs. To better illustrate this, a shadowgraph image is presented along with the drop-sizer algorithm and DTV post-treatment at $x/d_n = 400$, $y/d_n = 0$ in Figure 3.4. While the Liquid LDV measurements can be made regardless the y axis position, the LDV on the olive-oil tracers, for the gas phase, can only be made at the left of the orange line in Figure 3.4.

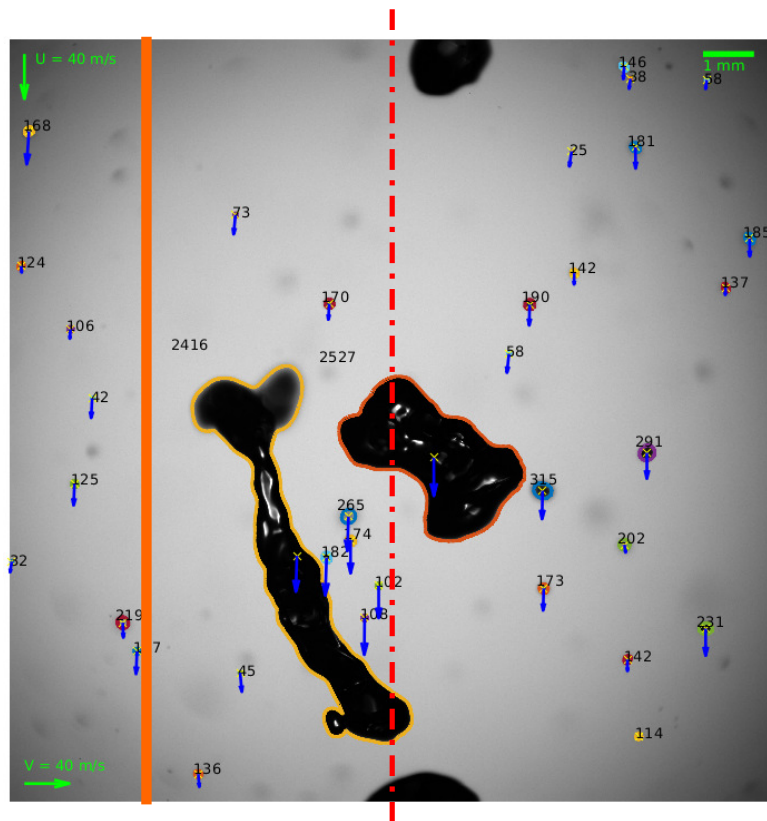


Figure 3.4 – Drop-sizing and DTV post-processing on shadowgraph images at $x/d_n = 400$, $y/d_n = 0$: jet centerline (red), $y/d_n = 4$ mark (orange line), droplets detected (coloured contours), velocity-vector (blue arrow) and equivalent diameter ($d_{[30]}$ in μm) written next to each contour detected.

An example of the difference between these two types of measurements is shown in Figure 3.5. Where the bi-variate velocity histograms are shown in a coincident point between the two profiles, precisely at $x/d_n = 400$, $y/d_n = 4$ (at the orange line in Figure 3.4).

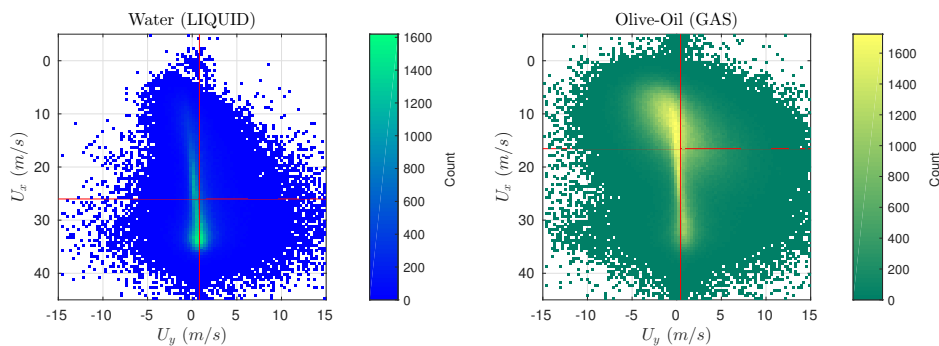


Figure 3.5 – Bi-variate histograms of both velocity components for the liquid phase (blue, left) and the gas phase (green, right). Mean values on red line levels.

The left histogram shows the data from the liquid campaign (without tracers). As expected, the velocity events are concentrated near the jet's average bulk velocity ($\bar{u}_L = 35 \text{ m/s}$), pointing slightly outwards, following the jet's lateral dispersion.

On the contrary, the right histogram shows the data from the gas campaign. This time, the velocity distribution has a wider velocity span in both components. The average gas phase entrainment is seen in the upper part, with a low $\bar{u}_{x,G}$, and $\bar{u}_{y,G} < 0$, pointing towards the centre. However, close to the centre line, the added-effect of the large water droplets that slip into the gas phase analysis can still be seen. By looking at the same region as in the left histogram, their presence is visible in gas phase measurements.

Nevertheless, given the much larger data-rate of oil droplets, seen by the amount of data concentrated out of the liquid region in the right histogram, it can be considered that the whole signal is closer to the gas-phase velocity, and not from a liquid-gas mixture. One aspect that is not investigated, however, is the correction by resident time of the particles inside the measurement volume.

As this result shows, a clear distinction between both phases can be constructed in a radial profile using this LDV method, despite the uncertainty closer to the jet's axis. It is expected that the separation between the liquid/gas velocity fields will provide a better insight on the turbulent quantities, needed for the RANS model described in Chapter 2.

Convergence analysis

Before constructing the profiles, a convergence analysis is made on every averaged quantity, calculated from the velocity time series on both liquid and gas phases.

The convergence criteria for both cases are set on the calculated Reynolds stresses. Although the worst case scenario varies from point to point (closer or far from the jet centerline), in general, the \bar{R}_{12} component drives the convergence of every other quantity. Higher order moments, like Skewness and Flatness could only find a convergence in a reasonable time closer to the jet's centre line, where the LDV data rate is high, so they are left out of the global convergence criteria.

The conditions detailed in Table 3.2 show the minimum requirements to consider a point converged in the liquid measurements campaign. They are evaluated dynamically at every acquisition point.

Table 3.2 – Convergence criteria for the LDV liquid points.

Condition	Value
Maximum Time	10 min
Maximum number of points	10^6
Residual on \bar{R}_{12}	10^{-4}

Chapter 3. Experimental campaign

Following these criteria, the convergence on the Reynolds stresses is presented in Figure 3.6 at $x/d_n = 400$, $y/d_n = 4$. It shows the calculated components as a function of the time up to which the average is calculated. The figure shows that the acquisition stopped at 10 min, meaning that the residual does not reach 10^{-4} . Despite the lack of convergence, the relative value is considered enough to represent a point in this case. This becomes more evident when looking at the real constructed profiles.

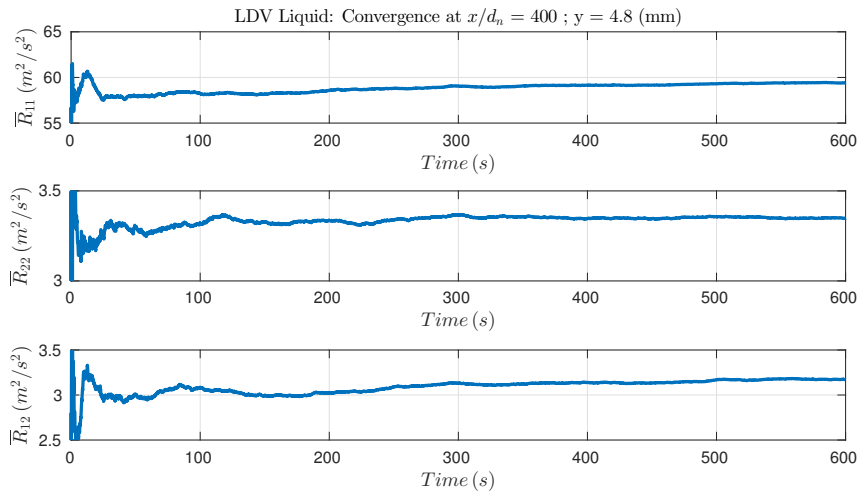


Figure 3.6 – Convergence analysis of the Reynolds stresses on the liquid phase at $[x/d_n = 400, y/d_n = 4]$.

In the same way as the liquid measurement campaign, the gas convergence criteria is summarised in Table 3.3.

Table 3.3 – Convergence criteria for the LDV gas points.

Condition	Value
Maximum Time	10 min
Maximum number of points	10^6
Residual on \bar{R}_{12}	10^{-4}

As the gas tracer particles give a higher data-rate than liquid droplets alone, the convergence this time reaches the residual threshold for \bar{R}_{12} , stopping the acquisition at $\sim 6 \text{ min}$, as Figure 3.7 shows.

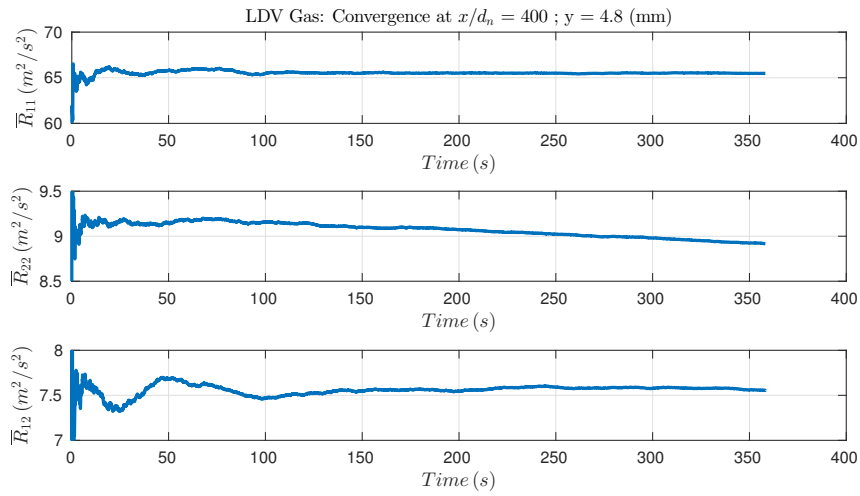


Figure 3.7 – Convergence analysis of the Reynolds stresses on the gas phase at $[x/d_n = 400, y/d_n = 4]$.

Measurement points

The spatial location of the measured points for the two LDV campaigns is shown in Figure 3.8.

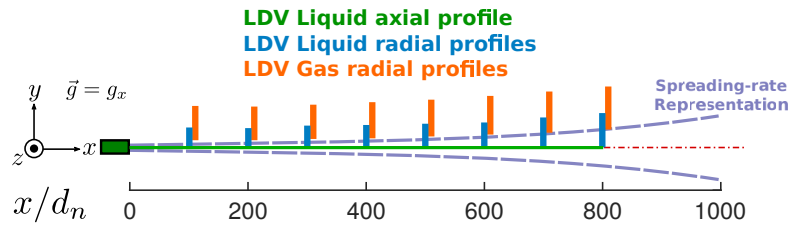


Figure 3.8 – Schematic view of the measurement points for the LDV campaign in the study case.

For the liquid campaign, a first axial profile is acquired continuously from $x/d_n = 0$ to $x/d_n = 800$. Then, radial profiles from $x/d_n = 100$ to $y/d_n = 800$ are acquired at a step of $\Delta x/d_n = 100$, following the jet spreading-rate. Because of the strong shading of the liquid jet, only radial profiles are acquired, from the centerline towards the detector. For a complete lateral profile, a second detector on the other side would be necessary.

The same procedure for the gas phase campaign is conducted, where radial profiles are acquired at the same positions. As explained before, the radial gas profiles do not touch the dense zone of the spray, and therefore they do not touch the centerline. However, they can go further out into the external zones of the boundary layer around the jet.

3.3.2 DTV set-up

Shadow images are used to run a custom DTV algorithm on the dispersed regions of the spray and to visualise the liquid column primary breakup. These images are generated by the shadow of the liquid, projected into a high-speed camera, in the presence of a perpendicular background light. The system is a *ShadowStrobe* from Dantec Dynamics, mounted as shown in Figure 3.9.

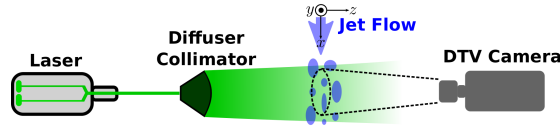


Figure 3.9 – Experimental set-up of the DTV system using shadow images.

The system captures two consecutive image frames at high speed, from which the detection and matching of particles/features can be made. The background lighting is generated by a double-pulsed laser source, consisting on a Litron Nd-YAG of 135 mJ (532 nm). The light is then conducted via fibre-optics to a diffuser/collimator, generating a non-coherent uniform background.

A PIV/DTV HiSense 4M-C CCD camera mounted with a Canon MP-E 65 mm f/2.8 lens is used. It captures 12-bit depth grey-scale images at 2048×2048 pixels in a double-layer CCD sensor. With this optical arrangement, the scale resolution is 139 pix/mm , which transforms in an image size of $14.73 \times 14.73\text{ mm}^2$.

The camera is exposed during the whole duration of a pair of captured frames, leaving to the laser firing timings control over the exposure times. In between the frames, the first image is transferred to the sensor's second layer, leaving the first one ready for the second exposure. For this reason, images must be taken in a dark room, where the actual exposition time is $\sim 4\text{ ns}$.

The acquisition frequency for a pair of images is set to $f_a = 5\text{ Hz}$. The time between pulses (tbp) vary, depending on the average velocity of the objects inside the image. This is an important parameter to set, because it should be large enough to let the droplets move in-between frames, but not much so no significant changes to the overall form and/or location pattern of the objects inside the frame is produced.

As an example, a set of raw shadow images are shown in Figure 3.10, taken at the jet's centerline, where $tbp = 5\text{ }\mu\text{s}$. Ranging from $x/d_n = 0$ to $x/d_n = 350$, a complete visualisation of the destabilisation and primary breakup can be seen. Small ligaments can be seen at $x/d_n = 0$ close to the nozzle, as Wu and Faeth [63] explains, they are related to the boundary layer inside the nozzle, where their sizes are found to be proportional to the turbulent eddies inside the injector. More downstream, at $x/d_n = 150$ some helical structures can be seen, Hoyt and

Taylor [29] explain these structures by the amplification of an helical modal instability, where aerodynamic effects start to play a more significant role in the turbulent breakup regime.

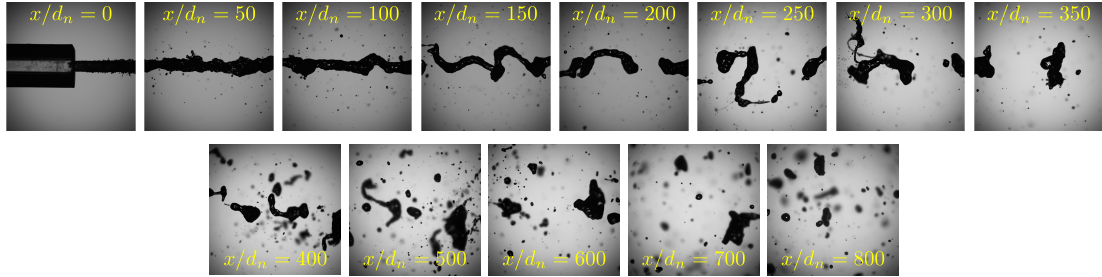


Figure 3.10 – Shadow images at the jet centerline from $x/d_n = 0$ to $x/d_n = 800$.

Liquid column breakup length

Following the original work by Wu et al. [64] and Sallam et al. [53], a characterisation of the breakup mechanism can be made, as a function of the breakup length L_c and droplets sizes $d_{[32]}$. Moreover, provided that the atomization regime of this study case should be the same as Stevenin et al. [58] case, the behaviour of such quantities must follow the same relations.

To tackle the first part, and to provide an immediate analysis of the atomization regime, the mean breakup length \bar{L}_c is estimated by looking at the breakup events from Figure 3.10. Each one of these images is taken from a series of 1000 at each point, from where the number of breakup events are counted at each position.

The reasoning is the following: if at a given point, at a given time, the liquid column presents a discontinuity, then, there is a probability that the first instantaneous breakup happened at that point or before, closer to the nozzle. Taking this reasoning to the limit, then the ratio of the number of events N_b to the total number of images N_T , at a given position, should follow the probability that the average breakup length \bar{L}_c to be less than or equal to the given position from the nozzle. The results of this calculation on every set of images from $x/d_n = 100$ to $x/d_n = 300$ is shown in Figure 3.11.

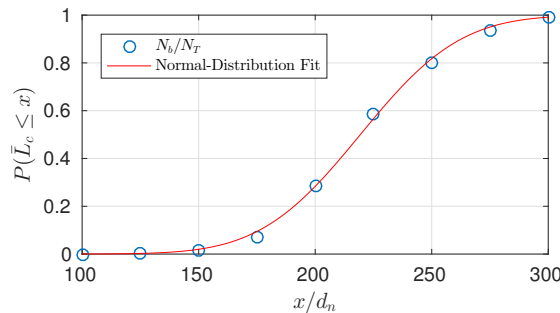


Figure 3.11 – Probability distribution of the liquid column average breakup length \bar{L}_c as a function of the normalised distance from the nozzle.

Chapter 3. Experimental campaign

As Figure 3.11 shows, the probability that $\bar{L}_c \leq x$ fits well a Normal distribution, with a mean value of $\bar{L}_c/d_n = 219$. As a reference, the relation given by Sallam et al. [53], based on a best-fit on several experiments on the same regime gives:

$$\frac{\bar{L}_c}{d_n} = 8.51 We_L^{0.31} = 203. \quad (3.1)$$

Shadow image segmentation

Having determined the breakup length, and the distance from the nozzle at which liquid column does not exist anymore, the secondary breakup of liquid packets/droplets begins. From $x/d_n = 400$ to $x/d_n = 800$, a DTV (Droplet Tracking Velocimetry) algorithm is used to characterise the dispersed part of the flow.

The main objective is to accurately detect the droplets in a shadow image and calculate their velocity using the double-frame acquisition. To do so, several image treatment techniques are used to filter and segment the shadow images. To achieve this, a custom *shadow-sizer* algorithm is developed and implemented using the *Image Processing Toolbox* in MATLAB®. This *shadow-sizer* software is an extension to the one developed by Stevenin [57].

To take advantage of the parallel computation capabilities, the new version of the code runs in parallel, on every computational core available on a x86-64 PC. In addition to that, an *nVidia CUDA* enabled graphics-card (Maxwell architecture) is used to perform heavy matrix-operations, like filtering, bi-linear interpolations and binary operations.

A step-by-step procedure on the general aspects of the code is detailed next:

- **Wavelet transform:** Based on the procedure presented by Yon [65], a Mexican-hat kernel function is used and applied as a filter to the original image (Im_{org}), the goal is to detect changes of the image gradient, therefore, amplifying the boundaries of the droplets no-matter the defocusing (Im_{wt}). Then, a dynamic threshold generates a binary image (Im_{BW}). Every object detected is then a candidate to be a droplet, as Figure 3.12 shows, where the coloured BW objects are shown to clearly identify the segmentation result.

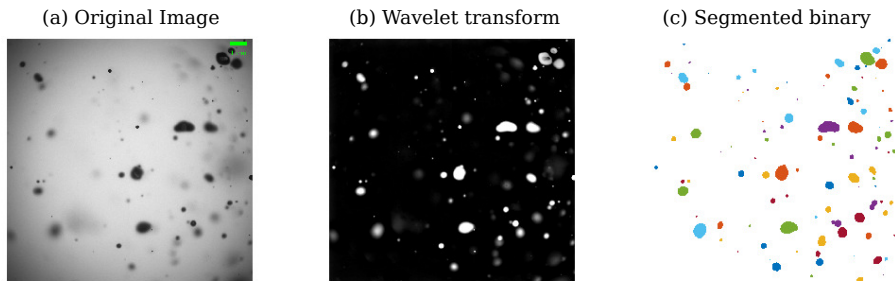


Figure 3.12 – Shadow image segmentation using MATLAB toolboxes. Image post-processing at $[x/d_n = 800, y/d_n = 12]$.

- **Local analysis:** Following the local analysis detailed by Fdida and Blaisot [20], every object is isolated and analysed locally. A local image is created for every object, by applying the binary mask of Figure 3.12-(c) to Im_{org} , resulting in a subset of smaller images Im_{loc} (local image).

The grey-level intensity of the local images are defined as i , where i_{min} and i_{max} are the minimum (dark) and maximum (bright) values. Then, the contrast ratio defined as $C = (i_{max} - i_{min}) / (i_{max} + i_{min})$ is calculated and the object is rejected from the analysis if $C < 0.1$.

- **Contours extraction:** The objects that pass the contrast filter are finally analysed. The Im_{loc} is normalised, meaning that the global grey levels from before now are $0 < i < 1$. From these normalised local images, the contours (w) at the following grey-levels (l) are extracted: $w_{l=0.25}$, $w_{l=0.50}$, $w_{l=0.61}$ and $w_{l=0.77}$. Using a bi-linear interpolation, those contours are represented in a sub-pixel domain at $10x$ the original size. Finally, using the 3D representation described by Daves et al. [10], the equivalent diameter $d_{[30]}$ is calculated. Other quantities are also kept for further analysis, like the principal axis, orientation and eccentricity. These are shown in Figure 3.13.

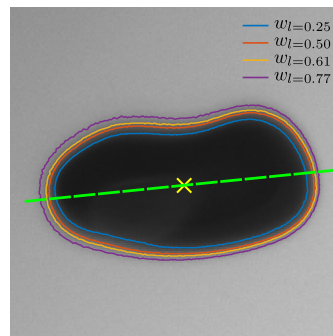
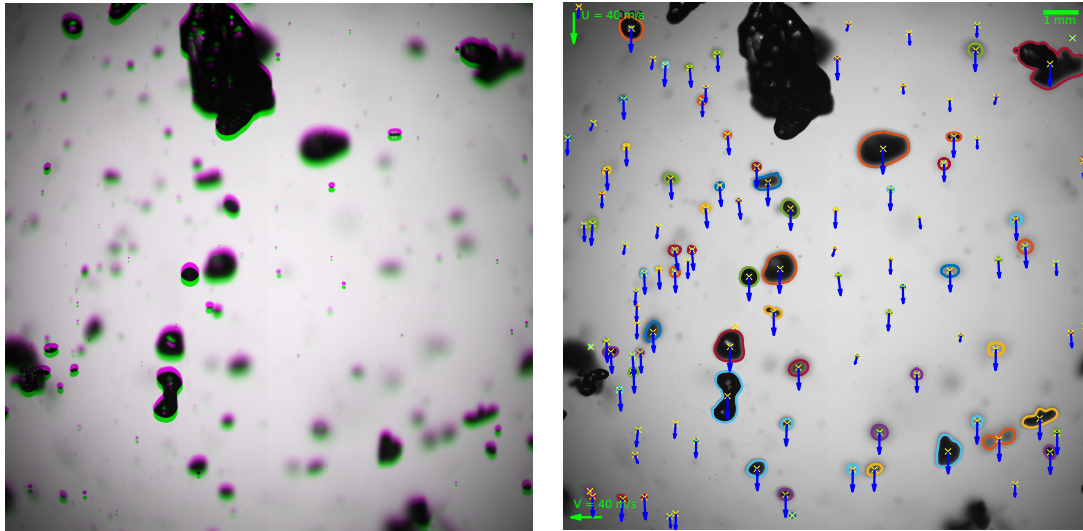


Figure 3.13 – Sub-image analysis on a detected droplet. Local contours and principal axis.

- **Velocity estimation:** Using the centroids from every droplet detected, on (x, y) coordinates in the pair of images, the *SoftAssign* matching algorithm from Gold et al. [24] is used. This creates an output matrix with the matched objects from both consecutive frames. Finally, knowing the scale resolution (139 pix/mm) and the time between images (tbp), the velocity vector of every droplet can be estimated.

The final result of the image segmentation procedure (wavelet transform and filtering, local analysis, contours extraction and velocity estimation) is shown in Figure 3.14. The information for every frame is kept for further granulometry and velocimetry of the jet.



(a) Superposition of two consecutive shadow 12-bit images using a $tbp = 5 \mu s$.

(b) Shadow-sizer and DTV post-processing. Contours at $l = 61\%$ and velocity vectors.

Figure 3.14 – Custom DTV post-processing algorithm. Image centre at $x/d_n = 600$, $y/d_n = 0$.

Depth-of-field calibration

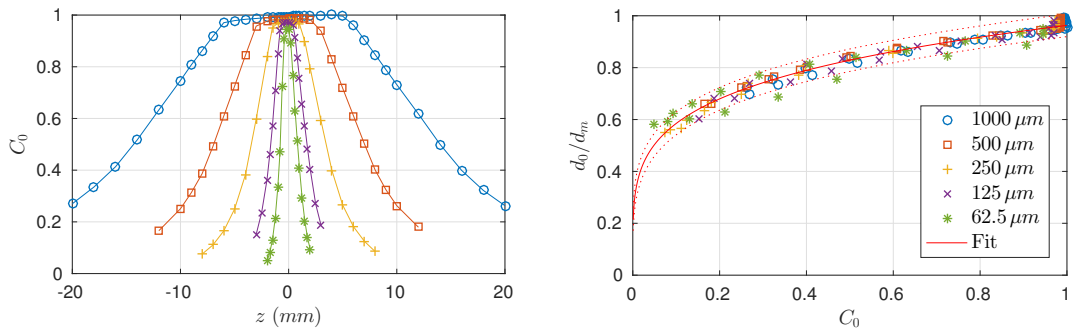
Although the Shadow-sizer algorithm can well detect out-of-focus droplets, as a function of their characteristic sizes ($d_{[30]}$), these are not always in the same plane of measurement. In a jet with cylindrical geometry, aggregating information that does not exist within the same physical space could lead to several biases in the granulometry and velocimetry.

A calibration procedure on the size of the detected objects is then conducted, following the original work by Fdida and Blaisot [20]. The response of this optical system is studied by looking at the in-focus and out-of-focus images on calibrated opaque disks of known size. Despite that droplets are transparent, the refractive index change at the surface does not influence the grey-level gradient detected at the edges of an opaque object (Fdida [19]), making this type of calibration on completely opaque objects well suited for droplets.



Figure 3.15 – ThorLabs grid distortion target. 3in x 3in, 125 to 2000 μm grid spacings, soda lime glass.

The procedure is then to use the same shadow-sizer algorithm to detect the objects contours, as a function of a known distance from the focus plane z . The calibrated objects are from a Thor-Labs grid distortion target (Figure 3.15), where 62.5, 125, 250, 500 and 1000 μm low-reflexion discs are painted in a soda lime glass support. The results are shown in Figure 3.16, as a function of the normalised contrast ratio C_0 .



(a) Normalized contrast ratio C_0 as a function of the distance from the focal plane z for all disc diameters in the target.

(b) Ratio of the measured diameter d_m at $l = 61\%$ to the actual diameter d_0 as a function of the normalized contrast ratio C_0 .

Figure 3.16 – Calibration using a commercial optical target.

Figure 3.16a shows the normalised contrast ratio C_0 (C , where $C_{max} = 1$), for every disc real size, against the distance from the focal plane z . A difference on the response to the focal plane distance can be seen for every type of object, this generates a Depth-of-Field (DOF) as a function of the size of the object.

As also shown by Fdida and Blaisot [20], Figure 3.16b shows the ratio of the actual size of the objects d_0 to the measured d_m at $l = 61\%$ ($(d_{[30],l=61\%})$) against the normalised contrast ratio C_0 .

Chapter 3. Experimental campaign

From this, it can be seen that the overestimation of the real size follows the same relation no matter the original size nor the out-of-focus distance and it is only a function of the contrast ratio.

Following this analysis, every equivalent diameter $d_{[30]}$, extracted from the contours at $l = 61\%$, for every droplet detected in this study case, can be corrected only by looking at the calculated contrast ratio C .

This calibration methodology has been developed and tested on cases with nearly round objects. Here, however, its use is questionable, where heavy deformed large packets of liquid can be found and the definition of an equivalent diameter is only referential. These corrections are finally not applied to the results presented in Chapter 4, but they are kept as a reference about the response of the optical system. This notion of DOF is useful to give a proper interpretation for the velocity and fluctuations fields presented in Chapter 4.

Convergence analysis

With the analysis on the images in mind, where the droplets sizes and velocities are extracted, the resulting long series of data are used to construct averaged quantities. In a similar way as in the LDV case, the average velocity field of these droplets are represented in a spatial grid. An analysis on how this average representation behaves is presented next.

To construct the average fields, a convergence analysis is first performed as a function of the number of images (N) needed to have representative average fields. A previous work performed Stevenin [57] shows that the joint distribution of droplets sizes and velocities is very sparse for a similar liquid jet, meaning that the average velocity field has a strong dependence on the droplets distribution. It is therefore important to study how many objects are detected and validated in each pair of frames, for when the averaged velocity and droplet's size fields are constructed, those quantities seem converged on a N number of total images.

Subsequently, an analysis based on a specific distribution of droplets by class of diameter is proposed. The aim is to specify a decomposition by sizes where the average fields are calculated. To do so, the following parameters are set:

1. The partition should be the same for the whole analysis. It is known that large droplets will exist only close to the centerline and will tend to disappear in the outside regions. The partition proposed must not change according to this, and if large droplets do not exist at one point, the class is considered non-existent.
2. The distribution should be minimal. Meaning that a partition of many classes that has the same behaviour of a smaller one is discarded.
3. The average quantity must be independent if weighted by the diameter inside the class

(i). Meaning that, if h is the quantity to average, then:

$$\bar{h} = \frac{\overline{dh}}{\bar{d}}. \quad (3.2)$$

4. The number of elements should allow a convergence of the average inside the class.
5. To avoid loners, a minimum of 100 elements is allowed inside a class. If not, the class is considered non existent on that point. This is imposed principally because the average on large droplets will never converge outside the jet centre line, despite that some rare events occur.

Following these directives, the following partition by droplet equivalent diameter class is proposed in Table 3.4.

Table 3.4 – Partition of droplets population by class of diameter.

Class 1:	$d_{[30]} \leq 0.10 \text{ mm}$
Class 2:	$0.10 \text{ mm} < d_{[30]} \leq 0.25 \text{ mm}$
Class 3:	$0.25 \text{ mm} < d_{[30]} \leq 0.50 \text{ mm}$
Class 4:	$0.50 \text{ mm} < d_{[30]} \leq 0.75 \text{ mm}$
Class 5:	$0.75 \text{ mm} < d_{[30]} \leq 1.00 \text{ mm}$
Class 6:	$1.00 \text{ mm} < d_{[30]}$

To justify the use of this partition, the analysis is presented at $x/d_n = 600$, $y/d_n = 0$ (see Figure 3.14), on a set of 1000 images. The data collected corresponds to a 1/5th of the image in the central point, using the sub-image partition.

The averaging procedure is the following. *Average* is the mean velocity component \bar{u}_i , calculated from the arithmetic average, over n objects (droplets) identified as j inside the class (k),

$$\bar{u}_{i,(k)} = \frac{1}{n} \sum_{j=1}^n u_{i,\{j \in (k)\}}; \quad (3.3)$$

and *d-Average* is the same mean velocity component \bar{u}_i , but calculated from the weighted average, over the same objects, by the droplet $d_{[30]}$ diameter, meaning:

$$\bar{u}_{i,(k)} = \frac{\sum_{j=1}^n d_{[30],\{j \in (k)\}} u_{i,\{j \in (k)\}}}{\sum_{j=1}^n d_{[30],\{j \in (k)\}}}. \quad (3.4)$$

Using this, the influence of the droplet sizes, inside a class, is weighted in the mean velocity estimation. The convergence is shown in Figure 3.17 for the velocity field.

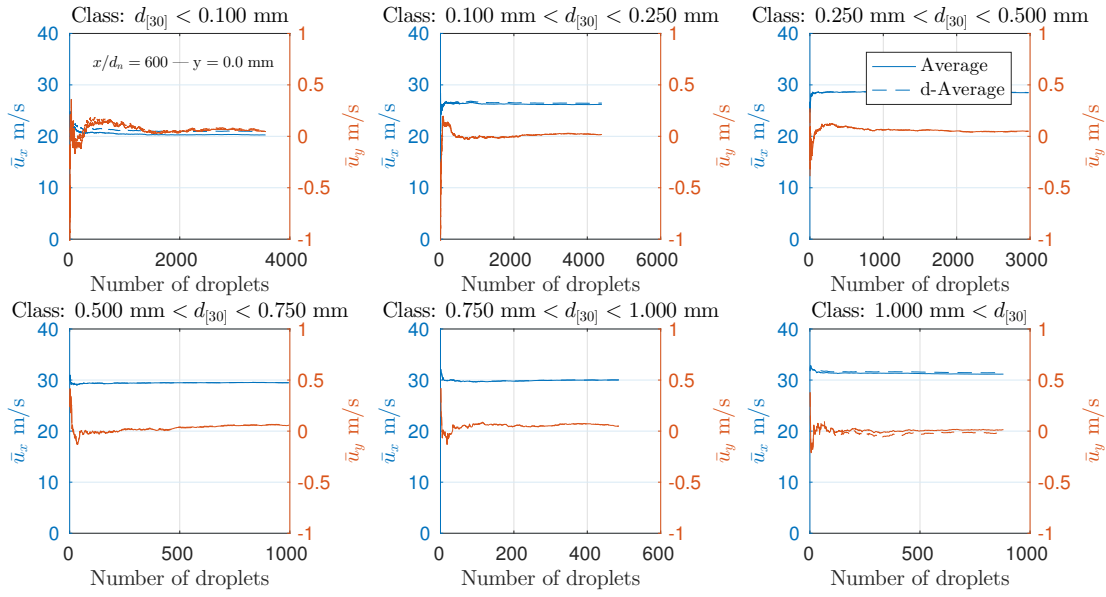


Figure 3.17 – Convergence analysis on the mean velocity by droplet's class diameters. Sub-image count at $[x/d_n = 600, y = 0 \text{ mm}]$.

To summarise, this analysis shows that 1000 images are enough to represent the average velocity field, under this partition by class of droplet diameter, on a sub-image of a $1/5^{th}$ of the original lateral size.

However, this is not always true for the calculated Reynolds stresses. These are calculated relative to the average by class shown before. Figure 3.18 shows the same analysis on the principal Reynolds stresses by class, $\bar{R}_{11}^{(i)}$ and $\bar{R}_{22}^{(i)}$.

The same principle apply for the Reynolds stresses calculation. *Average* uses the arithmetic average:

$$\bar{R}_{ij,(k)} = \frac{1}{n} \sum_{l=1}^n (u_{i,\{l \in (k)\}} - \bar{u}_{i,(k)}) (u_{j,\{l \in (k)\}} - \bar{u}_{j,(k)}); \quad (3.5)$$

and *d-Average* is calculated as a weighted average by the droplet $d_{[30]}$ diameter, meaning:

$$\bar{R}_{ij,(k)} = \frac{\sum_{l=1}^n d_{[30],\{j \in (k)\}} (u_{i,\{l \in (k)\}} - \bar{u}_{i,(k)}) (u_{j,\{l \in (k)\}} - \bar{u}_{j,(k)})}{\sum_{l=1}^n d_{[30],\{l \in (k)\}}}. \quad (3.6)$$

Since the population of large droplets is considerably lower in the bigger class, the convergence on the number of droplets needed does not always meet. Moreover, there is a difference this time as a function of the weighted average inside the class, as shown by the dotted lines against the continuous one.

Despite all these difficulties the partition by class is kept and the number of images is not

modified either. As the later results show, the extra precision that can be gained by re-setting those parameters would not change the analysis.

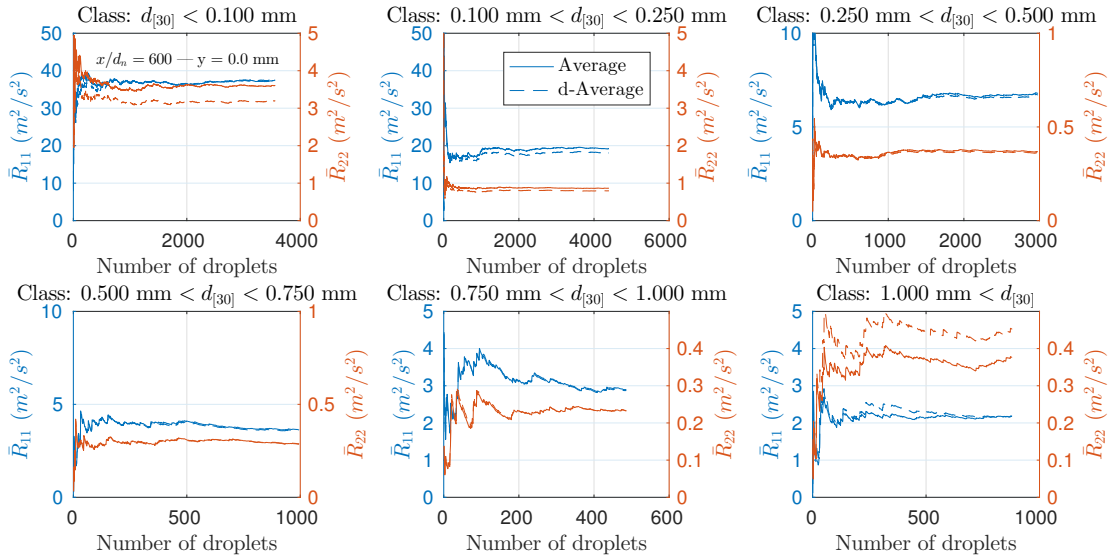


Figure 3.18 – Convergence analysis on the Reynolds stresses by droplet's class diameters. Sub-image count at $[x/d_n = 600, y = 0 \text{ mm}]$.

Measurement points

As detailed before, all statistics are in a spatial partition of the original image. Since the spatial resolution is rather big (139 pix/mm; 14.73 mm), there are strong gradients of any quantity if represented in a lateral profile inside a 2048x2048 pixels frame. To show this effect, the joint probability density *pdf* of all events u_x - u_y , u_x - $d_{[30]}$ and u_y - $d_{[30]}$ in a sub-image analysis is presented in Figure 3.19.

This shows that the distributions of velocities and sizes vary a lot inside the image itself. These points are represented centred on the slices (see Figure 3.20). The probability density functions (*pdf*) are constructed from the histograms. A partition of 50 bins is used to do the count on every axis, where the white bins are the zones with zero counts. The solid lines represent the average values and the dashed ones the standard deviation.

Then, the reconstruction of radial profiles is performed by considering only the information extracted at the central slices, like Figure 3.20 shows. This is called a super-resolution profile, giving an extra spatial precision on the averaged quantities.

The images are acquired laterally with a step of 4.8 mm, meaning that there is a large overlapping of information. This produces a good quality profile, with enough resolution to perform further operations, like spatial derivatives.

Chapter 3. Experimental campaign

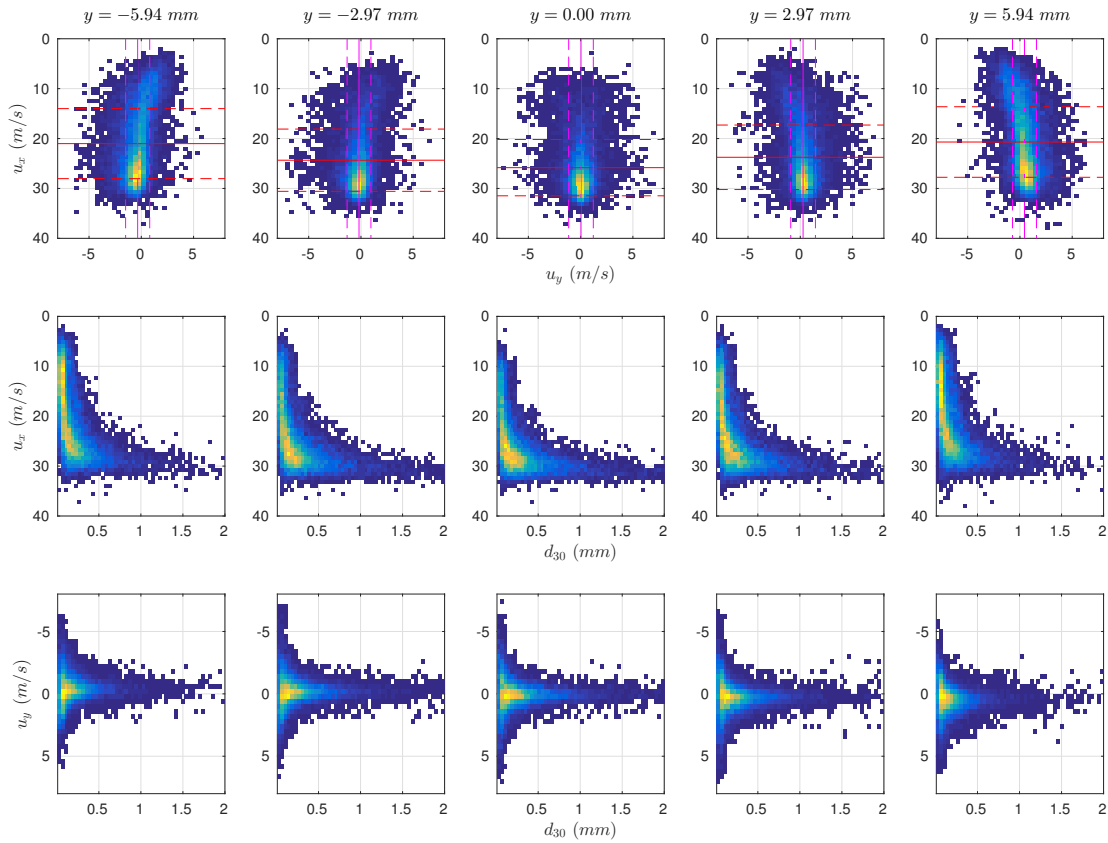


Figure 3.19 – Bi-variate histograms normalised as a *pdf* for: u_x - u_y , u_x - $d_{[30]}$ and u_y - $d_{[30]}$. Sub-image count at $[x/d_n = 600, y = 0 \text{ mm}]$.

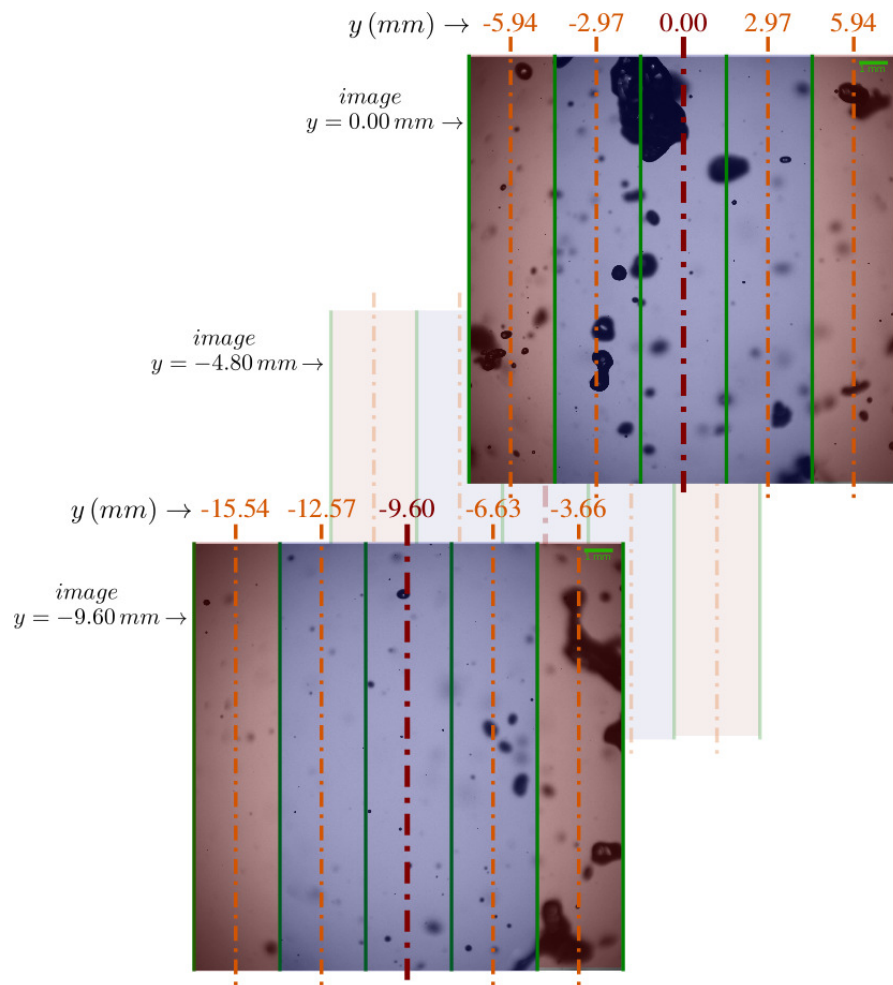


Figure 3.20 – Super-resolution profile reconstruction by overlapping of sub-image data. Blue zones are kept, red are discarded. Example at $x/d_n = 600$.

Finally, similar to the LDV case, this process is repeated on the locations detailed in Figure 3.21, completing the DTV measurement campaign.

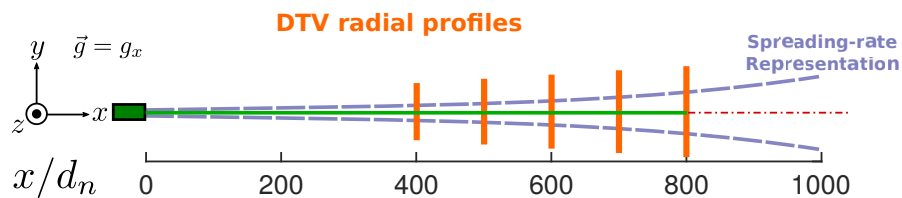


Figure 3.21 – Schematic view of the measurement points for the DTV campaign.

Summary

A detailed description of the experimental techniques applied to a study case is given in this chapter. From this development, the following points could summarise the topics treated:

- LDV and DTV measurements systems are chosen to carry out the experimental campaign. Both systems have been tested before in similar cases by other authors. The objective is to capture the velocity fields of both gas and liquid phases, along with the distribution of droplets sizes in the dispersed region of the flow. Additionally, shadow images taken close to the nozzle allow a visualisation of the liquid column breakup behaviour.
- The study case consists in a circular glass tube nozzle of $d_n = 1.2 \text{ mm}$. This geometry allows a direct equivalence with the simulation cases in Chapter 2. Although this nozzle does not exist in any real application, this simplified case provides a better controlled environment to perform the experiments, with less incertitude on the operating conditions.
- The LDV technique is applied to measure both liquid and gas phases. These measurements are carried out in separate experimental campaigns. The liquid campaign is performed in the dense and dispersed part of the jet. For the gas campaign, olive-oil mist is used as passive tracers in the surrounding air. A special set-up in the acquisition parameters of the LDV (BP filter, SNR, PM gain) is used to discriminate the average signal from the tracers and the residual part from the liquid droplets. This configuration allows to capture the average and fluctuating components of the liquid/gas slip-velocity, an important quantity to compare with the U-RANS model.
- Shadow images are acquired to run a custom DTV algorithm. From this technique, the droplets sizes and velocity distribution are obtained, a more detailed piece of information than the one inferred from the average liquid LDV. A strong relation of the droplets distribution with both average and turbulent velocity fields is found. This means that a correct estimation of the DOF is crucial to get an accurate velocity field. To tackle this incertitude, a calibration procedure is carried out using a calibrated target.

Some of the experimental results are shown in this chapter as an example. This is done to show how the set-up is done and how the raw data from the LDV and DTV are integrated into the construction of the averaged fields.

4 Results

Introduction

On this chapter, the results from the simulation cases are presented along with the experimental observations all-together. The development of this work does not follow the same logic separation of the numerical and experimental chapters. Indeed, the results are presented in a way so that the mixture multiphase flow model used here could be compared and explained with and by the experimental observations.

The experimental results are presented first. Their analysis allows to characterise and to set some overall parameters on the dynamics of the studied liquid jet. The decay of the centerline velocity or the spreading-rate on a round-jet are some immediate useful parameters to look-up to, these set the first baseline to quickly compare against numerical simulations. Later, the mean and fluctuating velocity fields are obtained from both LDV and DTV measurement campaigns, these quantities are useful to analyse the behaviour of the turbulence RANS model used [47][8][56].

Great effort also is put into the numerical simulations, where the custom solver is constructed and implemented using the *OpenFOAM* CFD code. Although the construction and test of this solver could be a subject on its own, based on the experimental observations, a series of study cases are created to test the behaviour of such formulations, which are only applied to this study case. Always centred on the same Favre-averaged mixture multiphase modelling, some variations of $k-\epsilon$ and RSM turbulence models are compared, along with first and second-order closures for the modelled turbulent mass transport fluxes [60].

As previously mentioned, one of the main challenges of this work is to find an explanation to the strong anisotropy found on the Reynolds stresses principal components [58]. A combined approach, from the experimental observations, seen by the RSM turbulence model, could provide some clues on this behaviour.

4.1 Experimental observations

The experimental observations are based on the data provided by the LDV and DTV campaigns. From these data, two main quantities are calculated: the average velocity field and the Reynolds stresses. Some special particularities are involved when performing these calculations, like the ones detailed in Chapter 3. The objective is to extract the averaged fields from the liquid and gas phases separately.

In this section, the detailed results on the averaged fields are presented. A comparison between the two measurement techniques in terms of the average velocity fields and the Reynolds stresses is attempted first. The details on how these quantities evolve in comparison with the RANS model are described later on a series of simulation cases.

4.1.1 Mean velocity field

Given the cylindrical symmetry of the flow, there are only two main components involved in the velocity field: u_x and u_y , this last one similar to the radial component in a symmetry plane. No matter what type of average operator is used, the flow is always considered statistically axisymmetric.

As previously defined in Chapter 3, the averaging procedure differs slightly from the two analysis. The LDV data is always treated using a simple arithmetic average, over n events, separated by phase, meaning:

$$\bar{u}_{i,L} = \frac{1}{n} \sum_{k=1}^n u_{i,\{k \in Liq\}}; \quad (4.1)$$

$$\bar{u}_{i,G} = \frac{1}{n} \sum_{k=1}^n u_{i,\{k \in Gas\}}. \quad (4.2)$$

For the DTV, the procedure is slightly different. The first approach is to calculate the mean velocities using a simple arithmetic average, like in the LDV case, meaning that the mean velocity flagged as *Average* is:

$$\bar{u}_i = \frac{1}{n} \sum_{k=1}^n u_{i,k}; \quad (4.3)$$

whereas *d-Average* is the same mean velocity component \bar{u}_i , but calculated from the weighted average, over the same objects, by the droplet $d_{[30]}$ diameter, meaning:

$$\bar{u}_i = \frac{\sum_{k=1}^n d_{[30],k} u_{i,k}}{\sum_{k=1}^n d_{[30],k}}. \quad (4.4)$$

If the DTV data is separated by class, then a simple arithmetic average is kept, meaning that

the average velocity for the class (k) is:

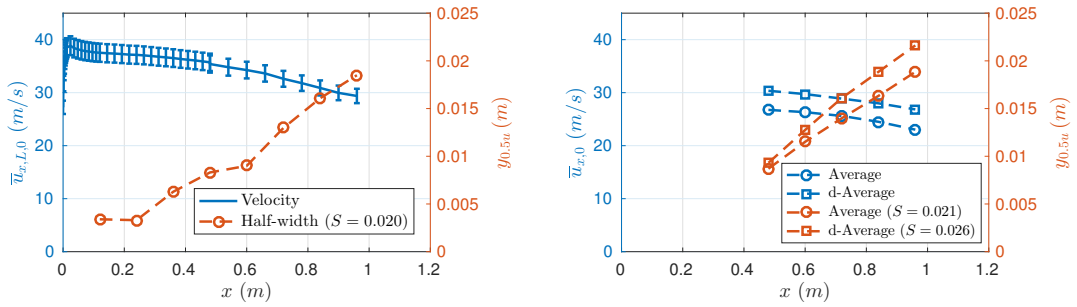
$$\bar{u}_{i,(k)} = \frac{1}{n} \sum_{l=1}^n u_{i,\{l \in (k)\}}; \quad (4.5)$$

The centerline axial velocity is then defined as $\bar{u}_{x,L,0} = \bar{u}_{x,L}(x, y = 0)$, where the underscore indicates the axis component and phase, and in parenthesis the position. From this, the axial velocity half-width $y_{0.5u}$ is the distance from the jet centerline at which $\bar{u}_{x,L}(x, y = y_{0.5u}) = \bar{u}_{x,L,0}/2$. Using this, the spreading rate S is defined as:

$$S = \frac{\partial y_{0.5u}}{\partial x}; \quad (4.6)$$

Despite the formal definition of S , it is calculated and considered linear for $x/d_n > 400$.

Using these definitions, Figure 4.1 shows the decay of $\bar{u}_{x,L,0}$ against the axial distance from the nozzle, along with the axial velocity half-width $y_{0.5u}$ for the two measurements techniques.



(a) LDV. Mean liquid axial velocity along the centerline $\bar{u}_{L,x,0}$ and half-width $y_{0.5u}$ from radial profiles.

(b) DTV. Mean liquid axial velocity along the centerline, $\bar{u}_{x,0}$ and diameter-weighted $\overline{d}u_{x,0}/\overline{d}_0$; and half-width $y_{0.5u}$ from radial profiles.

Figure 4.1 – Mean velocity axial profiles from experimental observations.

In the same way as in constant density round-jets (air-air of Hussein et al. [30]), the jet loses velocity and spreads. Figure 4.1a shows the decay of $\bar{u}_{L,x,0}$ and the spreading of the jet, characterised by the $y_{0.5u}$, using the LDV data on the positions defined in Figure 3.8. To compare, Figure 4.1b shows the same, but using the two averaging procedures proposed from the DTV profiles.

The difference between the two sets of measurements is explained by the integration volume on which the data is acquired. In one hand, the dimensions of the LDV measurement volume are $0.146 \times 0.146 \times 2.9 \text{ mm}^3$ (see Figure 3.3), making the spatial velocities integration to around the size of the jet original diameter. On the other hand, the DTV central slice (see Figure 3.20) is wide 2.9 mm too, making both comparable. However, the depth-of-field (DOF) of the DTV data has a much larger span, even for small droplets (see Figure 3.16a), meaning that the calculated DTV average of droplets velocities is integrated into a much larger volume than in

Chapter 4. Results

the LDV case. Since the axial velocity decays against the radial distance, this larger integration volume makes the DTV centerline velocity lower than in the liquid LDV case.

Although the larger droplets are seen in a larger DOE, they only exist in the central portion of the jet, and as previously seen in Figure 3.19, they tend to keep the jet bulk velocity ($\bar{u}_J = 35 \text{ m/s}$). This effect is shown by calculating the centerline velocity by class of droplet in Figure 4.2.

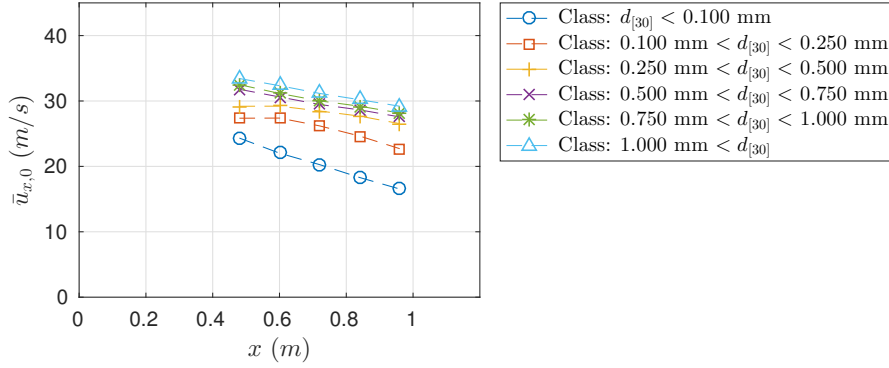


Figure 4.2 – DTV. Mean liquid axial velocity along the centerline $\bar{u}_{x,0}$ by droplets class diameters.

From the difference on these results, it is not straightforward to assimilate the LDV or DTV data to the Liquid phase velocity field. Nevertheless, this is carried forward to complete the analysis.

Contrary to a constant density case, because of the extra inertial, viscous and gravity effects on the mixture, in variable density flows there is no straightforward similarity. However, similar relations can be found in the literature. Ruffin et al. [51] studied the decay rate of several variable density flows, where the following relation can be applied:

$$\frac{\tilde{u}_{x,0}}{\tilde{u}_J} = \frac{1}{A} \left(\frac{d_n}{x - x_0} \right) \left(\frac{\rho_L}{\rho_G} \right)^b; \quad (4.7)$$

where A is the asymptotic decay rate, x_0 the abscissa at which the asymptotic behaviour begins (virtual origin) and b a power applied to the density ratio. To compare this relation with a constant density case, the nozzle effective diameter is defined as $d_n(\rho_L/\rho_G)^b$, used as a normalisation parameter.

Before presenting the calculation, it should be noted that these relations are constructed for a gas mixture. Therefore, the mixture velocity \tilde{u} is involved. Here, only the liquid phase is measured at the centerline, obtained and assimilated from LDV and DTV. However, given the high density ratio ($\rho_L/\rho_G = 828$), when $\tilde{Y} \rightarrow 1.0$ at the centerline, $\tilde{u}_{x,0} \rightarrow \bar{u}_{x,L,0}$.

Another small difference is about the injection velocity \tilde{u}_J in Eq. 4.7. \tilde{u}_J is assumed to be a top-hat flat profile, which is not true in this case. Although this does not change significantly

the results, Figure 4.3 shows the difference between the bulk velocity \bar{u}_J against the centerline injection velocity $\bar{u}_{J,0}$ at $x/d_n = 0$ (injection point). These are different because there is a developed boundary layer inside the injector, and to clarify this point, the results from a $k-\epsilon$ simulation case inside the circular injector, along with a calculated power-law $1/7th$, are shown.

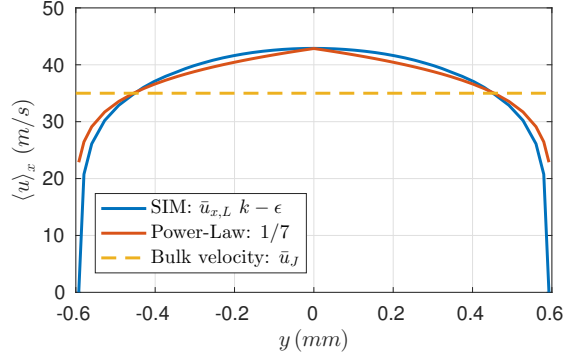
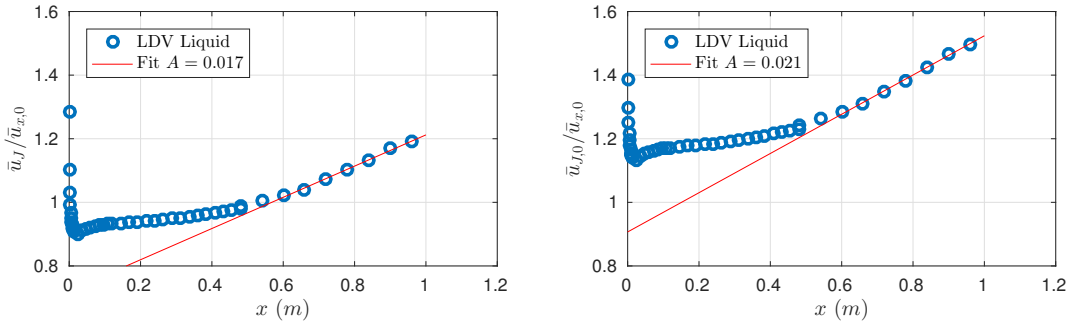


Figure 4.3 – Axial velocity profile against radial distance at $x/d_n = 0$.

With these considerations, using $b = 0.5$, the fitted value for A using Eq. 4.7 is shown in Figure 4.4. The two possible injection velocities are contrasted. Also, only the data in the dispersed region of the jet is considered, meaning that A is calculated using the data for $x/d_n > 400$, in the same way as the spreading-rate S before.



(a) Using bulk injection velocity $\bar{u}_J = 35 \text{ m/s}$. (b) Using centerline injection velocity $\bar{u}_{J,0} = 44 \text{ m/s}$.

Figure 4.4 – Liquid centerline axial velocity decay rate against axial distance.

This yields an average decay rate $A = 0.019$, nearly 10 times smaller than in the cases reported by Ruffin et al. [51] and the LDV data from Hussein et al. [30] in an air-air round jet, where $S = 0.094$. However, using the same procedure, Stevenin et al. [58] found a similar decay rate of $A = 0.0273$, and a spreading rate of $S = 0.024$.

As no more information is available, the construction of a similarity pattern using the radial profiles is attempted next. $\bar{u}_{x,L,0}$ and $y_{0.5u}$ are used as normalising quantities. Figure 4.5

presents both the axial and lateral liquid velocities, using this procedure.

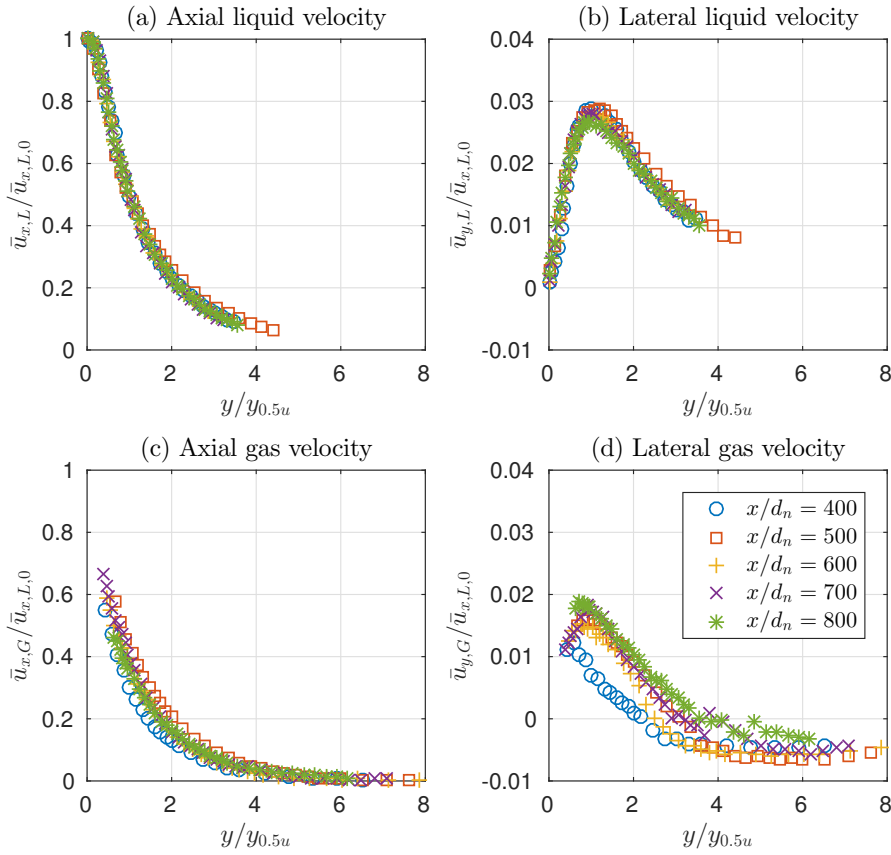


Figure 4.5 – Velocity field from the Liquid and Gas LDV campaign. Profiles against radial distance from $x/d_n = 400$ to $x/d_n = 800$.

A similarity is found on both components in the liquid part, but the shape differs from a single phase jet. While the axial component decays slower against the radial distance, the lateral component remains always positive. This is logic if the liquid velocity follows always the liquid spreading from the central part of the jet, pointing outwards. Therefore, the slip-velocity between the phases should always be positive. Indeed, as Figure 4.5 shows, both gas components fall below the liquid velocity. The entrainment part of the jet is carried out by the gas phase, but at a much slower intensity than in a single phase jet. And, as expected, there is no similarity this time on neither of the profiles.

The noise in the profiles, seen as steps far from the centerline, comes from the LDV BP-Filter setting. As the magnitude of the velocity decreases, the BP-Filter is set to a more narrow span, this corresponds to discrete cutout frequencies. This effect makes the jumps from one point to another in the profile, as the configuration is continuously changed to grab the wider possible band.

To highlight the importance of the average liquid/gas slip-velocity $\bar{u}_{i,S}$, a relation extracted

from Chapter 2 is repeated here (see Eq. 2.15 on Page 17). From the development of the Favre averaging process, the Reynolds-averaged phase-velocity fields are related to the turbulent mass flux in the following expression:

$$\bar{u}_{i,S} = \bar{u}_{i,L} - \bar{u}_{i,G} = \frac{\overline{u_i'' Y''}}{\bar{Y}(1 - \bar{Y})}; \quad (4.8)$$

meaning that if a correct estimation of $\bar{u}_{i,S}$ is achieved, the form of the turbulent mass flux $\overline{u_i'' Y''}$ could be deduced. From Eq. 4.8, $\bar{u}_{i,L}$ and $\bar{u}_{i,G}$ refer to the Reynolds averaged fields on the Liquid and Gas phases. However, as discussed before, it is not straightforward to define the average behaviour of the liquid phase as the average from the LDV or DTV data. Therefore, the analysis is presented step-by-step.

A better insight on the liquid velocity behaviour can be seen by looking at the DTV profiles. Despite the lose of spatial precision because of the DOE, as seen before in Chapter 3 (Figure 3.16a on Page 61), the distribution of droplets sizes plays a major role in the reconstruction of the velocity and the Reynolds stresses fields. The influence of the droplet sizes in the calculated averaged values is investigated first.

To mimic the previous Liquid-LDV results, the same profiles are constructed using the method described in Figure 3.20 (Page 67). A first analysis on the influence of the droplet sizes is done by reconstructing the velocity field using Eq. 4.3 (*Average*) and Eq. 4.4 (*d-Average*).

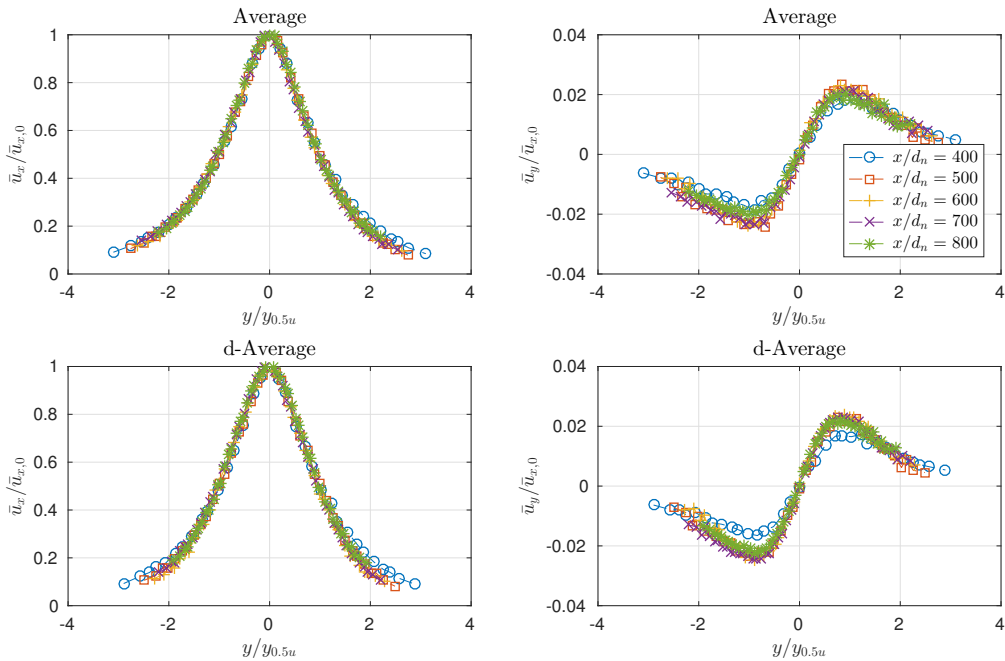


Figure 4.6 – Mean axial and lateral velocities against radial distance. DTV radial profiles from $x/d_n = 400$ to $x/d_n = 800$.

Chapter 4. Results

To check the jet symmetry, the profiles are reconstructed from all the horizontal measurement points. As Figure 4.6 shows, the same similarity on the profiles is achieved, using the two types of averages. $\bar{u}_{x,0}$ and $y_{0.5u}$ are used as normalising parameters, calculated from the DTV profiles. Nevertheless, comparing with the Liquid-LDV, it can be noted that although the similar-profiles keep the same shape, the velocity field obtained by the DTV is not the same.

As mentioned before, there is a difference in the behaviour depending on the class of droplets by diameter. This is investigated by decomposing the averaged velocity field into the classes defined in Table 3.4 (Page 63). Then, the mean velocity is calculated using an arithmetic average of Eq. 4.5.

Using this procedure, Figures 4.7 and 4.8 show the velocity against radial distance profiles, on all the measurement points, in absolute coordinates. The sub-figure analysis on the shadow images, along with a sufficient number of objects detected by class, allow the reconstruction of these detailed profiles.

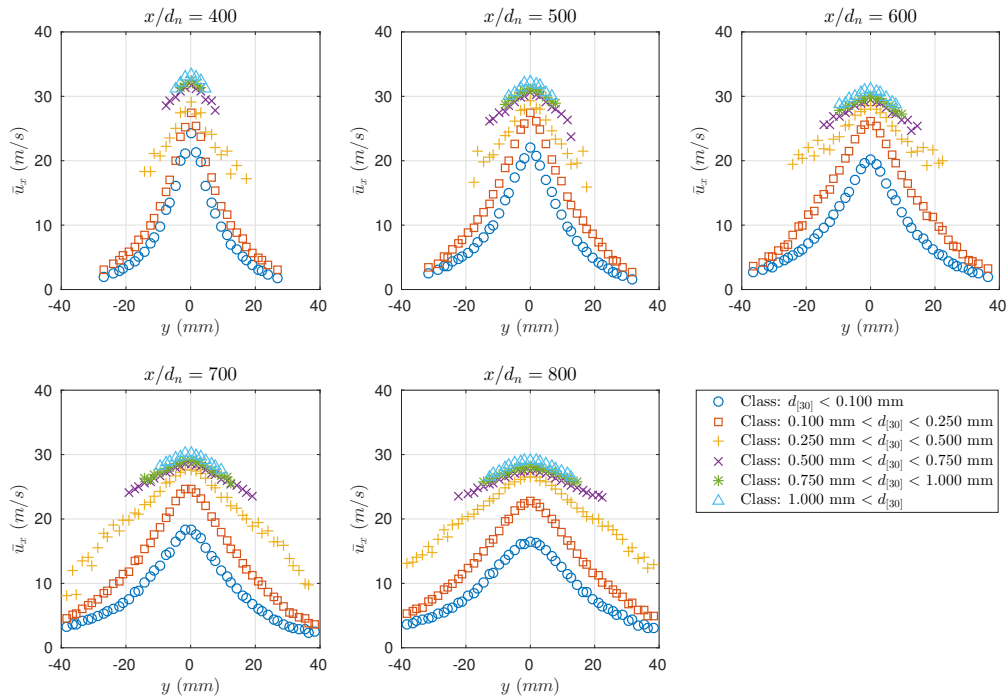


Figure 4.7 – Mean axial velocity by droplet's class diameter against radial distance. DTV Average radial profiles from $x/d_n = 400$ to $x/d_n = 800$.

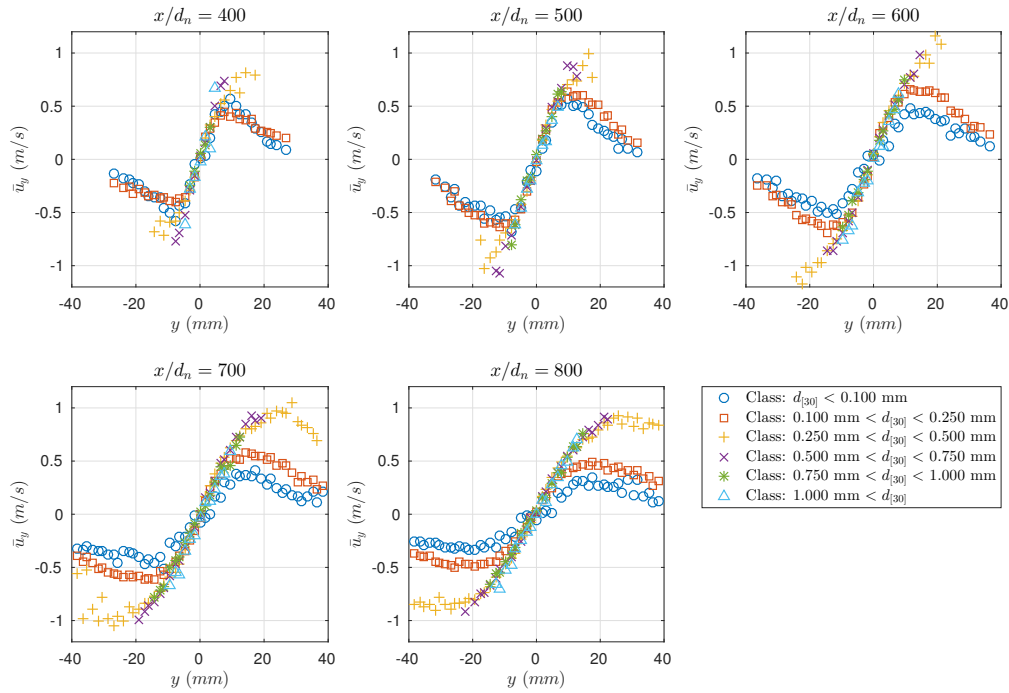


Figure 4.8 – Mean lateral velocity by droplet’s class diameter against radial distance. DTV Average radial profiles from $x/d_n = 400$ to $x/d_n = 800$.

While large droplets tend to maintain the jet average bulk velocity ($\bar{u}_j = 35 \text{ m/s}$) in the axial direction, the small ones lag significantly behind. The lateral velocity shows a similar behaviour, where big droplets tend to escape the central part of the jet, twice as fast as for the smaller class. Despite using a different class partition, the same behaviour can be seen in Stevenin [57] case.

This effect is already observed by Prevost et al. [49] in a particle laden tube jet. When particles come within the same gas jet, their response to the average motion is driven by their capacity to adapt to the gas flow velocity. So, if the longitudinal average gas velocity decreases, it would be harder for large particles to adapt, and their average velocity will be higher.

An analogy to this case can be made. Here, a heavy poly-dispersed flow comes from the nozzle, where droplets meet the gas phase. Dragged by the particles, the gas phase should accelerate until an equilibrium velocity is reached. Small droplets will adapt quicker to this, since they are subjected to bigger aerodynamic effects as a function of the local slip-velocity (velocity seen by the droplets) and their relaxation time τ_R . This effect can be further investigated by examining the Reynolds stresses, which are shown next.

As previously mentioned, the gas phase velocity obtained by LDV is not accurate in zones where a large concentration of liquid droplets is present. Moreover, both LDV and DTV might have biases related to the measurement volume and DOF. Despite these limitations, the LDV data allows to estimate $\bar{u}_{i,L}$, $\bar{u}_{i,G}$ and $\bar{u}_{i,S}$, where the results show a clear mean slip velocity.

From the DTV side, the incertitude introduced by the DOF is tackled with the analysis by class of diameter. This allows to have a clear picture on the average behaviour at different scales, and although it is not explicitly shown here, the relaxation time τ_R must play a significant role, as investigated by Ferrand et al. [21].

4.1.2 Reynolds stresses

The same analysis is performed for the calculation of the Reynolds stresses. Since the main goal is to compare these experimental results with a mixture RANS model, some precisions must be set before.

The numerical mixture RANS model is Favre-averaged, meaning that if a representation from the Reynolds stresses by phase is constructed, the combination yields the following relation:

$$\widetilde{u_i'' u_j''} = \widetilde{Y} \overline{u'_{i,L} u'_{j,L}} + (1 - \widetilde{Y}) \overline{u'_{i,G} u'_{j,G}} + \frac{\widetilde{u_i'' Y''} \widetilde{u_j'' Y''}}{\widetilde{Y}(1 - \widetilde{Y})}; \quad (4.9)$$

where the first two terms are the Reynolds-averaged contributions from the two phases, and the last part is a slip-related component. Actually, using the original relation for the slip-velocity, $\bar{u}_{i,S}$ (Eq. 4.8) into this Eq. 4.9, all contributions to the Favre-averaged Reynolds stresses can be expressed from known experimental quantities:

- $\widetilde{u_i'' u_j''}$: Favre averaged Reynolds stresses (or \widetilde{R}_{ij});
- $\overline{u'_{i,L} u'_{j,L}}$: Liquid Reynolds stresses (or $\bar{R}_{ij,L}$);
- $\overline{u'_{i,G} u'_{j,G}}$: Gas Reynolds stresses (or $\bar{R}_{ij,G}$);
- $\bar{u}_{i,S} \bar{u}_{j,S}$: Slip Reynolds stresses (or $\bar{R}_{ij,S}$).

Rewriting Eq. 4.9 using these terms, gives:

$$\widetilde{R}_{ij} = \widetilde{Y} \bar{R}_{ij,L} + (1 - \widetilde{Y}) \bar{R}_{ij,G} + \widetilde{Y}(1 - \widetilde{Y}) \bar{R}_{ij,S}. \quad (4.10)$$

The overall expression can not be reconstructed, because no experimental results are available to estimate \widetilde{Y} . Nevertheless, the partial contributions are available from the Liquid and Gas LDV measurements, and the subsequent slip-velocity.

The averaging procedure for the Reynolds stresses on each phase is detailed using the LDV data. Using the calculated $\bar{u}_{i,L}$ (Eq. 4.1) and $\bar{u}_{i,G}$ (Eq. 4.2) as center values, the following estimators are constructed for $\bar{R}_{ij,L}$ and $\bar{R}_{ij,G}$:

$$\bar{R}_{ij,L} = \frac{1}{n} \sum_{k=1}^n (u_{i,\{k \in liq\}} - \bar{u}_{i,L})(u_{j,\{k \in liq\}} - \bar{u}_{j,L}); \quad (4.11)$$

$$\bar{R}_{ij,G} = \frac{1}{n} \sum_{k=1}^n (u_{i,\{k \in gas\}} - \bar{u}_{i,G})(u_{j,\{k \in gas\}} - \bar{u}_{j,G}). \quad (4.12)$$

The slip component, $\bar{R}_{ij,S}$ in Eq. 4.10, is reconstructed from the slip-velocity field defined in Eq. 4.8, which yields:

$$\bar{R}_{ij,S} = (\bar{u}_{i,L} - \bar{u}_{i,G})(\bar{u}_{j,L} - \bar{u}_{j,G}) = \bar{u}_{i,S}\bar{u}_{j,S}. \quad (4.13)$$

Using this procedure, $\bar{R}_{ij,L}$, $\bar{R}_{ij,G}$ and $\bar{R}_{ij,S}$ contributions are shown in Figure 4.9 for \bar{R}_{11} , \bar{R}_{22} and \bar{R}_{12} components.

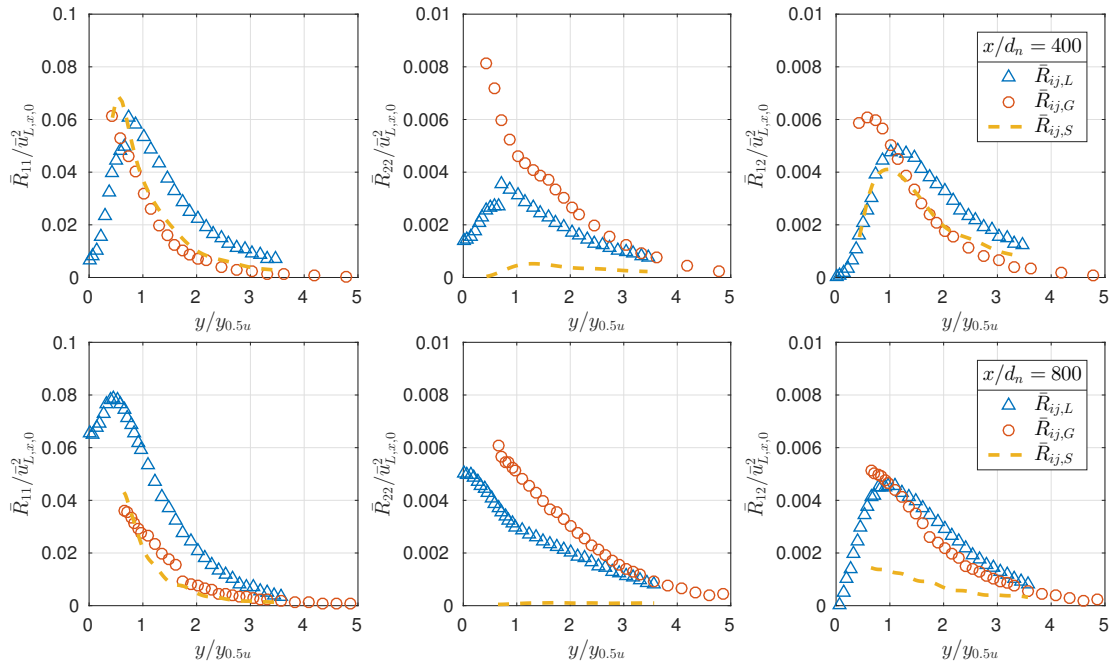


Figure 4.9 – Reynolds stresses against radial distance. LDV liquid, gas and slip components radial profiles at $x/d_n = 400$ and $x/d_n = 800$.

$\bar{u}_{x,L,0}$ and $y_{0.5u}$ are used as normalising parameters. The resulting stresses are presented at $x/d_n = 400$ and $x/d_n = 800$, to see the evolution from the beginning of the dispersed zone up to the last profile acquired.

The $\bar{R}_{11,L}$ component shows a similar behaviour like in a single-phase round jets, reaching its maximum of 0.08 in the dispersed region [30]. The main difference is in the radial component $\bar{R}_{22,L}$, where a huge anisotropy is found, being $\bar{R}_{11,L} \sim 15 \bar{R}_{22,L}$. The shear component $\bar{R}_{12,L}$ is also small, it reaches $\bar{R}_{12}/\bar{k} \approx 1/3$ at the end of the liquid velocity profile, where no more droplets are present. This behaviour differs from the gas-gas variable-density case of Amielh et al. [2] or the gas-gas constant-density of Hussein et al. [30], where the comparison is shown

in Figure 4.10.

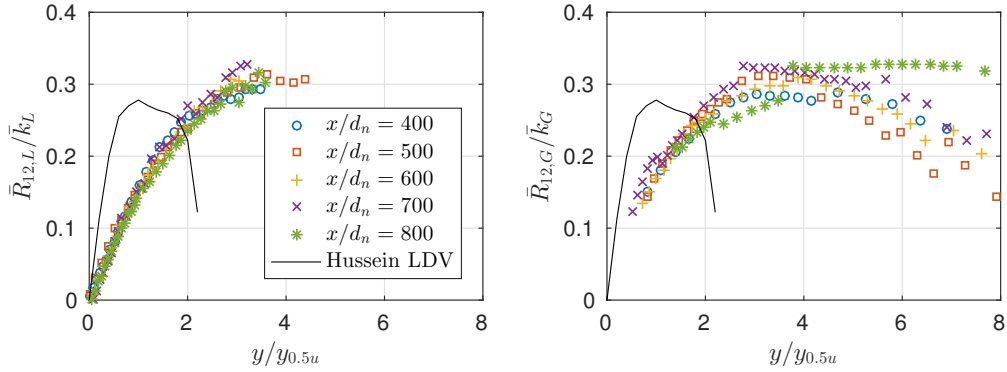


Figure 4.10 – Shear stress over turbulent kinetic energy. LDV liquid and gas components. Radial profiles from $x/d_n = 400$ to $x/d_n = 800$.

Here, \bar{k}_L and \bar{k}_G are calculated assuming a cylindrical axisymmetry, meaning:

$$\bar{k}_L = \frac{1}{2} (\bar{R}_{11,L} + 2\bar{R}_{22,L}); \quad (4.14)$$

$$\bar{k}_G = \frac{1}{2} (\bar{R}_{11,G} + 2\bar{R}_{22,G}). \quad (4.15)$$

Since the shear (R_{12}) and lateral (R_{22}) components are the main dissipation terms in momentum equation, these low values could explain the low decay-rate in the centerline velocity and low spreading-rate. Moreover, it is important to notice that the calculated slip-component $\bar{R}_{ij,S}$ has the same order of magnitude as the liquid and gas parts ($\bar{R}_{ij,L}$ and $\bar{R}_{ij,G}$), meaning that the complete reconstruction based on these three contributions is important to perform a proper comparison with the mixture \tilde{R}_{ij} model.

To characterise the anisotropy of the Reynold stresses, the anisotropy factor is introduced. Since this liquid round jet presents an axisymmetric behaviour, where $\tilde{R}_{11} \gg \tilde{R}_{22} = \tilde{R}_{33}$, the anisotropy factor $\langle A \rangle_R$ is defined as:

$$\langle A \rangle_R = \frac{\langle R \rangle_{22}}{\langle R \rangle_{11}}. \quad (4.16)$$

Therefore, a low anisotropy factor means a high anisotropy $A_R \ll 1.0$, and a value close to $A_R = 1.0$ means an isotropic behaviour.

From the observations made by Stevenin [57], if the Stokes number (St) calculated for the liquid droplets is small enough, a high anisotropy could be a consequence of the sharp gas boundary layer created around the poorly atomised liquid jet. However, by looking at the gas phase Reynolds stresses here, it seems to be the other way around. Indeed, the gas phase data

presents a lower anisotropy than the liquid phase, meaning that it is the liquid phase which generates this behaviour.

To investigate further on the source, the DTV data is used. Since the strong anisotropy and low shear components seem to be maintained throughout the whole dispersed domain, an analysis at $x/d_n = 800$ is presented. The joint *pdfs* between the velocity components and the droplet's diameters are shown in Figure 4.11 at several radial distances from the centerline, where using the sub-image partition, the *pdfs* are constructed by picking the central slices on each value.

To compare using the whole database, Liquid and Gas LDV are shown on nearly the same measurement points. The first row corresponds to the LDV Gas (not available at the centerline); the second row is the LDV Liquid; and the rest are from DTV, decomposed as the *pdfs* by velocity component as a function of the droplet equivalent diameter ($d_{[30]}$). It is clear that the local dispersion by class of diameters behaves in a very different way on both axes, this is confirmed by looking at the same *pdf* shape from the LDV campaign.

The change in the fluctuating behaviour for both velocity components can be seen at the same time in the Liquid and Gas phases. As the distance from the centerline increases, a tendency to a more isotropic behaviour can be seen in both the liquid and the gas. By looking at the decomposition by droplet diameter, it seems that the presence of big droplets close to the centerline generates a long spectrum of variation for the axial velocities, whereas a less intense effect is seen in the lateral component.

From this, the Reynolds stresses are obtained using the same averaging procedure used for the mean velocity estimation: thus, a simple average and a diameter-weighted average. \bar{R}_{ij} flagged as *Average*, using \bar{u}_i as a centre value from Eq. 4.3, is simply:

$$\bar{R}_{ij} = \frac{1}{n} \sum_{l=1}^n (u_{i,l} - \bar{u}_i)(u_{j,l} - \bar{u}_j); \quad (4.17)$$

and *d-Average* is calculated as a weighted average by the droplet $d_{[30]}$ diameter, using \bar{u}_i from Eq. 4.4, meaning:

$$\bar{R}_{ij} = \frac{\sum_{l=1}^n d_{[30],l} (u_{i,l} - \bar{u}_i)(u_{j,l} - \bar{u}_j)}{\sum_{l=1}^n d_{[30],l}}. \quad (4.18)$$

The results are shown in Figure 4.12, where the same similitude representation appears using the calculated $\bar{u}_{x,0}$ and $y_{0.5u}$ as normalisation parameters, from the corresponding velocity fields. Once more, no matter the type of average, the profiles fit well a similar relation. Moreover, the profiles show the same behaviour as those previously obtained by LDV. However, as expected, the diameter-weighted average produces an impact on the results. As the previous *pdfs* show in Figure 4.11, large droplets present little agitation compared to the smaller ones. This effect is studied by reconstructing the Reynolds stresses by class of diameter. The averaging procedure is a simple arithmetic average inside the class (k), meaning that the

Chapter 4. Results

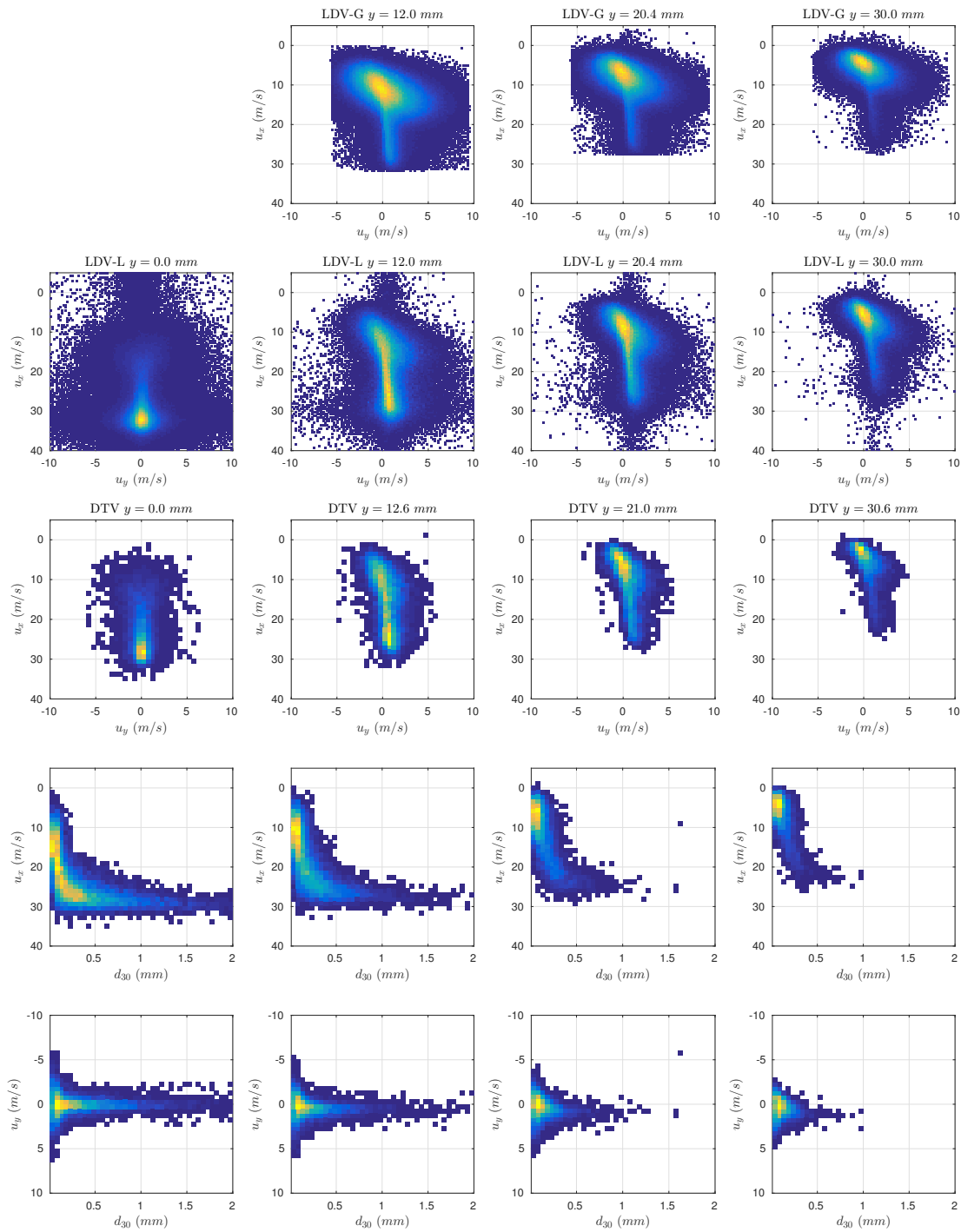


Figure 4.11 – Bi-variate histograms normalised as a *pdf* from LDV and DTV, at $x/d_n = 800$ for: u_x - u_y , u_x - $d_{[30]}$ and u_y - $d_{[30]}$.

4.1. Experimental observations

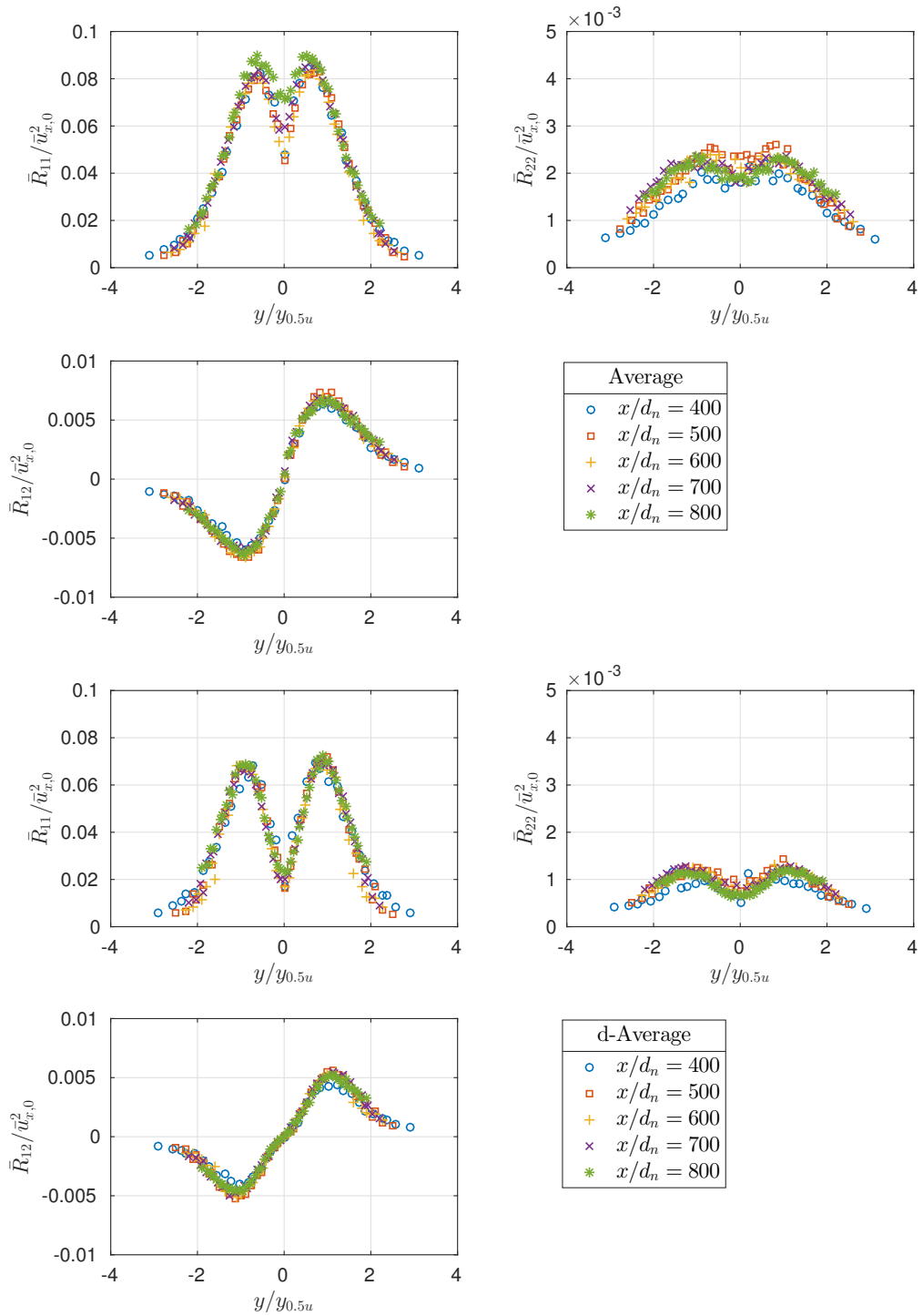


Figure 4.12 – Reynolds stresses against radial distance. DTV Average and d-Average radial profiles from $x/d_n = 400$ to $x/d_n = 800$.

Chapter 4. Results

values are centred using $\bar{u}_{i,(k)}$ (Eq. 4.5):

$$\bar{R}_{ij,(k)} = \frac{1}{n} \sum_{l=1}^n (u_{i,\{l \in (k)\}} - \bar{u}_{i,(k)}) (u_{j,\{l \in (k)\}} - \bar{u}_{j,(k)}); \quad (4.19)$$

and shown in Figure 4.13. Since, $\bar{u}_{x,0}$ and $y_{0.5u}$ are not defined by class of diameter, the Reynolds stresses are presented in absolute values, at $x/d_n = 400$ and $x/d_n = 800$.

A clear different behaviour can be observed from the analysis by class of diameter. The shear and transverse components seem to be more important for very small diameter droplets, following the gas phase turbulence (see Figure 4.9). This is consistent with the observations made by Ferrand et al. [21] in a particle-laden jet, who explains this behaviour using the calculated Stokes number (St) by class of diameter.

Finally, using these values for the reconstructed \bar{R}_{ij} , the anisotropy factor $\bar{R}_{22,(k)}/\bar{R}_{11,(k)}$ by class is constructed and presented in Figure 4.14.

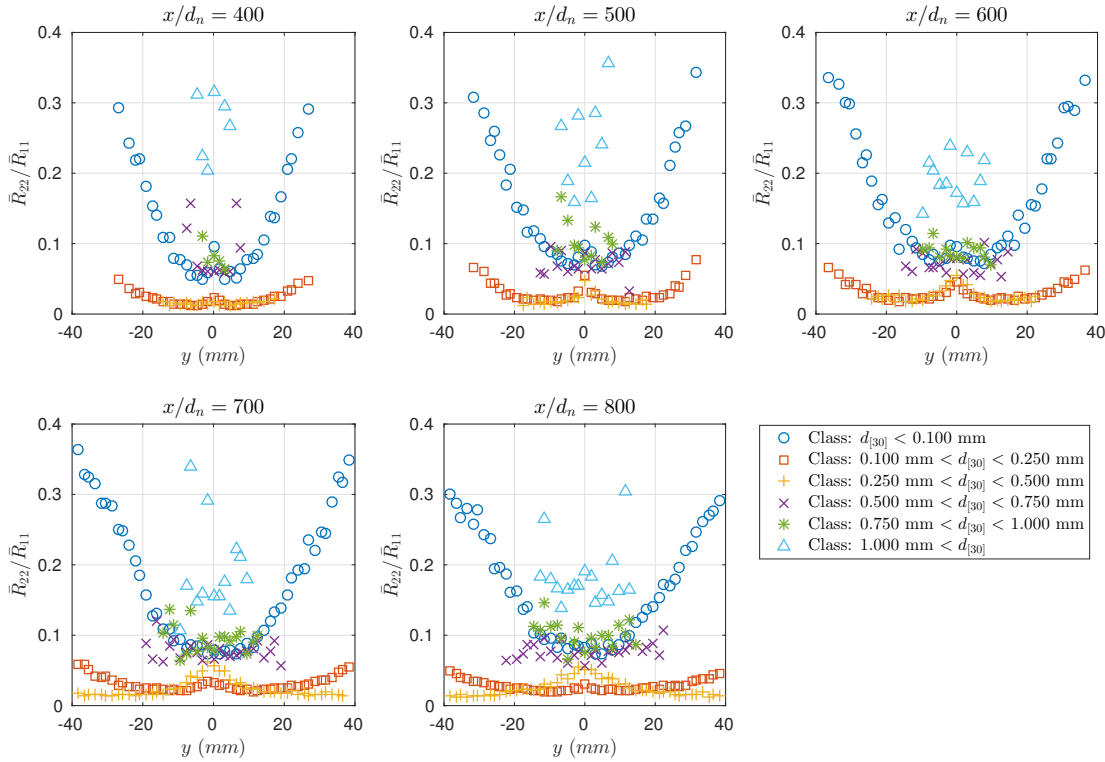


Figure 4.14 – Reynolds stresses anisotropy factor ($\bar{R}_{22}/\bar{R}_{11}$) against radial distance. DTV radial profiles by droplets' class diameters from $x/d_n = 400$ to $x/d_n = 800$.

These results clearly differs from the gas-gas jet of Hussein et al. [30] or the particle-laden jet of Ferrand et al. [21], where a high anisotropy is found on the bigger class of particles ($d_p = 80 - 90 \mu\text{m}$). Here, the anisotropy seems to reach its maximum in the $100 \mu\text{m} < d_{[30]} \leq 250 \mu\text{m}$ and $250 \mu\text{m} < d_{[30]} \leq 500 \mu\text{m}$ class, at the more fragmented part of the jet. In contrast, very

4.1. Experimental observations

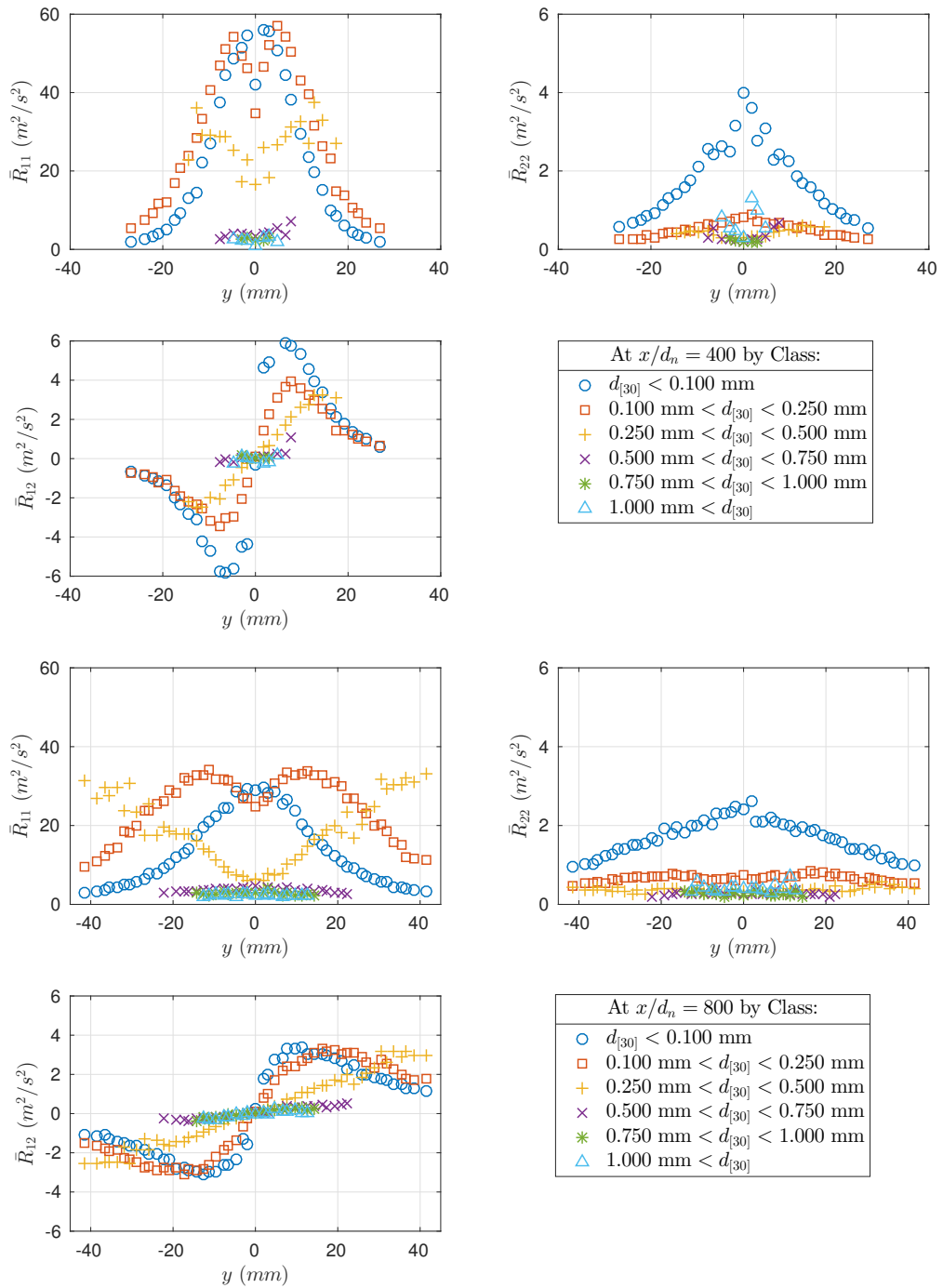


Figure 4.13 – Reynolds stresses against radial distance. DTV radial profiles by droplets' class diameters for $x/d_n = 400$ and $x/d_n = 800$.

Chapter 4. Results

large and small droplets are more isotropic. As enunciated before, very small droplets could be more prone to be affected by the gas phase turbulence, therefore they will tend to isotropy at the external zones. This is also implicitly shown in Figure 4.11, where the combined effect can be seen by reconstructing the *pdfs* at several distances from the centerline.

As mentioned before, an estimation of the Stokes Number (St) could give a better insight on this behaviour. From the acquired data, the following formulation by class of diameter (k) could be used:

$$St_{(k)} = \frac{\tau_R}{\tau_t} = \frac{\frac{\rho_L \bar{d}_{[30],(k)}^2}{18\mu_G(1+0.15Re_{d,(k)}^{0.687})}}{\frac{y_{0.5u}}{\sqrt{\bar{R}_{11,G}}}}; \quad (4.20)$$

τ_t is estimated using the length scale $y_{0.5u}$ and axial standard deviation for the velocity fluctuations in the gas phase $\sqrt{\bar{R}_{11,G}}$. $Re_{d,(k)}$ is the Reynolds number seen by the droplets of the class (k):

$$Re_{d,(k)} = \frac{\|\bar{u}_{i,(k)} - \bar{u}_{i,G}\| \bar{d}_{[30],(k)}}{v_G}. \quad (4.21)$$

Here, to represent the velocity seen by the droplets, the mean gas velocity $\bar{u}_{i,G}$ is extracted from the LDV data, and $\bar{u}_{i,(k)}$ is the mean velocity of the class (k) from the DTV, with the corresponding mean diameter $\bar{d}_{[30],(k)}$. This formulation differs from the one in Eq. 2.41 (page 25) in the sense that it confronts directly the mean slip velocity by class of diameters against the gas velocity field, whereas the modelled quantity needs the drift part $\bar{u}_{i,D}$ (Eq. 2.42) to account for the slip velocity *seen* by the droplets.

Because the mean and fluctuating data is not available at the centerline of the jet, a special class of $\bar{d}_{[30],(k)} \leq 50\mu m$ is created to represent $\sqrt{\bar{R}_{11,G}}$. This is, however, a very strong hypothesis, because as Figure 4.15 shows at $x/d_n = 800$, despite the similitude far from the centerline of these two quantities, closer to the axis there is no evidence that small droplets ($\bar{d}_{[30],(k)} \leq 50\mu m$) follow the gas-phase fluctuations.

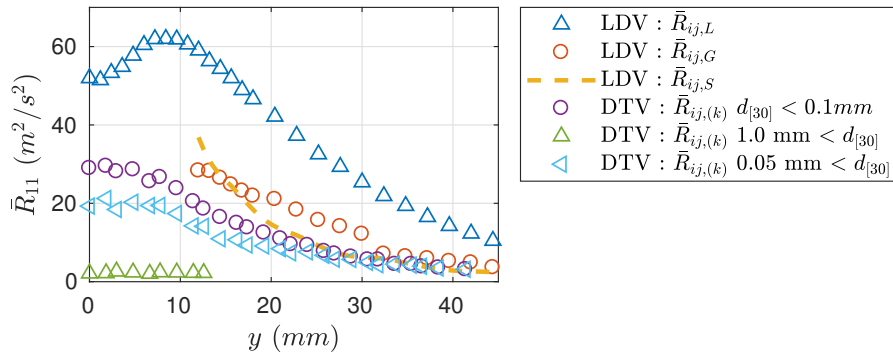


Figure 4.15 – Reynolds stresses against radial distance. DTV and LDV radial profiles at $x/d_n = 800$.

4.1. Experimental observations

Using these results, the Stokes number St from Eq. 4.20 is calculated along the centerline of the jet in Figure 4.16. It shows how the particles should react to this gas fluctuating field $\bar{R}_{11,G}$. Here, if $St \gg 1$, the droplets are unresponsive to the gas phase fluctuations, and if $St \ll 1$, they should follow the gas phase as tracers.

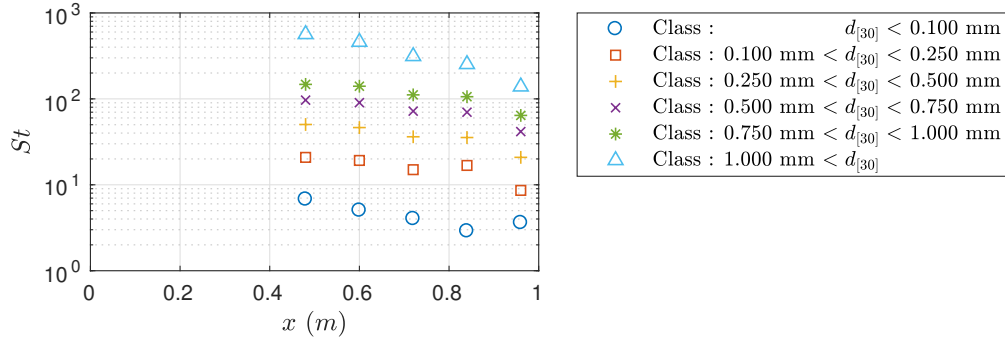


Figure 4.16 – Stokes number at the jet centerline by droplets' class of diameters from $x/d_n = 400$ to $x/d_n = 800$.

Despite this strong hypothesis, a clear difference on the behaviour by class of diameter can be seen. Although the small droplets never reach $St \ll 1$, and therefore, they should not be considered as gas tracers, they are order of magnitudes more responsive to the gas phase fluctuations than the bigger ones.

This effect could explain the strong anisotropy factor found in the medium sized droplets (see Figure 4.14). Large droplets are the least influenced by the gas phase fluctuations, they tend to keep a velocity close to the injection bulk velocity $\bar{u}_J = 35 \text{ m/s}$, with a turbulent intensity inherited from the pure liquid-phase (see Figure 4.13). Small droplets follow the gas-phase fluctuations easily far from the centerline, but they are trapped by the large slip-velocity induced by large droplets close to the axis. However, medium sizes droplets ($100 \leq \bar{d}_{[30],(k)} \leq 500 \mu\text{m}$), can have both a wide band of turbulent intensity and be less influenced by the gas phase fluctuations far from the centerline, boosting the anisotropy on the whole profile as seen in Figure 4.14.

4.2 Numerical model analysis

The numerical model analysis follows the previous cases definition in Chapter 2. The main objective at first is to test the behaviour of several variations of the RANS turbulence models. Later, based on the experimental observations, some specific cases are presented to account for these observations.

The detailed description of the modelled equations is given in Chapter 2.2. However, to better illustrate the analysis, some equations are rewritten here along with the study case definition. A quick description of the simulation case is shown in Figure 4.17. This represents a schematic view of a longitudinal 2D slice (the real case is 3D).

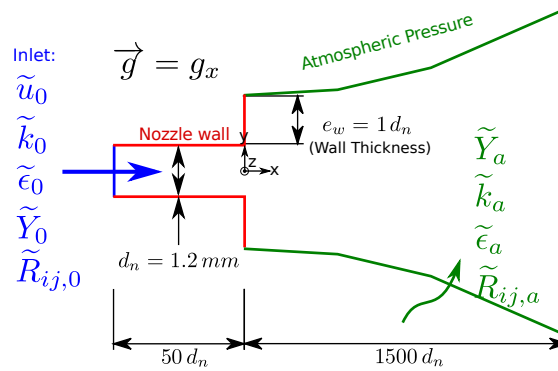


Figure 4.17 – Schematic representation of the 3D mesh, including boundary conditions.

From this, the boundary conditions and case set-up are:

- The nozzle diameter is $d_n = 1.2 \text{ mm}$, of length $L_n = 50d_n$ and pointing downwards, aligned with gravity.
- Only water is injected through the nozzle, meaning that $\tilde{u}_0 = \bar{u}_{L,J} = 35 \text{ m/s}$ and $\tilde{Y}_0 = \bar{Y}_0 = 1$. The air is considered still.
- Turbulence boundary conditions are specified as if there is an infinite, similar, pipe flow upstream, with a turbulence intensity $I_t = 4\%$. This yields a $\tilde{k}_0 = 3.3 \text{ m}^2/\text{s}^2$ and $\tilde{\epsilon}_0 = 11700 \text{ m}^2/\text{s}^3$. The Reynolds stresses are considered isotropic, so $\tilde{R}_{ij,0} = 2/3\tilde{k}_0\delta_{ij} \text{ m}^2/\text{s}^2$.
- The simulation time is from $t_0 = 0 \text{ s}$ to $t_f = 0.3 \text{ s}$. This ensures a full coverage of the domain, even in the external regions of the jet. The time-step of the simulation is variable, calculated from the worst case as a function of the local Courant number Co . To avoid any divergence of the simulation, $Co = 0.8$ is set as the maximum possible value.

4.2.1 RANS turbulence model

First, a variation of the RANS turbulence model is analysed. The three previously described turbulence models are used: $k - \epsilon$ (k-Epsilon), $R_{ij} - \epsilon$ (RSM) and $R_{ij} - \epsilon_{ij}$ (RSM Variation). To isolate the behaviour only as a function of the turbulence modelling, the same basic turbulent mass flux model is used, Y_{mod0} . All of this corresponds to the cases: *Case 112*, *Case 212* and *Case 312* (Page 37).

A first comparison with the experimental results is shown in Figure 4.18. The centerline evolution of the axial mixture velocity ($\tilde{u}_{x,0}$) is presented along the centerline liquid velocity ($\bar{u}_{x,L,0}$) from the LDV (Figure 4.18-(a)). Evidently, despite that the comparison of mixture against liquid velocities might be inconsistent, at the centerline $\tilde{Y} \approx 1.0$, which makes $\tilde{u}_{x,0} \approx \bar{u}_{x,L,0}$. Based on the lateral profiles, the calculated half-width of the velocity profiles is

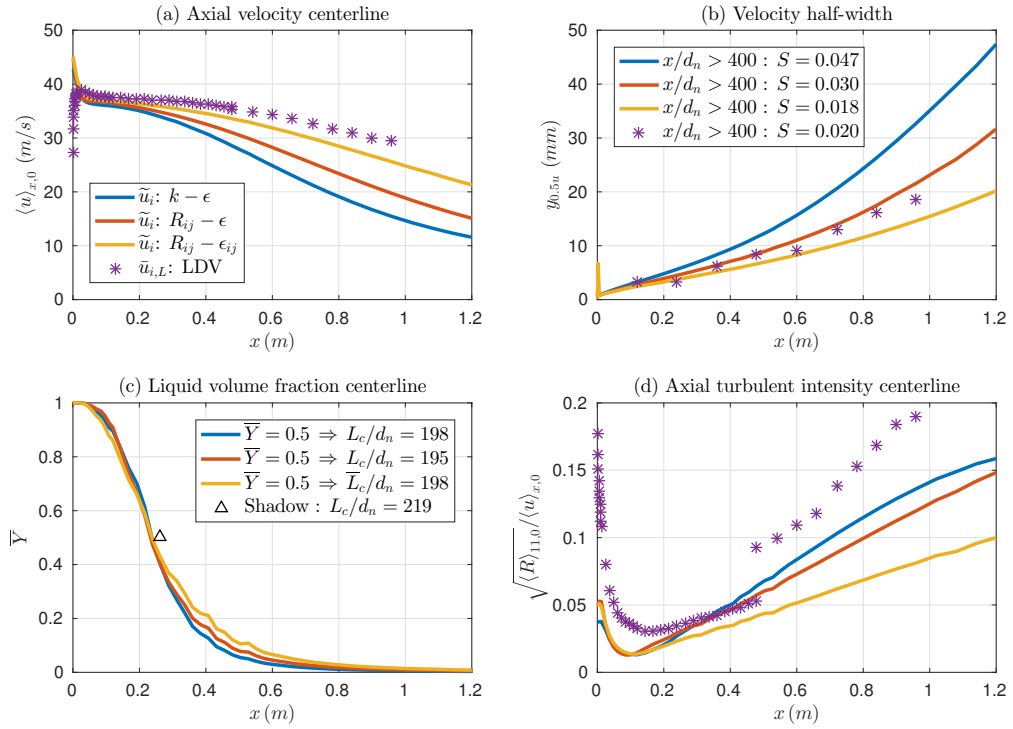


Figure 4.18 – Turbulence models' benchmark compared to the Liquid LDV.

compared ($y_{0.5u}$) with experimental reconstruction from the LDV $\tilde{u}_{x,L}$ profiles (Figure 4.18-(b)). As discussed later, the half-width is defined for the mixture velocity, so a combination between $\tilde{u}_{x,L}$ and $\tilde{u}_{x,G}$ should be used instead. However, as \tilde{Y} is not directly measured, \tilde{u}_x remains unknown.

The centerline liquid volume fraction is compared to the estimated average liquid column breakup length, where $\bar{Y} \approx 0.5$ (Figure 4.18-(c)). This is a rough estimation of the behaviour of the solution, because this hypothesis to separate the dense zone from the dispersed part of the spray is not always well defined.

Chapter 4. Results

Finally, the comparison for the axial turbulent intensity $\sqrt{\langle R \rangle_{11,0}} / \langle u \rangle_{x,0}$ is shown in Figure 4.18-(d). Contrary to the mean values, the choice of parameters on the LDV set-up seems to have a big impact on the calculated fluctuating quantities. Indeed, at $x/d = 400$, a change in the PM sensitivity is made, resulting in a jump of the calculated turbulent intensity. To avoid damaging the PMs, from $x/d = 0$ to $x/d = 400$ the gain can not be set to a higher value, resulting in a biased fluctuating field, as the system is unable to capture small droplets events.

The first observation that can be made is about the momentum diffusion comparison between the three model approaches. As expected, the introduction of a RANS model that takes into account some anisotropy on the Reynolds stresses plays a significant role in the overall results. As Figure 4.18 shows, the $R_{ij} - \epsilon_{ij}$ simulation case presents a small decay-rate of the axial centerline velocity $\tilde{u}_{x,0}$, bringing the results closer to the experimental points. The explanation on the mechanism of these results is explained later using the Reynolds stresses fields.

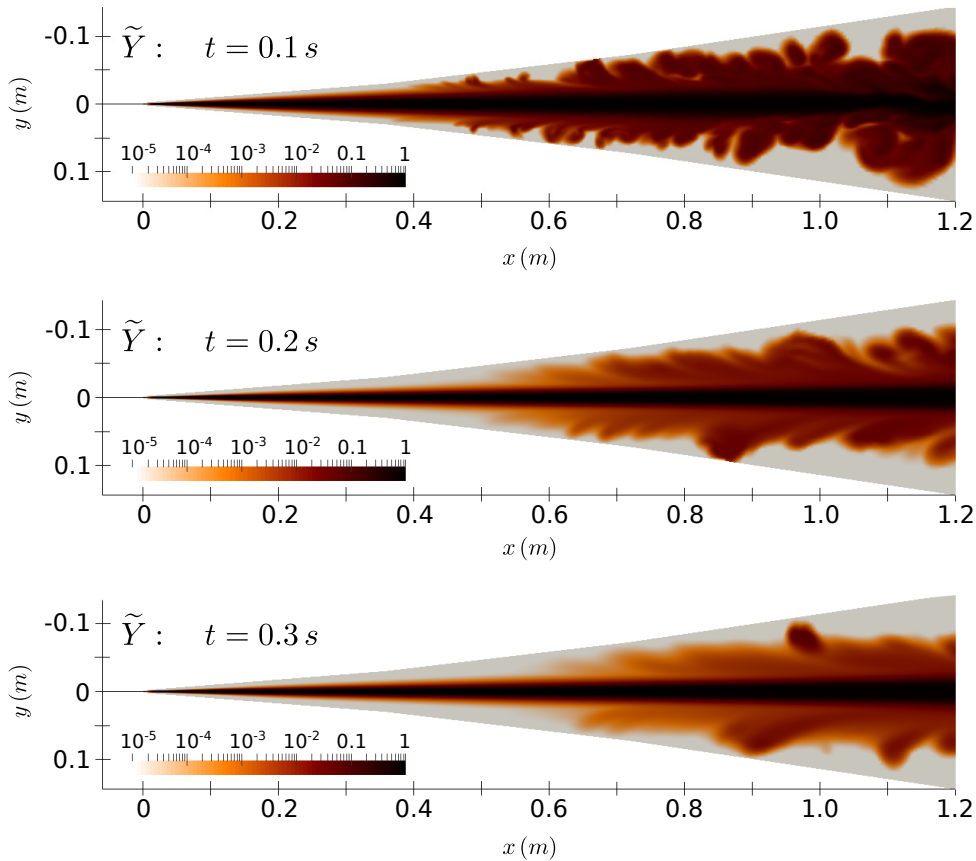


Figure 4.19 – Liquid mass fraction \tilde{Y} field in a mid-plane ($z = 0$) cutout. Solution from $t = 0.1$ s to $t = 0.3$ s.

Because of the U-RANS formulation, and since the solution is taken at a given time, $t = 0.3$ s, it can be seen in Figure 4.18-(c) that there is a residual unsteadiness of the solution. Indeed,

\tilde{Y} fluctuates as function of time (therefore, \bar{Y} does too). This is not due to some lack of convergence, because the solver converges at every time-step by definition. In fact, these fluctuations may be a product of the actual jet flapping, like in the work made by Delon [13]. Nevertheless, these fluctuations are not considered to be high enough to affect the analysis made here, and the unsteadiness is not taken into account in this analysis. To illustrate this, a complete solution in a mid-plane cutout of the simulated domain is shown in Figure 4.19 for the $R_{ij} - \epsilon_{ij}$ case.

Before going into the comparative analysis, a precision on the use of the turbulent mass flux model needs to be made. This argument is carried out throughout the whole analysis. Indeed, Y_{mod0} reads (from Eq. 2.37):

$$-\bar{\rho} \widetilde{u_i'' Y''} = \frac{\mu_t}{\sigma_Y} \frac{\partial \tilde{Y}}{\partial x_i}. \quad (4.22)$$

From the model used by Belhadeef et al. [5], and the later analysis made by Stevenin et al. [59], the use of a turbulent Schmidt number of $\sigma_Y = 5.5$ is used and justified. Not only because it fits well the experimental results on a similar round jet, but because it emulates a strong anisotropy factor in the principal Reynolds stresses, starting from a more general formulation, meaning that if a boundary layer approximation is made, then:

$$-\bar{\rho} \widetilde{u_i'' Y''} \approx \bar{\rho} \widetilde{u_y'' Y''} = C_Y \bar{\rho} \frac{\tilde{k}}{\tilde{\epsilon}} \widetilde{u_y''^2} \frac{\partial \tilde{Y}}{\partial y}; \quad (4.23)$$

and assuming that $\widetilde{u_y''^2} = 0.082 \tilde{k}$, then using the standard value of $C_Y = 0.1$, Y_{mod1} becomes Y_{mod0} with $\sigma_Y = 5.5$.

If a RSM case would produce a strong anisotropy, like in the one observed in Figure 4.14, this artificial $\sigma_Y = 5.5$ would not be necessary. However, this is not the case for the two RSM formulations used here. The anisotropy factor reaches nearly $\tilde{R}_{22} / \tilde{R}_{11} = 0.6$ and together with a high enough shear component $\tilde{R}_{12} \sim \tilde{k}/3$, Y_{mod1} becomes Y_{mod0} .

Good enough RSM and turbulent mass flux formulations would produce both a strong anisotropy factor and a low shear component. This would produce at the same time a low decay rate of the centerline axial velocity and a low spreading rate, as experimentally found (see Figures 4.1, 4.9 and 4.14).

Having set the same turbulent mass flux model, as previously shown, how the Reynolds stresses are calculated seems to have a huge effect on the velocity field. This is explicitly shown in Figure 4.20, where the Reynolds stresses are compared in the dispersed zone of the jet.

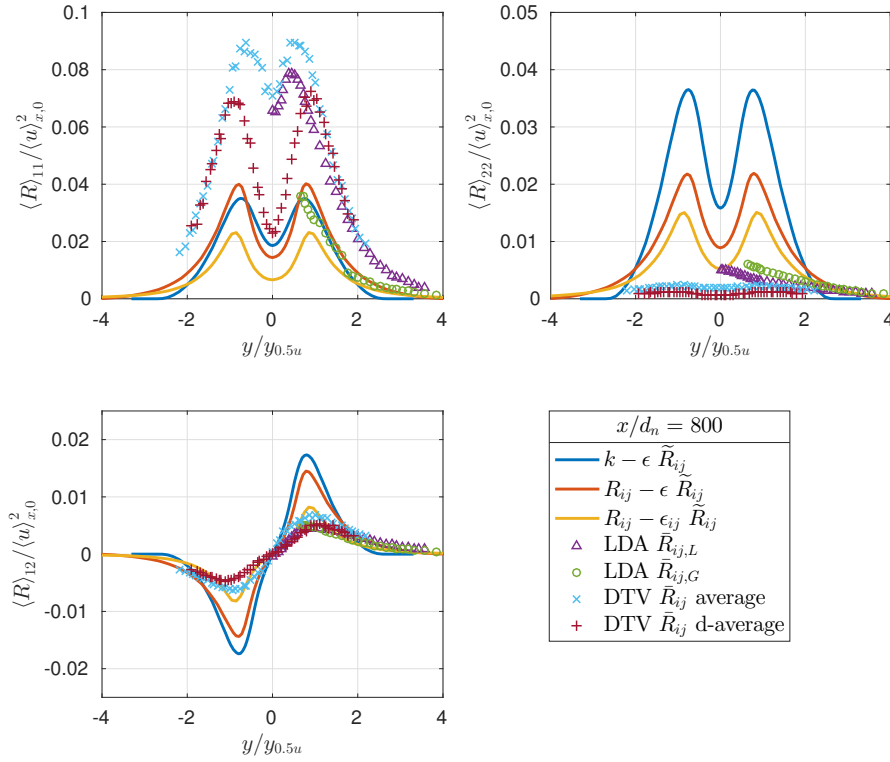


Figure 4.20 – Comparison of the Reynolds stresses against radial distance as a function of the turbulence model at $x/d_n = 800$. Experimental LDV (liquid and gas) and DTV radial profiles are shown as a benchmark.

Indeed, while both the simulation and the experimental case produce nearly the same turbulent kinetic energy, which for a cylindrical axisymmetry is:

$$\langle k \rangle = \frac{1}{2} (\langle R \rangle_{11} + \langle R \rangle_{22} + \langle R \rangle_{33}) \approx \frac{1}{2} (\langle R \rangle_{11} + 2\langle R \rangle_{22}); \quad (4.24)$$

the distribution between the principal components is completely different. Indeed, $\langle R \rangle_{11}$ component has a similar value compared to Hussein et al. [30] or Amielh et al. [2] cases, while $\langle R \rangle_{22}$ simulation results does not seem to approach the very low experimental values.

Despite all this, since $\langle R \rangle_{12}$ is indeed lower in the $R_{ij} - \epsilon_{ij}$ case, this results in a low momentum transfer from the axial to the radial direction, decreasing the decay rate of the axial centerline velocity. A good numerical result would be to reduce considerably $\langle R \rangle_{22}$ and $\langle R \rangle_{12}$, while keeping a high enough $\langle R \rangle_{11}$.

Although these comparisons are made between the Liquid/Gas Reynolds-averaged values, against the Favre-averaged model, the orders of magnitude and the relation given by Eq. 4.10 point in a clear direction.

4.2.2 Epsilon equation behaviour

Before examining further the last point, a brief analysis on the use of the Epsilon equation is developed. The three RANS models used here rely on the same modelled Epsilon equation (Eq. 2.22) to obtain the turbulent kinetic energy dissipation rate $\tilde{\epsilon}$.

Many versions of this modelled equation exist in different applications of RANS turbulence. A particular variation to the original version by Jones and Launder [34] is introduced by Pope [46]. The original version gives good results in a planar-jet configuration, but if the same parameters are used in a round-jet, the spreading rate S is overestimated. This is called the round-jet/planar-jet anomaly, it is related to the vortex stretching in the angular direction of a round-jet. Pope [46] proposes to add an extra source term to account for this, resulting in good agreement with experimental results.

Dally et al. [9] proposes to use the original equation proposed by Jones and Launder [34], but with $C_{\epsilon 1} = 1.60$ instead of the original $C_{\epsilon 1} = 1.44$ value. The overall increase of the production term would produce a similar effect to correct the spreading rate in a round-jet. The analysis on the application of this modification to a circular multiphase jet is also studied by Stevenin et al. [59], improving the numerical results on the spreading rate prediction.

To test this behaviour, the contributions at the *RHS* of the Epsilon equation are studied by modifying the value of $C_{\epsilon 1}$. The study cases are based on the $R_{ij} - \epsilon$ model with Y_{mod0} : *Case 211* and *Case 212* (see page 38). In Figure 4.21 the following budget is shown for the two cases at $x/d_n = 400$ in a radial profile:

- **Production-1:** with $C_{\epsilon 1} = 1.44$ or $C_{\epsilon 1} = 1.60$;

$$-C_{\epsilon 1} \frac{\tilde{\epsilon}}{k} \overline{\rho u_i'' u_j''} \frac{\partial \tilde{u}_i}{\partial x_j}. \quad (4.25)$$

- **Production-2:** with $C_{\epsilon 4} = 1.0$;

$$-C_{\epsilon 4} \frac{\tilde{\epsilon}}{k} \overline{u_i''} \frac{\partial \bar{p}}{\partial x_i}. \quad (4.26)$$

- **Destruction:** with $C_{\epsilon 2} = 1.92$

$$-C_{\epsilon 2} \bar{\rho} \frac{\tilde{\epsilon}^2}{k}. \quad (4.27)$$

- **Dilatation:** with $C_{\epsilon 5} = 1.0$

$$-C_{\epsilon 5} \bar{\rho} \tilde{\epsilon} \frac{\partial \tilde{u}_k}{\partial x_k}. \quad (4.28)$$

Chapter 4. Results

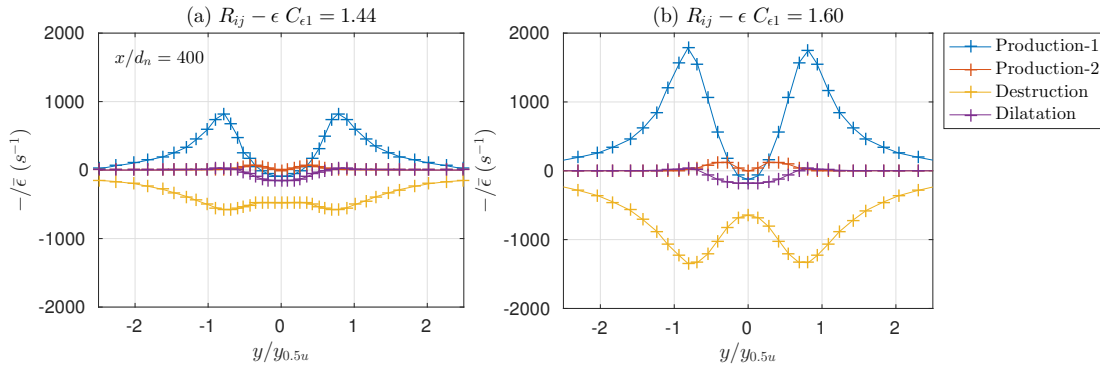


Figure 4.21 – Epsilon equation budget against radial distance for two cases: (a) $R_{ij} - \epsilon$ with $C_{\epsilon 1} = 1.44$ (Standard value); (b) $R_{ij} - \epsilon$ with $C_{\epsilon 1} = 1.60$ (round-jet correction). Radial profiles at $x/d_n = 400$.

The profiles are divided by $\bar{\rho}\tilde{\epsilon}$ to account for the relative variation. Cell centre values are also shown to highlight the mesh quality. Indeed, the original production term (*Production-1*) is higher using $C_{\epsilon 1} = 1.60$, creating a higher $\tilde{\epsilon}$, lowering the turbulent kinetic energy \tilde{k} in zones with high shear.

To check if this effect is also important using the $R_{ij} - \epsilon_{ij}$ model with Y_{mod0} , cases *Case 311* and *Case 312* (see page 38) are also created. The overall influence is shown in Figure 4.22, where the axial velocity profiles for all four numerical models are compared against the experimental results.

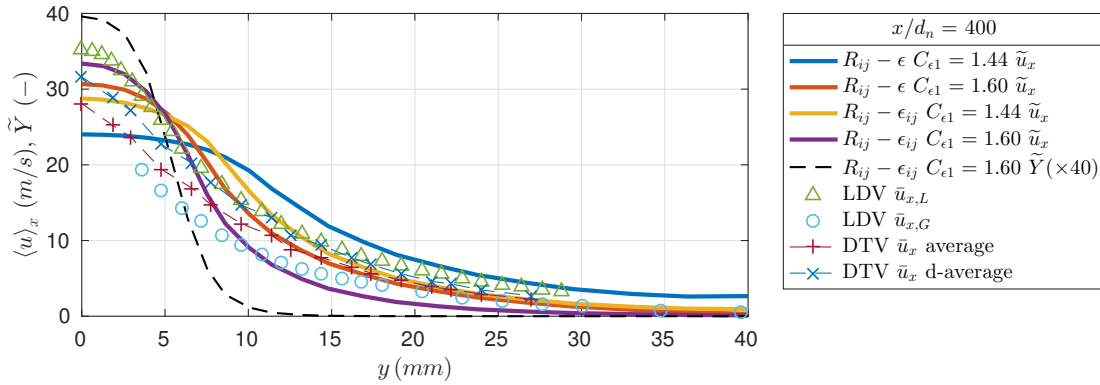


Figure 4.22 – Mean axial velocity against radial distance as a function of $C_{\epsilon 1}$ at $x/d_n = 400$. Experimental LDV (liquid and gas) and DTV radial profiles are shown as a benchmark.

As previously shown before, the $R_{ij} - \epsilon_{ij}$ model with Y_{mod0} predicts not only a better centerline velocity but at the same time a good spreading rate. From Figure 4.18 (page 89) it might seem that the spreading rate S is underestimated, but looking at the actual radial profiles, \tilde{u}_x should blend from $\tilde{u}_{x,L}$ to $\tilde{u}_{x,G}$ as a function of the radial distance, following the liquid mass fraction \tilde{Y} radial profile. This last quantity is however not available from the experimental measurements,

but the numerical solution is shown to illustrate the effect.

4.2.3 Turbulent mass transport

The previous two analyses are centred on the use of an RSM case, coupled with a basic description for the turbulent mass fluxes (Y_{mod0}). Now, the focus is on this last quantity. Using several numerical study cases, a comparison between the experimental results against the numerical solution is made, as a function of several formulations for $\widetilde{u_i'' Y''}$.

Both Y_{mod0} and Y_{mod1} are based in the same gradient diffusion hypothesis (Eq. 2.37 and 2.38, on Page 23). However, as experimentally observed, the mean slip-velocity between the liquid and gas phases (Eq. 4.8) does not agree with this gradient hypothesis formulation. Indeed, if $\bar{u}_{x,S} \gg \bar{u}_{y,S}$, and $\frac{\partial \tilde{Y}}{\partial x} \ll \frac{\partial \tilde{Y}}{\partial y}$, then $\widetilde{u_i'' Y''} \ll \frac{\partial \tilde{Y}}{\partial x_i}$.

Throughout the whole set of simulation cases, the second order modelled equation for $\widetilde{u_i'' Y''}$ is solved, but not coupled (Eq. 2.39) with the actual mass transport Eq. 2.10. This is done to have an estimation on how a solution to this equation would behave, without the complications of a full coupling, which is analysed later.

From the experimental results, it can be seen that generally $\widetilde{u'' Y''} \gg \widetilde{v'' Y''}$. Therefore, the solution for the second order modelling of $\widetilde{u_i'' Y''}$ should produce something like this. An analysis of the source terms at the *RHS* of Eq. 2.39 gives an insight on how the solution may react as a function of a subset of modelled parameters. Indeed, if the system is in equilibrium and the source and sink terms are dominant, then:

$$\widetilde{u_i'' Y''} = \tilde{F}_{i,D} - \frac{C_{F2}}{C_{F4}} (1 - \tilde{Y}) \tau_R \widetilde{u_i'' u_j''} \frac{\partial \tilde{Y}}{\partial x_j} - \frac{C_{F1}}{C_{F4}} (1 - \tilde{Y}) \tau_R \widetilde{u_j'' Y''} \frac{\partial \tilde{u}_i}{\partial x_j} - \frac{C_{F3}}{C_{F4}} (1 - \tilde{Y}) \tau_R \frac{\tilde{Y}''}{\bar{\rho}} \frac{\partial \bar{p}}{\partial x_i}; \quad (4.29)$$

where $\tilde{F}_{i,D}$ is the modelled drift velocity, simply expressed as Y_{mod0} . From this, an approximation can be made, where $\frac{\partial}{\partial y} \gg \frac{\partial}{\partial x}$ and the pressure-gradient term is neglected, by simply making $C_{F3} = 0$. Then, the axial and lateral components are:

$$\widetilde{u_x'' Y''} = -\frac{C_{F2}}{C_{F4}} (1 - \tilde{Y}) \tau_R \widetilde{u_x'' u_y''} \frac{\partial \tilde{Y}}{\partial y} - \frac{C_{F1}}{C_{F4}} (1 - \tilde{Y}) \tau_R \widetilde{u_y'' Y''} \frac{\partial \tilde{u}_x}{\partial y} \quad (4.30)$$

$$\widetilde{u_y'' Y''} = -\frac{\nu_t}{\sigma_Y} \frac{\partial \tilde{Y}}{\partial y} - \frac{C_{F2}}{C_{F4}} (1 - \tilde{Y}) \tau_R \widetilde{u_y''^2} \frac{\partial \tilde{Y}}{\partial y} - \frac{C_{F1}}{C_{F4}} (1 - \tilde{Y}) \tau_R \widetilde{u_y'' Y''} \frac{\partial \tilde{u}_y}{\partial y} \quad (4.31)$$

From this approximation, it can be seen that there is a way to make $\widetilde{u'' Y''} \gg \widetilde{v'' Y''}$.

But first, a good solution to for the equivalent mean diameter of droplets $d_{[32]}$ is needed, by solving Eq. 2.45. This would create a big enough τ_R close to the centerline, making the far most *RHS* terms important. And second, a subset of C_{Fi} parameters such as: C_{F4} and $C_{F1} \gg C_{F2}$

Chapter 4. Results

are needed too.

To tackle the first point, the solution to the calculated $d_{[32]}$ from the $\tilde{\rho}\tilde{\Omega}$ solution is shown in Figure 4.23, along with the $d_{[30]}$ obtain from the DTV experimental measurements at $x/d_n = 400$.

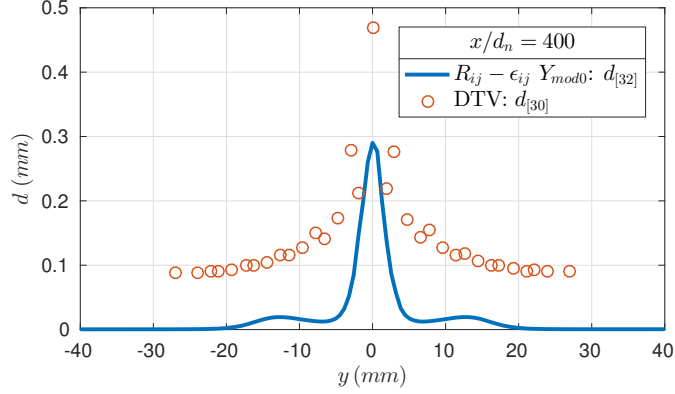


Figure 4.23 – Equivalent diameter of droplets population against radial distance. Radial profiles from simulations and DTV at $x/d_n = 400$.

Although the solution does not fit very well the experimental measurements, because not much attention is taken to the parameters in this study case, the solution is not far off physical values, therefore it can be used.

Next, choosing $C_{F1} = 4.0$, $C_{F2} = 0.1$, $C_{F3} = 0.0$ and $C_{F4} = 4.0$ (Case 312), the budget for the RHS terms in Eq. 2.39 is shown in Figure 4.24.

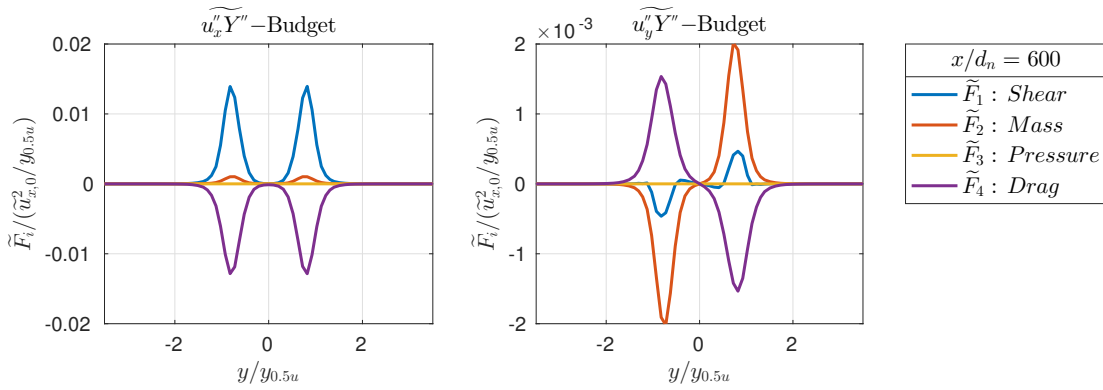


Figure 4.24 – Turbulent mass transport equation contributions budget against radial distance. Axial and radial components at $x/d_n = 400$.

Where the contributions are:

- \tilde{F}_1 Shear: $C_{F1} \tilde{u}_j'' \tilde{Y}'' \frac{\partial \tilde{u}_i}{\partial x_j}$;

- \tilde{F}_2 Mass: $-C_{F2} \widetilde{u''_i u''_j} \frac{\partial \tilde{Y}}{\partial x_j}$;
- \tilde{F}_3 Pressure: $-C_{F3} \frac{1}{\bar{\rho}} \overline{Y''} \frac{\partial \bar{p}}{\partial x_i}$;
- \tilde{F}_4 Drag: $C_{F4} \frac{1}{\bar{\rho}} \bar{F}_{Drag,i}$.

From this alternative solution to $\widetilde{u''_i Y''}$, from now on called F_i , the calculated mean-slip velocity can also be obtained. This is not a solution to the model however, it is the same Eq. 4.8, but using the F_i solution. To explicitly show this effect, both formulations are contrasted using the same RSM case. The comparison between these two solutions is shown in Figure 4.25.

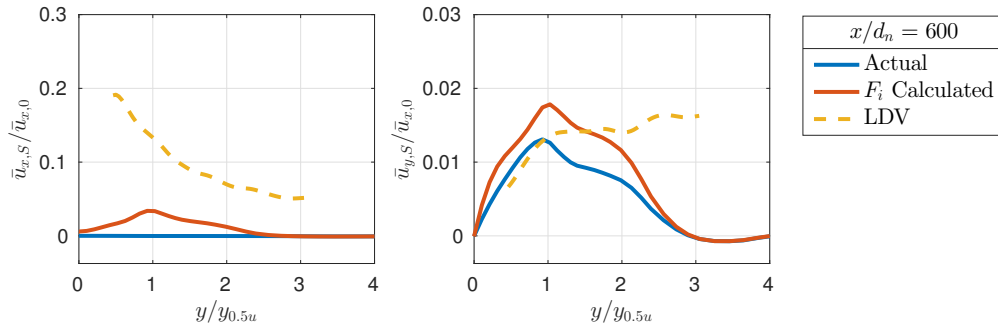


Figure 4.25 – Mean slip-velocity against radial distance as a function of Y_{mod} at $x/d_n = 600$. Experimental LDV slip-velocity shown as a benchmark.

Despite the good agreement on the mean velocity fields between the numerical and experimental results, the turbulent mass flux $\widetilde{u''_i Y''}$ does not produce an adequate solution. However, the F_i solution shows some improvement, where at least $\bar{u}_{x,S} > \bar{u}_{y,S}$. This is also true for the Reynolds stresses $\widetilde{u''_i u''_j}$, where the strong anisotropy cannot be reproduced using this RANS formulation.

Using these results, a question arises. Could a good F_i solution, coupled with the Reynolds stresses (via Σ_{ij} , Eq. 2.26 on Page 21) generate a strong anisotropy. To investigate this, an analysis on the contributions to the \tilde{R}_{ij} equations is made. The objective is to identify how the anisotropy is generated and what would be the role of Σ_{ij} in it.

To illustrate this effect, a first study case without any modification is detailed. It is based on the same $R_{ij} - \epsilon_{ij}$ model, with Y_{mod} : *Case 312* (see page 38). From the \tilde{R}_{ij} equations, the contributions at the *RHS* of Eq. 2.23 are rewritten into the final modelled version and detailed next:

$$\frac{\partial \bar{\rho} \widetilde{u''_i u''_j}}{\partial t} + \frac{\partial \bar{\rho} \widetilde{u''_i u''_j}}{\partial x_l} - \frac{\partial}{\partial x_l} \left[C_s \bar{\rho} \frac{\tilde{k}}{\tilde{\epsilon}} \widetilde{u''_l u''_k} \frac{\partial \widetilde{u''_i u''_j}}{\partial x_k} \right] = \bar{\rho} P_{ij} + \bar{\rho} \Phi_{ij} + \Sigma_{ij} - \bar{\epsilon}_{ij}. \quad (4.32)$$

where, the first production is:

$$P_{ij} = - \left(\overline{u_i'' u_k''} \frac{\partial \tilde{u}_j}{\partial x_k} + \overline{u_j'' u_k''} \frac{\partial \tilde{u}_i}{\partial x_k} \right); \quad (4.33)$$

and the second, variable density production:

$$\frac{1}{\bar{\rho}} \Sigma_{ij} = \left(\frac{1}{\rho_G} - \frac{1}{\rho_L} \right) \left[\overline{u_i'' Y''} \frac{\partial \bar{p}}{\partial x_j} + \overline{u_j'' Y''} \frac{\partial \bar{p}}{\partial x_i} \right]. \quad (4.34)$$

The modelled pressure-strain correlation is:

$$\Phi_{ij} = \phi_{ij}^{(slow)} + \phi_{ij}^{(rapid,P)} + \phi_{ij}^{(rapid,\Sigma)}; \quad (4.35)$$

with, the slow return to isotropy ($C_1 = 1.8$):

$$\phi_{ij}^{(slow)} = -C_1 \frac{\bar{\epsilon}}{\tilde{k}} \left(\overline{u_i'' u_j''} - \frac{2}{3} \tilde{k} \delta_{ij} \right); \quad (4.36)$$

the rapid P_{ij} -based redistribution ($C_2 = 0.6$):

$$\phi_{ij}^{(rapid,P)} = -C_2 \left(P_{ij} - \frac{1}{3} P_{ll} \delta_{ij} \right) \quad (4.37)$$

and, the rapid Σ_{ij} -based redistribution ($C_3 = 0.75$):

$$\phi_{ij}^{(rapid,\Sigma)} = -C_3 \frac{1}{\bar{\rho}} \left(\Sigma_{ij} - \frac{1}{3} \Sigma_{ll} \delta_{ij} \right). \quad (4.38)$$

And finally, the modelled dissipation tensor:

$$\frac{1}{\bar{\rho}} \bar{\epsilon}_{ij} = \frac{\overline{u_i'' u_j''}}{\tilde{k}} \bar{\epsilon}. \quad (4.39)$$

All these contributions are shown in Figure 4.26, for the components \tilde{R}_{11} , \tilde{R}_{22} and \tilde{R}_{12} , along with the calculated \bar{P}_{ij} from the LDV Liquid and Gas campaigns. As the budget shows, the shear stress production does not seem to be a source of the anisotropy on its own. Moreover, the modelled Σ_{ij} is a source term only in the \tilde{R}_{22} component, whatever the value in \tilde{R}_{11} . Even if a good solution for the turbulent mass flux $\overline{u_i'' Y''}$ were obtained, coupled with the main pressure gradient in the axial direction, Σ_{11} would be negligible compared to the lateral part Σ_{22} .

This analysis shows that a correct Σ_{ij} does not boost the anisotropy, it is the redistribution term that could play a significant role. Indeed, choosing a $C_3 \gg 0.75$, all the contribution in the \tilde{R}_{22} component could be given to \tilde{R}_{11} . Despite that this variation might be a good start point to boost the anisotropy, this modification is not investigated in this work.

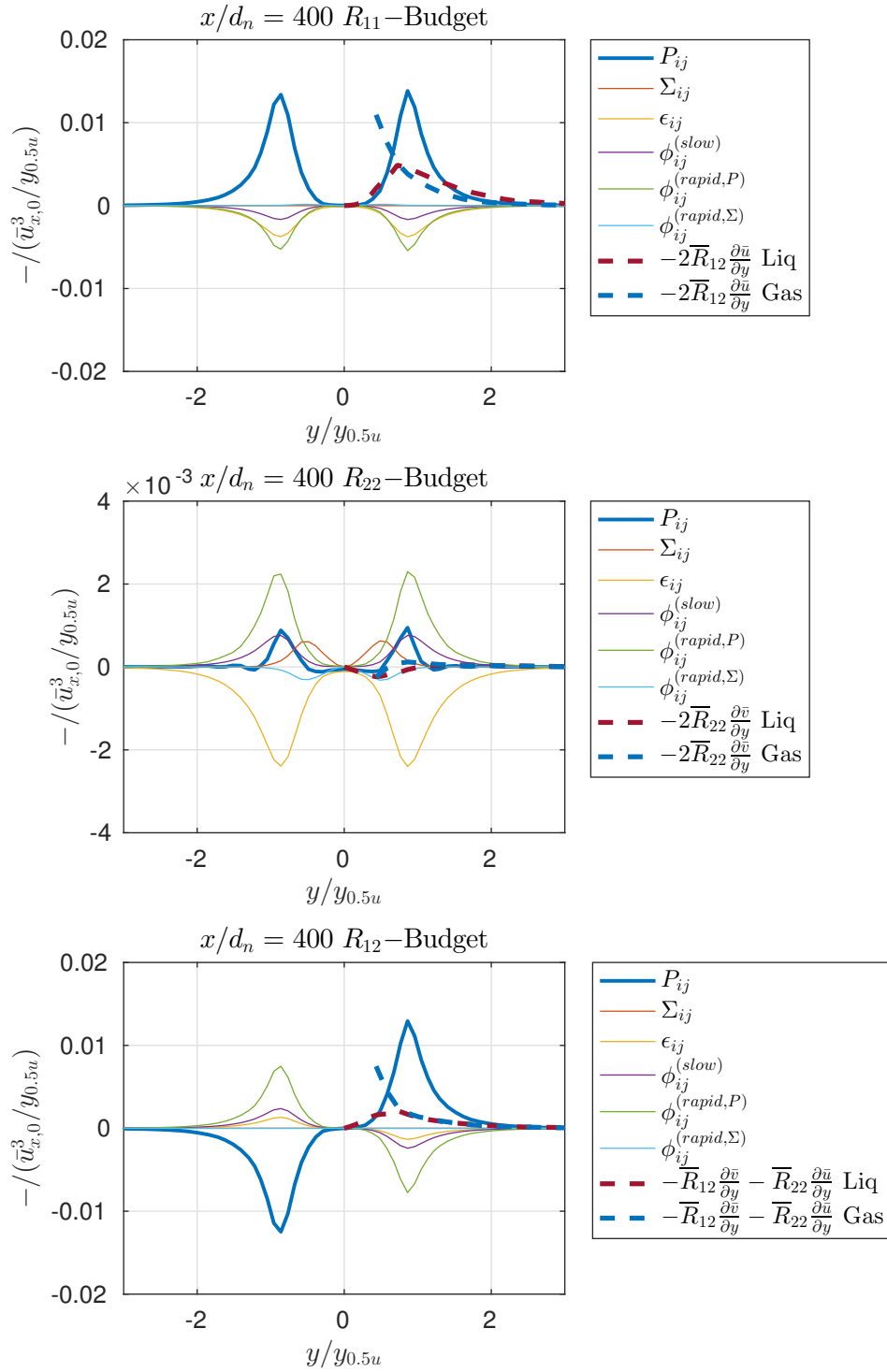


Figure 4.26 – Reynolds stresses equations budget against radial distance at $x/d_n = 400$ for the $R_{ij} - \epsilon_{ij} Y_{mod0}$ case. Experimental LDV (liquid and gas) radial profiles are shown as a benchmark.

4.2.4 Fully-coupled turbulent model

The full coupled turbulent model comes from the solution of Eq. 2.39 and the incorporation of this solution back to Eq. 2.12 and the momentum equation solver. All the system of equations is fully coupled. To do this, a detail on the solution of the second order modelled equation for $\widetilde{u_i'' Y''}$ is given first. Later, some precisions are given about the numerical solver scheme, which are necessary to attain a stable and converged solution at each time-step.

As previously shown, the *RHS* of Eq. 4.40 is an important source term in the pressure Eq. 2.53 (see page 30).

$$\frac{\partial \bar{\rho} \widetilde{Y}}{\partial t} + \frac{\partial \bar{\rho} \widetilde{u_i} \widetilde{Y}}{\partial x_i} = - \frac{\partial \bar{\rho} \widetilde{u_i'' Y''}}{\partial x_i}. \quad (4.40)$$

In the second order model, $\widetilde{u_i'' Y''}$ are obtained by solving Eq. 2.39. Then, Eq. 4.40 could be solved by simply introducing this solution into the *RHS*. However, this situation is not numerically stable for an iterative solver, where the solution is calculated starting from the previous one. Without an implicit term in the diffusion part for \widetilde{Y} , it is only up to the numerical diffusion to maintain the equation in a parabolic form. To overcome this, a blended solution is proposed between Y_{mod0} and Y_{mod2} , where the fluxes are simply:

$$\widetilde{u_i'' Y''} = F_B \widetilde{u_i'' Y''}_{Y_{mod0}} + (1 - F_B) \widetilde{u_i'' Y''}_{Y_{mod2}}. \quad (4.41)$$

If this form is introduced into to Eq. 4.40, the final equation to solve is:

$$\frac{\partial \bar{\rho} \widetilde{Y}}{\partial t} + \frac{\partial \bar{\rho} \widetilde{u_i} \widetilde{Y}}{\partial x_i} = F_B \frac{\partial}{\partial x_i} \left(\frac{\mu_t}{\sigma_Y} \frac{\partial \widetilde{Y}}{\partial x_i} \right) - (1 - F_B) \frac{\partial \bar{\rho} F_i}{\partial x_i}; \quad (4.42)$$

where F_i is the solution to Eq. 2.39 (Y_{mod2}) on *Case 312*, and $F_B = 0.1$ is the blend parameter to set between the two modelled forms.

To compare with the previous model and experimental results, the axial velocity against radial distance at $x/d_n = 400$ is presented in Figure 4.27. The results show no big improvement from the velocity field point-of-view. Indeed, the increase on the mean axial velocity is a direct consequence of the better representation of the axial slip-velocity $\bar{u}_{x,S}$. However, as Figure 4.25 showed, the solution for the turbulent mass fluxes F_i produces a negligible slip-velocity $\bar{u}_{i,S}$, compared to the one obtained by LDV.

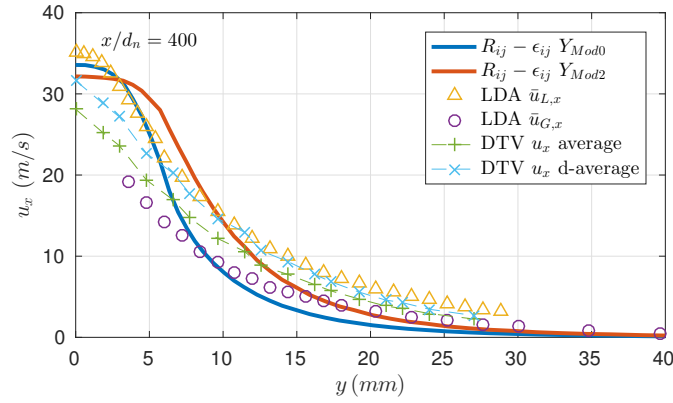


Figure 4.27 – Comparison of the mean axial velocity against radial distance as a function of Y_{mod} at $x/d_n = 400$. Experimental LDV (liquid and gas) and DTV radial profiles are shown as a benchmark.

The set of parameters used in the Y_{mod2} solution is not carefully investigated. Despite that the choice made for *Case 312* allows to generate a slip-velocity in the axial direction ($\bar{u}_{x,S}$), contrary to Y_{mod0} or Y_{mod1} , a fine tuning of C_{F1} , C_{F2} , C_{F3} and C_{F4} may produce a better solution.

Finally, to see the overall behaviour of this modelling approach, the solution for centerline velocity $\bar{u}_{x,0}$, spreading ($y_{0.5u}$) and centerline volume fraction \bar{Y}_0 are shown in Figure 4.28.

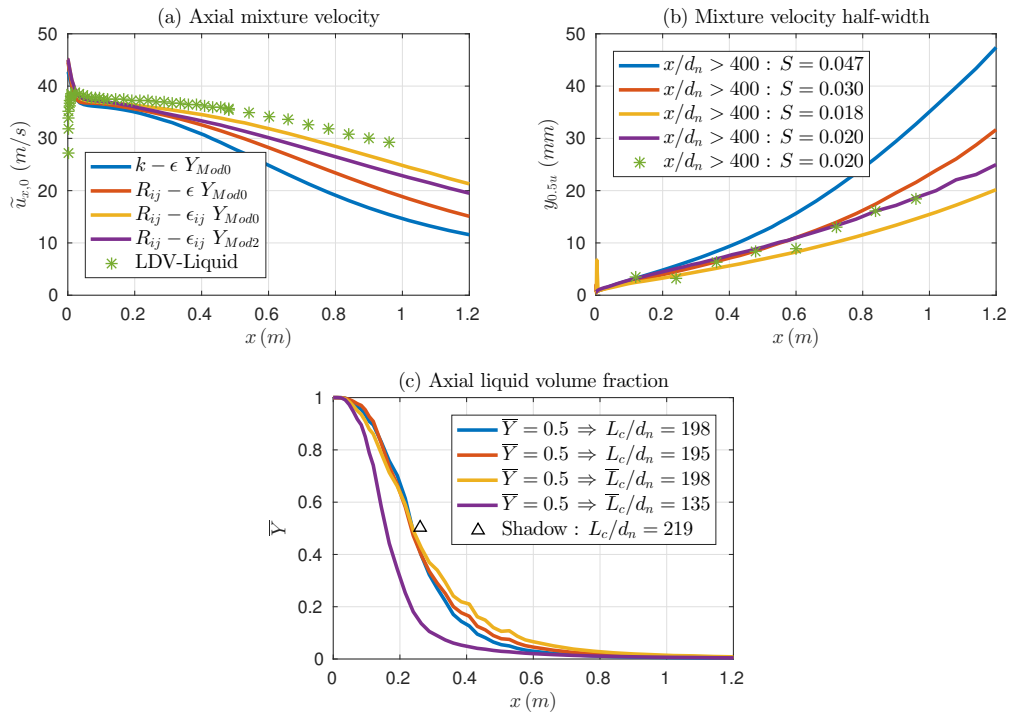


Figure 4.28 – Turbulence mass transport models' benchmark. (a) Axial velocity along the centerline; (b) Axial velocity half-width; (c) Liquid volume fraction along the centerline.

Chapter 4. Results

The effect produced on the mean spreading-rate and the centerline velocity decay-rate may not be significant. However, the increase of the slip-velocity is produced by the increase of the turbulent mass flux, modifying significantly the solution of the liquid volume fraction. This is not necessarily a bad solution, because the only experimental reference is the hypothesis that at the breakup point $\bar{Y} = 0.5$, which may not be necessarily true in this liquid jet.

To combine and to solve this fully-coupled model approach requires a lot of considerations, from the modelling of the actual physics and from numerical stability. Originally, this approach is conducted to try to generate a more case-independent formulation, relying less on modelled quantities and the choice of parameters. However, these efforts seem not to pay off, as even a second-order closure model, fully coupled with the momentum solver also needs fine tuning.

Summary

The combined results from the experimental campaigns and the numerical simulations are presented in this chapter. From this, the following points could summarise the analysis:

- The experimental results obtained from the LDV and DTV campaigns are presented first. From this analysis, some basic parameters like the axial velocity decay-rate and the spreading rate are calculated. These values are compared to the behaviour of other cases from the literature. Although the density ratio of this case study is high ($\rho_L/\rho_G = 829$), these results seem to be in accordance with other liquid round-jets cases, like in diesel injectors.
- The reconstruction of the velocity and fluctuation fields is based on the two separate LDV campaigns, the aim is to capture the liquid phase and gas phase around it. To complement, the DTV provides a fine decomposition of the liquid fields, by class of droplet sizes. The results show a non-negligible average slip-velocity $\bar{u}_{i,s}$ between the phases. This quantity plays a significant role in the reconstruction of the Favre-averaged Reynolds stresses.
- From the reconstruction of liquid and gas Reynolds stresses, a low anisotropy factor of the principal components is found on both phases, meaning a high anisotropy. In the liquid part, this value can be as small as $\bar{R}_{22,L}/\bar{R}_{11,L} \sim 0.05$, whereas in the gas phase, it can reach $\bar{R}_{22,G}/\bar{R}_{11,G} \sim 0.1$. These results differ significantly from the ones found in constant density round jets, where $\bar{R}_{22}/\bar{R}_{11} \sim 0.6$. The decomposition of the fluctuating fields by class of droplets gives a clue on the mechanism that might produce this behaviour. Indeed, the results show a drastic change in the anisotropy factor: big droplets seem to keep the same fluctuating energy from the liquid core, but a high velocity as well; as the jet breaks into droplets of smaller sizes, they seem to be more and more affected by the slip-velocity between the big droplets and gas phase, creating a wider band for the fluctuations to operate in the axial direction; finally, the smallest droplet group ($d_{[30]} < 100\mu m$) seems to follow purely the gas phase fluctuations, at the external zones of the gas entrainment. Some authors explain this behaviour by calculating the Stokes number St , however, this analysis is not presented here.
- The experimental results serve as a baseline to compare the constructed simulation cases. The analysis is centred on the behaviour of a RSM turbulence formulation, nevertheless, a basic $k - \epsilon$ model is also shown for comparison purposes. The velocity field obtained using the RSM turbulence is very close to the experimental observations, however, this result is obtained assuming a very low anisotropy factor, following the experimental observations. This transforms into a very high turbulent Schmidt number of $\sigma_Y = 5.5$, which is far from the most common use of $\sigma_Y \approx 0.9$.
- Despite the inclusion of variable density effects into the RSM model, even with the use of a second-order solution for the turbulent mass fluxes $\overline{u_i'' Y''}$, the high anisotropy experimentally observed can not be reproduced in the simulation cases. An analysis

Chapter 4. Results

on the budget inside the \tilde{R}_{ij} equations shows that the Σ_{ij} production only works in the lateral \tilde{R}_{22} component. This result points out that maybe it is the redistribution part, modelled from the pressure-strain correlation, that might play a significant role in the source of the anisotropy.

Summary, conclusions and perspectives

This short chapter is purely dedicated to the general conclusions of this work. Although a series of partial conclusions are already presented on each chapter, the general view presented here is made to wrap-up the combined experimental and numerical approaches.

The study of the performance of sprinklers/sprayers in agricultural applications is a continuous development research. New regulations aim to both reduce water consumption on irrigation applications, and to minimise ambient pollution when crop protection products are applied to cultures. These research subjects are carried out at IRSTEA Montpellier centre, where technical, normative, experimental and theoretical approaches are developed in conjunction with public and private institutions.

The experimental and numerical approaches treated here are only one small part of the vast research applied to agricultural sprinklers/sprayers at IRSTEA in collaboration with IRPHE. From these particular activities, the following points are extracted to summarise and to conclude this work:

- Based on previous observations, and to simplify the experimental conditions, a particular case scenario is created to study the atomization and dispersion on an agricultural-like jet, where purified water is injected into stagnant air. From this, a circular nozzle of diameter $d_n = 1.2 \text{ mm}$ and length $L_c/d_n = 50$ is created. The injection average bulk velocity is set to $\bar{u}_J = 35 \text{ m/s}$. This geometry, fluid properties and operating conditions produce a turbulent atomization regime.
- The atomization and dispersion are first investigated using numerical CFD simulations. Here, the liquid jet is represented as a variable-density single-fluid Favre-averaged mixture. Since the size of the problem is relatively big, compared to other applications like fuel injectors, the advantage of such modelling technique is that there is no need to represent every length scale present on the flow, therefore saving on computational resources, but at the expense of model completeness.

Summary, conclusions and perspectives

- The mixture model is successfully implemented using the *OpenFOAM* CFD code. It allows to represent the solution in an arbitrary 3D mesh, running under a custom U-RANS solver. The flexibility of the programming philosophy behind the code allows to easily implement several turbulence models: $k - \epsilon$ and *RSM*; both including variable density effects from the mixture model. Also, first-order and second-order closures for the turbulent mass flux are implemented in a fully coupled solver. The quasi-multiphase approach is tackled by the use of a transport equation for the mean interface area per unit volume quantity.
- To have a benchmark baseline for the model, an experimental campaign is carried out. LDV and Shadowgraphy optical techniques are used to measure the mean velocity and fluctuating fields. LDV is used to capture the liquid field and the gas around it, by seeding small olive-oil particles as tracers. In a separate campaign, DTV from the shadow images is applied to the disperse part of the jet, $x/d_n > 400$, adding more information to the liquid phase related to the distribution of droplet sizes.
- A very specific LDV configuration is used to perform the data acquisition on each phase. A first measurement campaign is performed only in the liquid, where the results are assimilated to the velocity and fluctuating fields of the jet's liquid phase. For the gas phase, since the liquid droplets might interfere with the olive-oil tracers, some considerations have to be taken. First, it is found that the Doppler signal detected from the relatively big water droplets ($d > 30 \mu m$) is considerably higher than the one produced by the small olive-oil tracers ($d \sim 1 \mu m$), making the threshold of the LDV burst signal a good candidate to separate the gas from the liquid signal. Although the available LDV equipment does not allow to perform such separation, a combined narrow BP-Filter, higher acceptable SNR and higher sensitivity on the PM gain allow to eliminate most of the droplet events captured along with the tracers. The resulting signal is not completely depurated from the liquid droplets. However, having the LDV results only in the liquid phase as a comparison, these are considered to be closer to the expected behaviour of a gas velocity signal, and not from a mixture of liquid droplets and gas tracers. This combined technique allows to reconstruct the liquid and gas velocity fields along with the Reynolds stresses within an acceptable margin of error.
- Shadow images are used to run a custom DTV algorithm developed and implemented in MATLAB. A shadow strobe system from Dantec Dynamics is used to capture the projected shadow of the liquid jet/droplets into a high-speed CCD camera. The first part of the algorithm detects and extracts droplet's contours from the acquired 12-bit grey-scale shadow images, even if they are out-of-focus. The second part performs a matching between the centroids of these contours to estimate the velocity from two consecutive frames. To account for the out-of-focus droplets, a calibration procedure is performed on opaque discs of a known diameter. This procedure gives an equivalent diameter correction for the out-of-focus objects, along with their relative position as a function of the detected contrast ratio and edge gradient. The results of the DTV algorithm are the velocity and fluctuating fields, decomposed by the estimated droplets

diameters.

- The numerical model seems to approach the experimental results when the mean velocity fields are contrasted. The calculated values for the centerline velocity decay rate and the spreading rate are in accordance with values found in the literature. However, no good agreement is found when comparing the fluctuating fields. Indeed, one of the main motivations of this work is the use of a *RSM* to take into account the anisotropy on the Reynolds stresses. However, several variations of this approach, even with a second-order closure for the turbulent mass flux, do not seem to approach the experimentally found anisotropy, where $\bar{R}_{22}/\bar{R}_{11} \sim 0.05$.
- A close analysis on the source mechanism that might produce the anisotropy of the Reynolds stresses in the *RSM* formulation is studied. If this effect is not present in constant density or slightly variable density flow, the mechanism of production must be a consequence of the large density ratio of this case ($\rho_L/\rho_G = 828$). By examining the source terms in the R_{ij} equations from the *RSM*, the redistribution part of the variable density production term Σ_{ij} , issued from the modelling of the pressure-strain correlation, seems to be a good candidate to investigate. The coupling of the mean pressure gradient and the turbulent mass fluxes, that generates Σ_{ij} , seems to act only on the lateral R_{22} component, no matter if a first-order or second-order formulation is used. This means that the redistribution part should be the only option to boost the anisotropy under this formulation.

Although the comparative analysis from the two approaches does not always give good results, it is considered that both add a good amount of information to the understanding of this study case. Nevertheless, there are several topics that could be treated to improve the analysis, such as:

- The calibration procedure on the shadow images is not applied to the measured droplet population. As the results show, the average and fluctuating quantities are strongly dependent on the granulometry. Therefore, a proper distribution of the droplet sizes must be obtained, by eliminating the biases related to the DOF and sizes estimation. However, if done so, more images would be needed to reconstruct a set of well converged average fields, since more droplets are likely to be rejected from the analysis.
- With a good estimation of the droplet population and distribution, a good estimation of the average liquid mass fraction \bar{Y} can be made from the shadow images. Stevenin [57] work shows a good agreement between the data acquired using an OP and the estimation made by the DTV system, where \bar{Y} is estimated by placing the volume occupied by the droplets inside the calculated DOF.
- The data obtained by the LDV on the gas phase is considered to be only an estimation. Indeed, the contamination of liquid droplets inside the population of gas tracers events results induces an underestimation of the Liquid-Gas slip-velocity $\bar{u}_{i,s}$. Newer LDV BSA systems allow to carefully discriminate events by the Doppler burst pedestal intensity.

Summary, conclusions and perspectives

The use of such a system could improve the accuracy and precision of the gas results, relying less on artificial filtering that might introduce several biases.

- Having a good droplet population and a solid estimation of $\bar{u}_{i,S}$, the Stokes number St can be calculated by droplet class of diameter. This quantity would allow to have a better explanation on the droplet's response to turbulent fluctuations as a function of their sizes. This mechanism seems to be a good candidate to explain the strong anisotropy of the Reynolds stresses.
- From the analysis of the R_{ij} equations budget, there is only one possible way to boost the anisotropy of the Reynolds stresses. The production term associated to the variable density formulation, Σ_{ij} , is only significantly important in the lateral direction, despite that $\bar{u}_{x,S} \gg \bar{u}_{y,S}$. Using only a linear pressure-strain correlation model, it is the redistribution part of Σ_{ij} which could play a significant role in the anisotropy production. Although there is no more information to support this, increasing $C_3 \gg 0.75$ would kill the source term in the lateral direction, creating an artificial source in the axial one.

Based on these perspectives, to conduct a new study case would require a new measurement campaign, along with new simulation cases. To carry on these activities simultaneously is very time consuming, and would also require new experimental equipment and HPC availability.

Finally, as a general conclusion, a great amount of effort is put to carefully implement and to solve the numerical cases constructed, along with a detailed experimental campaign. These two activities, carried out simultaneously, allow to see the results from a perspective that gives a valuable feedback in both directions.

Bibliography

- [1] M. Al Heidary, J. Douzals, C. Sinfort, and A. Vallet. Influence of spray characteristics on potential spray drift of field crop sprayers: A literature review. *Crop Protection*, 63: 120–130, 2014.
- [2] M. Amielh, T. Djeridane, F. Anselmet, and L. Fulachier. Velocity near-field of variable density turbulent jets. *International Journal of Heat and Mass Transfer*, 39(10):2149–2164, 1996.
- [3] A. Andreini, C. Bianchini, S. Puggelli, and F.-X. Demoulin. Development of a turbulent liquid flux model for Eulerian–Eulerian multiphase flow simulations. *International Journal of Multiphase Flow*, 81:88–103, 2016.
- [4] P.-A. Beau. *Modélisation de l'atomisation d'un jet liquide : application aux sprays Diesel*. Doctoral thesis, Université de Rouen, 2006.
- [5] A. Belhadef, A. Vallet, M. Amielh, and F. Anselmet. Pressure-swirl atomization: Modeling and experimental approaches. *International Journal of Multiphase Flow*, 39:13–20, 2012.
- [6] A. Boutier. *Vélocimétrie laser pour la mécanique des fluides*. Lavoisier, 2012. ISBN 978-2-7462-8821-8.
- [7] A. Cartellier. Optical probes for local void fraction measurements: Characterization of performance. *Review of Scientific Instruments*, 61(2):874–886, 1990.
- [8] P. Chassaing, R. A. Antonia, F. Anselmet, L. Joly, and S. Sarkar. *Variable Density Fluid Turbulence*, volume 69 of *Fluid Mechanics and Its Applications*. Springer Netherlands, 2002. ISBN 978-90-481-6040-2.
- [9] B. B. Dally, D. F. Fletcher, and A. R. Masri. Flow and mixing fields of turbulent bluff-body jets and flames. *Combustion Theory and Modelling*, 2(2):193–219, 1998.
- [10] G. G. Daves, R. O. Buckius, J. E. Peters, and A. R. Schroeder. Morphology Descriptors of Irregularly Shaped Particles from Two-Dimensional Images. *Aerosol Science and Technology*, 19(2):199–212, 1993.
- [11] M. De Luca. *Contribution à la modélisation de la pulvérisation d'un liquide phytosanitaire en vue de réduire les pollutions*. Doctoral thesis, Aix-Marseille II, 2007.

Bibliography

- [12] M. De Luca, A. Vallet, and R. Borghi. Pesticide atomization modeling for hollow-cone nozzle. *Atomization and Sprays*, 19(8):741–753, 2009.
- [13] A. Delon. *Instabilité de flapping: origine et effets sur la structure et le spray d'un jet atomisé*. Doctoral thesis, Université Grenoble Alpes, 2016.
- [14] F-X. Demoulin, P-A. Beau, G. Blokkeel, A. Mura, and R. Borghi. A new model for turbulent flows with large density fluctuations: Application to liquid atomization. *Atomization and Sprays*, 17(4), 2007.
- [15] J. Desantes, J. García-Oliver, J. Pastor, A. Pandal, E. Baldwin, and D. Schmidt. Coupled/decoupled spray simulation comparison of the ECN spray a condition with the Σ -Y Eulerian atomization model. *International Journal of Multiphase Flow*, 80:89–99, 2016.
- [16] C. Dumouchel. On the experimental investigation on primary atomization of liquid streams. *Experiments in Fluids*, 45(3):371–422, 2008.
- [17] B. Duret, J. Reveillon, T. Menard, and F. F-X. Demoulin. Improving primary atomization modeling through DNS of two-phase flows. *International Journal of Multiphase Flow*, 55: 130–137, 2013.
- [18] H. A. El-Asrag and M. Braun. Effect of turbulence non-isotropy modeling on spray dynamics for an evaporating Acetone spray jet. *International Journal of Multiphase Flow*, 68:100–120, 2015.
- [19] N. Fdida. *Développement d'un système de granulométrie par imagerie Application aux sprays larges et hétérogènes*. Ph.d thesis, Université de Rouen, 2008.
- [20] N. Fdida and J.-B. Blaisot. Drop size distribution measured by imaging: determination of the measurement volume by the calibration of the point spread function. *Meas. Sci. Technol.*, 21(2):025501, 2010.
- [21] V. Ferrand, R. Bazile, J. Borée, and G. Charnay. Gas–droplet turbulent velocity correlations and two-phase interaction in an axisymmetric jet laden with partly responsive droplets. *International Journal of Multiphase Flow*, 29(2):195–217, 2003.
- [22] J. H. Ferziger and M. Peric. *Computational Methods for Fluid Dynamics*. Springer-Verlag Berlin Heidelberg, 2002. ISBN 3540420746.
- [23] M. M. Gibson and B. E. Launder. Ground effects on pressure fluctuations in the atmospheric boundary layer. *Journal of Fluid Mechanics*, 86(03):491, 1978.
- [24] S. Gold, A. Rangarajan, C. Lu, S. Pappu, and E. Mjolsness. New algorithms for 2D and 3D point matching: pose estimation and correspondence. *Pattern Recognition*, 31(8): 1019–1031, 1998.
- [25] C. J. Greenshields. *OpenFOAM 2.4.0 Programmer's Guide*. OpenFOAM Foundation Ltd., 2015. URL www.openfoam.org.

- [26] C. J. Greenshields. *OpenFOAM 2.4.0 User's Guide*. OpenFOAM Foundation Ltd., 2015. URL www.openfoam.org.
- [27] H. Grosshans, E. Kristensson, R. Z. Szász, and E. Berrocal. Prediction and Measurement of the local extinction coefficient in sprays for 3D simulation/experiment data comparison. *International Journal of Multiphase Flow*, 72:218–232, 2015.
- [28] M. Hong, A. Cartellier, and E. J. Hopfinger. Characterization of phase detection optical probes for the measurement of the dispersed phase parameters in sprays. *International Journal of Multiphase Flow*, 30(6):615–648, 2004.
- [29] J. W. Hoyt and J. J. Taylor. Waves on water jets. *Journal of Fluid Mechanics*, 83(01):119, 1977.
- [30] H. J. Hussein, S. P. Capp, and W. K. George. Velocity measurements in a high-Reynolds-number, momentum-conserving, axisymmetric, turbulent jet. *Journal of Fluid Mechanics*, 258(1994):31–75, 1994.
- [31] R. Issa. Solution of the implicitly discretised fluid flow equations by operator-splitting. *Journal of Computational Physics*, 62:40–65, 1986.
- [32] S. Jakirlic and K. Hanjalic. A new approach to modelling near-wall turbulence energy and stress dissipation. *Journal of Fluid Mechanics*, 459:139–166, 2002.
- [33] H. Jasak. *Error Analysis and Estimation for the Finite Volume Method with Applications to Fluid Flows*. Doctoral thesis, University of London, 1996.
- [34] W. W. Jones and B. B. Launder. The prediction of laminarization with a two-equation model of turbulence. *International Journal of Heat and Mass Transfer*, 15(2):301–314, 1972.
- [35] J. B. Joshi, K. Nandakumar, G. M. Evans, V. K. Pareek, M. M. Gumulya, M. J. Sathe, and M. A. Khanwale. Bubble generated turbulence and direct numerical simulations. *Chemical Engineering Science*, 157:26–75, 2017.
- [36] N. Kadem, A. Tchiftchibachian, and R. Borghi. Experimental and numerical modeling study for irrigation gun water jet. *Atomization and Sprays*, 18:315–341, 2008.
- [37] V. Kumar, A. Yeola, M. Braun, J. Schuetze, and L.-Y. Lee. Numerical simulation of evaporating diesel sprays using $\Omega - Y$ model. In *ICLASS 2015, 13th International Conference on Liquid Atomization and Spray Systems*, Tainan, Taiwan, 2015.
- [38] V. Kumar, A. Yeola, S. Patwardhan, M. Braun, J. Schuetze, and L.-Y. Lee. Numerical simulation of non-evaporating sprays using $\Omega - Y$ model. In *ICLASS 2015, 13th International Conference on Liquid Atomization and Spray Systems*, Tainan, Taiwan, 2015.

Bibliography

- [39] B. E. Launder, G. J. Reece, and W. Rodi. Progress in the development of a Reynolds-stress turbulence closure. *Journal of Fluid Mechanics*, 68(03):537–566, 1975.
- [40] R. Lebas, T. Menard, P. P.-A. Beau, A. Berlemont, and F. F.-X. Demoulin. Numerical simulation of primary break-up and atomization: DNS and modelling study. *International Journal of Multiphase Flow*, 35(3):247–260, 2009.
- [41] D. Modarres, S. Elghobashi, and H. Tan. Two-component LDA measurement in a two-phase turbulent jet. *AIAA Journal*, 22(5):624–630, 1984.
- [42] A. G. Mychkovsky and S. L. Ceccio. LDV measurements and analysis of gas and particulate phase velocity profiles in a vertical jet plume in a 2D bubbling fluidized bed Part II: Mass and momentum transport. *Powder Technology*, 220:47–54, 2012.
- [43] A. G. Mychkovsky, D. Rangarajan, and S. L. Ceccio. LDV measurements and analysis of gas and particulate phase velocity profiles in a vertical jet plume in a 2D bubbling fluidized bed. Part I: A two-phase LDV measurement technique. *Powder Technology*, 220:55–62, 2012.
- [44] S. V. Patankar and D. B. Spalding. A calculation procedure for heat, mass and momentum transfer in three-dimensional parabolic flows. *International Journal of Heat and Mass Transfer*, 15(10):1787 – 1806, 1972.
- [45] R. Payri, S. Ruiz, J. Gimeno, and P. Martí-Aldaraví. Verification of a new CFD compressible segregated and multi-phase solver with different flux updates-equations sequences. *Applied Mathematical Modelling*, 39(2):851–861, 2015.
- [46] S. B. Pope. An explanation of the turbulent round-jet/plane-jet anomaly. *AIAA journal*, 1978.
- [47] S. B. Pope. *Turbulent Flows*. Cambridge University Press, 2000. ISBN 0521598869.
- [48] H. M. Prasser, M. Misawa, and I. Tiseanu. Comparison between wire-mesh sensor and ultra-fast X-ray tomograph for an air-water flow in a vertical pipe. *Flow Measurement and Instrumentation*, 16(2-3):73–83, 2005.
- [49] F. Prevost, J. Boree, H. Nuglisch, and G. Charnay. Measurements of fluid/particle correlated motion in the far field of an axisymmetric jet. *International Journal of Multiphase Flow*, 22(4):685–701, 1996.
- [50] J. Rotta. Statistische Theorie nichthomogener Turbulenz. *Zeitschrift für Physik*, 129(6): 547–572, 1951.
- [51] E. Ruffin, R. Schiestel, F. Anselmet, M. Amielh, and L. Fulachier. Investigation of characteristic scales in variable density turbulent jets using a second-order model. *Physics of Fluids*, 6(8):2785, 1994.

-
- [52] R. Salcedo, A. Vallet, R. Granell, C. Garcerá, E. Moltó, and P. Chueca. Eulerian–Lagrangian model of the behaviour of droplets produced by an air-assisted sprayer in a citrus orchard. *Biosystems Engineering*, 2016.
- [53] K. Sallam, Z. Dai, and G. G. Faeth. Liquid breakup at the surface of turbulent round liquid jets in still gases. *International Journal of Multiphase Flow*, 28(3):427–449, 2002.
- [54] M. Sanjose. *Evaluation de la méthode Euler-Euler pour la simulation aux grandes échelles des chambres à carburant liquide*. Doctoral thesis, Université de Toulouse, 2009.
- [55] M. J. Sathe, I. H. Thaker, T. E. Strand, and J. B. Joshi. Advanced PIV/LIF and shadowgraphy system to visualize flow structure in two-phase bubbly flows. *Chemical Engineering Science*, 65(8):2431–2442, 2010.
- [56] R. Schiestel. *Méthodes de modélisation et de simulation des écoulements turbulents*. Hermès Lavoisier, 2006. ISBN 2-7462-1336-2.
- [57] C. Stevenin. *Étude de l'atomisation d'un jet d'eau haute vitesse Application à l'irrigation par aspersion et à la pulvérisation*. Doctoral thesis, École Centrale Marseille, 2012.
- [58] C. Stevenin, S. Tomas, A. Vallet, M. Amielh, and F. Anselmet. Flow characteristics of a large-size pressure-atomized spray using DTV. *International Journal of Multiphase Flow*, 84:264–278, 2016.
- [59] C. Stevenin, A. Vallet, S. Tomas, M. Amielh, and F. Anselmet. Eulerian atomization modeling of a pressure-atomized spray for sprinkler irrigation. *International Journal of Heat and Fluid Flow*, 57:142–149, 2016.
- [60] A. Vallet, A. A. Burluka, and R. Borghi. Development of a eulerian model for the "atomization" of a liquid jet. *Atomization and Sprays*, 11(6):619–642, 2001.
- [61] H.-G. Weller, G. Tabor, H. Jasak, and C. Fureby. A tensorial approach to computational continuum mechanics using object-oriented techniques. *Computer in Physics*, 12(6): 620–631, 1998.
- [62] C. R. Wilke. A Viscosity Equation for Gas Mixtures. *The Journal of Chemical Physics*, 18(4): 517–519, 1950.
- [63] P. Wu and G. Faeth. Onset and end of drop formation along the surface of turbulent liquid jets in still gases. *Physics of Fluids (1994-present)*, 7(11):2915–2917, 1995.
- [64] P. Wu, L. Tseng, and G. Faeth. Primary breakup in gas/liquid mixing layers for turbulent liquids. *Atomization and Sprays*, 1992.
- [65] J. Yon. *Jet Diesel Haute Pression en Champ Proche et Lointain : Etude par Imagerie*. Doctoral thesis, Université de Rouen, 2003.

My My,
Hey Hey
— *Neil Young*

(Out of the Blue)